ISSN: 2220-9506 (Print)
ISSN: 2414-0473 (Online)

ПРИБОРЫ И МЕТОДЫ ИЗМЕРЕНИЙ

DEVICES AND METHODS OF MEASUREMENTS

Том 13 № 3 Vol. 13

2022

ПРИБОРЫ И МЕТОДЫ ИЗМЕРЕНИЙ

Научно-технический журнал

Основан в 2010 г.

Учредитель
Белорусский национальный технический университет

Выходит 4 раза в год

Журнал включен в базы данных:
Web of Science Core Collection (ESCI),
EBSCO, DOAJ, WorldCat, OpenAIRE, Google Scholar, РИНЦ,
ЭБС «Лань», НЭБ «КиберЛенинка», Соционет

Том 13 **№ 3** **2022**

Издание зарегистрировано в Министерстве информации Республики Беларусь 25 июня 2010 г.
Регистрационный номер 1372

В соответствии с решением ВАК от 8 июля 2011 г. №13/1 журнал включен в Перечень научных изданий для опубликования результатов диссертационных исследований; научное направление: «Средства и методы измерений, контроля, диагностики и оценки качества объектов и процессов» (технические и физико-математические науки)

ISSN 2220-9506

Подписка осуществляется через почтовые отделения связи по «Каталогу газет и журналов Республики Беларусь».
Подписные индексы – 74835; 748352.

Ответственный секретарь редакции: Шахлевич Л.Н.
Редактор: Чабарова О.Л.
Набор и верстка выполнены в редакции журнала «Приборы и методы измерений».
Подписано в печать 19.10.2022. Формат бумаги 60×84 1/8. Бумага мелованная.
Гарнитура Times New Roman. Печать цифровая. Усл. печ. л. 9,30. Уч.-изд. л. 6,36. Тираж 100 экз.
Дата выхода в свет 21.10.2022. Заказ № 634.
Отпечатано в Белорусском национальном техническом университете. ЛП № 02330/74 от 03.03.2014. Пр-т Независимости, 65, 220013, г. Минск

АДРЕС РЕДАКЦИИ:
Белорусский национальный технический университет
пр-т Независимости, 65, 220013, г. Минск, Республика Беларусь,
тел.: +375 (17) 293 96 67, факс: +375 (17) 292 67 94
e-mail: pimi@bntu.by
http://pimi.bntu.by

http://pimi.bntu.by ISSN (print): 2220-9506

DEVICES AND METHODS OF MEASUREMENTS

Scientific and Engineering Journal

Founded in 2010

Founder
Belarusian National Technical University

Issued four times a year

The Journal is included in the following databases:
Web of Science Core Collection (ESCI),
EBSCO, DOAJ, WorldCat, OpenAIRE, Google Scholar,
RISC, Lan, CyberLeninka, Socionet

Volume 13 **№ 3** **2022**

ADDRESS:
Belarusian National Technical University
Nezavisimosty Ave., 65, Minsk 220013, Belarus
Tel.: +375 (17) 293 96 67, fax: +375 (17) 292 67 94
e-mail: pimi@bntu.by
http://pimi.bntu.by

СОДЕРЖАНИЕ

CONTENTS

Stand Equipment and Test Methods of Modern Optical Sights

A.M. Kurganovich, V.A. Stasilovich, I.P. Shishkin, A.P. Shkadarevich

"STC "LEMT" BelOMO",
Makayenka str., 23, Minsk 220114, Belarus

Received 02.05.2022
Accepted for publication 20.09.2022

Abstract

Manufacture of sights with high output characteristics is a prerequisite for achieving the necessary accuracy when shooting. The aim of the work was to analyze the influence of pancratic optical sights' main parameters on their output performance characteristics.

It is shown that in order to achieve the quality level of the world's best samples, high image quality – no drop in contrast by no more than 30 % of the calculated value, careful manufacturing and control of both mechanical and optical parts, as well as components of the assembly units of products, the technological process of assembly and alignment is necessary.

Bench equipment and test methods which made it possible significantly increase the level of serial production are described, also some characteristics of GS3-12×50, GS3-24×56, GS5-25×56 "NTC "LEMT" BelOMO" are presented.

Keywords: pancratic sight, contrast transfer function, resolution, control technique, bench equipment.

DOI: 10.21122/2220-9506-2022-13-3-165-171

Адрес для переписки:
Стасилович В.А.
«НТЦ «ЛЭМТ» БелОМО»,
ул. Макаёнка, 23, г. Минск 220114, Беларусь
e-mail: Stasilovich19@gmail.com

Address for correspondence:
Stasilovich V.A.
"STC "LEMT" BelOMO",
Makayenka str., 23, Minsk 220114, Belarus
e-mail: Stasilovich19@gmail.com

Для цитирования:
A.M. Kurganovich, V.A. Stasilovich, I.P. Shishkin, A.P. Shkadarevich.
Stand Equipment and Test Methods of Modern Optical Sights.
Приборы и методы измерений.
2022. – Т. 13, № 3. – С. 165–171.
DOI: 10.21122/2220-9506-2022-13-3-165-171

For citation:
A.M. Kurganovich, V.A. Stasilovich, I.P. Shishkin, A.P. Shkadarevich.
Stand Equipment and Test Methods of Modern Optical Sights.
Devices and Methods of Measurements.
2022, vol. 13, no. 3, pp. 165–171.
DOI: 10.21122/2220-9506-2022-13-3-165-171

Стендовое оборудование и методики испытаний современных оптических прицелов

А.М. Курганович, В.А. Стасилович, И.П. Шишкин, А.П. Шкадаревич

«НТЦ «ЛЭМТ» БелОМО»,
ул. Макаёнка, 23, г. Минск 220114, Беларусь

Поступила 02.05.2022
Принята к печати 20.09.2022

Изготовление прицелов с высокими выходными характеристиками является необходимым условием для достижения необходимых точностей при стрельбе. Целью работы был анализ влияния основных параметров панкратических оптических прицелов на их выходные эксплуатационные характеристики.

Показано, что для достижения уровня качества лучших мировых образцов, высокого качества изображения – непадения контраста на более чем на 30 % от расчётного значения, необходимы тщательное изготовление и контроль как механических и оптических деталей, так и узлов сборочных единиц изделий, технологического процесса сборки и юстировки.

Описаны стендовое оборудование и методики испытаний, позволившие существенно повысить уровень серийной продукции, а также представленны некоторые характеристики прицелов GS3-12×50, GS3-24×56, GS5-25×56 «НТЦ «ЛЭМТ» БелОМО».

Ключевые слова: панкратический прицел, частотно-контрастная характеристика, разрешающая способность, методика контроля, стендовое оборудование.

DOI: 10.21122/2220-9506-2022-13-3-165-171

Адрес для переписки:
Стасилович В.А.
«НТЦ «ЛЭМТ» БелОМО»,
ул. Макаёнка, 23, г. Минск 220114, Беларусь
e-mail: Stasilovich19@gmail.com

Address for correspondence:
Stasilovich V.A.
"STC "LEMT" BelOMO",
Makayenka str., 23, Minsk 220114, Belarus
e-mail: Stasilovich19@gmail.com

Для цитирования:
A.M. Kurganovich, V.A. Stasilovich, I.P. Shishkin, A.P. Shkadarevich.
Stand Equipment and Test Methods of Modern Optical Sights.
Приборы и методы измерений.
2022. – Т. 13, № 3. – С. 165–171.
DOI: 10.21122/2220-9506-2022-13-3-165-171

For citation:
A.M. Kurganovich, V.A. Stasilovich, I.P. Shishkin, A.P. Shkadarevich.
Stand Equipment and Test Methods of Modern Optical Sights.
Devices and Methods of Measurements.
2022, vol. 13, no. 3, pp. 165–171.
DOI: 10.21122/2220-9506-2022-13-3-165-171

Introduction

Progress in development of sniper weapons has provided an increase both in the firing range and in the stability of ballistic parameters [1]. Naturally this puts forward increased requirements for optical sights' whose contribution to high-precision shooting is also important and critical. Existing models of sniper sights presented by domestic manufacturers do not allow firing comparable to the accuracy shown by the weapon [2].

Shooting at long distances requires large optical magnifications which is accompanied by a proportional decrease in the angular field of view. This in turn complicates the task of finding and detecting a target so the use of pankratic sights of variable multiplicity has no alternative [3]. The latter factor makes it relevant and expedient to simultaneously increase not only the optical magnification, but also the difference in the multiplicity of pancratic systems (sights). At the same time the task of ensuring high image quality over the entire optical magnification range becomes more complicated which imposes strict requirements on the optical sight lens which largely determines the quality of the optical image and the pancratic node which must provide large optical magnification differences as well as maintaining and improving high optical image quality over a wider range of optical and mechanical components. In addition it should be borne in mind that the previously mentioned increase in firing range is achieved by increasing the caliber which is accompanied by an increase in mechanical loads on optical parts and assemblies. This fact further complicates the problems of developing and producing high-quality sights [4].

Thus the creation of bench equipment both to ensure a high-performance technological process of assembling and adjusting optical sights, and to control the quality of finished sights is an urgent technical problem without which it is impossible to produce optical products of a high technical level sufficient for the best sniper weapons.

The criteria for sights when working with bench equipment, as well as measurement methods that allow to master the production of optical sights of variable multiplicities (Z4, Z5, Z8) with an increase of up to 40 times which compete in terms of technical level with the best world samples are presented.

High-quality optical sights must have high optical and mechanical characteristics: the maximum resolution value, image contrast in the entire range of the angular field of view of the sight lens both at the values of the maximum resolution and at the values of the resolution greater than the limit, high transmittance of the optical system, immutability of the position of the sighting element – mesh, during and after mechanical action, as well as while working with the elements of the sight (zoom change leash, alignment flywheels, parallactic adjustment leash), smooth operation of mechanisms, no jamming or slippage in their operation.

In connection with the above for an objective assessment several evaluation criteria of these parameters should be set.

1. The maximum resolution of the sight – should differ from the calculated ideal value by more than 30 %.

2. Contrast of the transmitted image on the axis with a resolution behind the eyepiece of 1 shtr/mrad should be at least 0.4, at 1.5 shtr/mrad – at least 0.25, at 2 shtr/mrad – 0.15.

3. Contrast value of the transmitted image at the angle of the field of view of 6° should not differ from the contrast of the transmitted image by more than 50 %.

4. Transmission of the optical system must be at least 90 %.

5. Change in the position of the reticle after exposure to shock and vibration loads, as well as when working with movable elements of the sight should not exceed 0.05–0.1 mrad.

6. Thermal stabilization of the optical system at operating temperatures ±50 °C.

7. Rotation torque of the magnification change drive, parallax should not exceed 70 H·m.

Equipment and measurement methods

Control of basic optical and mechanical parameters guarantees high-quality production of a sight. To carry out such control special equipment is required that allows measuring parameters with high accuracy. The following equipment is used during operation:

1. Universal stand for optical parameters' measurind

The stand (Figure 1) allows measuring characteristics: resolution, optical magnification, diopritic detuning, contrast transfer function (CTF), transmission of the optical system, vignetting, distortion, size and removal of the exit pupil, angle of field of view, stability of the position of the sighting element (when using a special seat). Use of high-resolution video cameras and special software minimizes operator errors that will subsequently affect the final measurement result and also significantly reduces time of changes and the complexity of the process itself which is especially important in mass production.

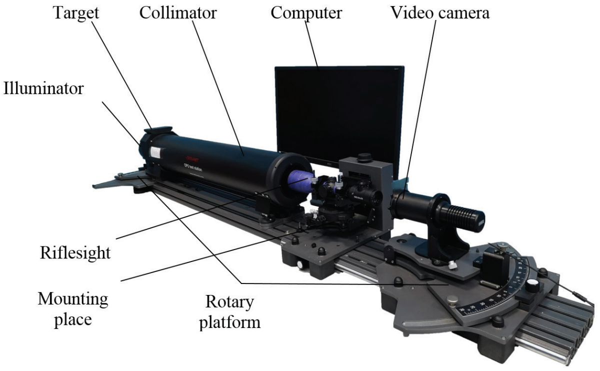

Figure 1 – Universal optical parameter control stand

One of the most important optical parameters that determine the image quality is the CTF. This parameter is more general characterizing the quality of the optical image because it shows a change in the resolution of the image transmitted by the sight depending on the decrease in contrast of the object under consideration at different angles of passage of optical rays [5].

Of course it should be taken into account that quality of the optical image directly depends on the accuracy of the manufacture of optical parts (the decentricity of the manufacture of optical elements, N – permissible sphericity and ΔN – the tolerance field of the surface shape – an interference ring or strip), as well as the accuracy of the installation of optical elements (the decentricity and inclination of the optical axis of the part relative to the axis of the optical system) [5]. Moreover depending on the features of the optical system, the values of these parameters can have a different effect on the image quality. At the same time in order to obtain a high-quality optical system and, accordingly, a device with high output characteristics, such methods should be selected that would contribute to the manufacturability of the device [6, 7].

Figure 2 shows the obtained graphs of the CTF for an optical sight of variable multiplicity with different sphericity and the tolerance field of the surface shape.

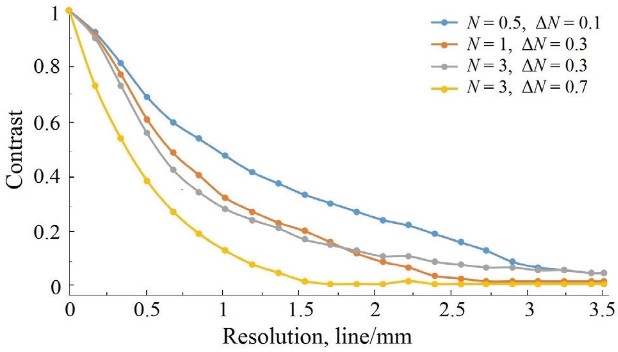

Figure 2 – Graphs of frequency-contrast characteristics with different surface manufacturing quality using the example of the GS5-25×56M1 sight

As can be seen from the graphs, the greatest contribution to improving the image quality is made by the parameter of the tolerance field of the surface shape – ΔN. In this regard, in the manufacture of optical elements, it is important that this parameter has a minimum deviation from the nominal value. Therefore the control of the tolerance field of the surface shape of optical elements is a particularly important part of the control of the parameters of parts and components of the sight.

2. Climate test chamber

Conducting climatic tests in the chamber (Figure 3*a*) implies that in addition to the already standard control of the mechanical parts of the device, such as the maximum resolution, the parallax of the sighting grid, the operation of the backlight, the removal of the aiming line, the quality and purity of coatings, it is necessary to check the sight for the thermal stability of the optical system. Stability of the parameters of the optical system in the operating temperature range is carried out at the stage of optical calculation of the sight by selecting glass grades that allow to exclude or compensate for image defocusing.

Optical sights with a thermocompensated optical system will provide a high-quality optical image and allow you to work with the sight in a larger range of temperature differences.

3. Stands for mechanical tests

Stands for mechanical tests include two types of stands – a stand of vibration loads (Figure 3*b*) and a stand of horizontal shock loads (Figure 3*c*).

On these stands preservation of mechanical and optical parameters is checked, such as the removal of the aiming line, the functioning of electronic components, the rotation of the device elements after exposure to mechanical loads simulating a shot impact and vibration during operation or transportation of the sight.

Vibration load stand allows you to simulate the conditions that arise when the sight is exposed to various kinds of vibrations that will appear during operation, and check the stability of parts, assemblies and their connections for resistance to this kind of loads. The presence of a special device for fixing the device allows moving vibrate along the axes for the most accurate simulation of the processes that occur during operation.

Shock loading stand allows creating conditions that arise when firing weapons of various capacities, and check the sight for strength to shock loads. To accurately recreate the conditions that occur when a shot is fired the stand must strike in a horizontal direction, simultaneously along the optical axis of the device.

4. Leakproofness control chamber

Control chamber which provides an adjus-table level of additional pressure, allows simulating the immersion of the sight in water to a depth of up to 30 m, which allows you to guarantee the tightness of the tested devices under hydrostatic pressure conditions. After this test the sight is subjected to dust protection and sprinkling tests.

This test confirms the full functioning and operability of the sight after exposure to high external pressure which corresponds to the IPX8.

5. Moisture protection class. Dust chamber

Dust protection test chamber of the devices is used to simulate natural weather conditions that occur during a dust storm in which the dust concentration in the chamber is 2 g/m^3, but not less than 0.1 % of the useful volume, with an ambient temperature of 50 °C, or to simulate rain conditions.

These tests make it possible to guarantee the operation of the sight after exposure to dust and the compliance of the sight with the IP6X dust protection class.

6. Torsiometer

One of the most important parameters of the sight, like any other equipment affecting the subjective assessment of the quality of the device is the softness and smoothness of the rotation of the sight elements, the absence of slippage during rotation. This parameter can be checked on a special torsiometer (Figure 3*f*) with attachments adapted for each model of the sight.

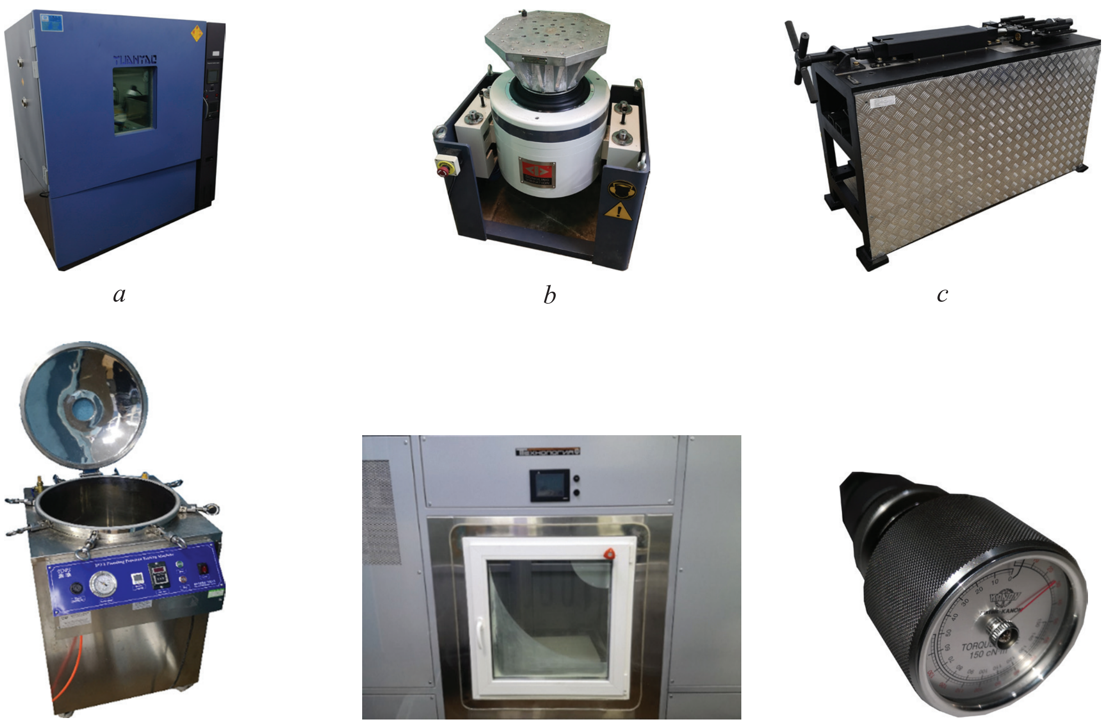

Figure 3 – Bench equipment used for the study of optical sights: *a* – climate test chamber; *b* – vibration test stand; *c* – horizontal shock load stand; *d* – immersion test chamber; *e* – dust chamber; *f* – torsiometer

The leash of the magnification change, parallactic detuning should not rotate spontaneously while working with the sight, however, for comfortable operation of the operator, the rotation moment of these elements for their diameter should not exceed 70 H·m.

The main parameters of the sights created and serially mastered at the STC "LEMT", which are successfully exported including highly developed countries are shown in Table vignetting and CHKX graphs for maximum and minimum magnifications are shown in Figures 4, 5 and 6, respectively.

Table

The main parameters of sights

Type of control and testing	Test parameters				
	GS3-12×50	GS5-25×56M1	GS3-24×56	GS1-8×24	GS1-8×24FFP
Magnification	3–12	5–25	3–24	1–8	1–8
Control of critical lens surfaces	$N = 3$ $\Delta N = 0.3$	$N = 2$ $\Delta N = 0.3$	$N = 3$ $\Delta N = 0.3$	$N = 5$ $\Delta N = 0.5$	$N = 5$ $\Delta N = 0.5$
Shock loads	450 g 1–2 ms	600 g 1–2 ms	450 g 1–2 ms	450 g 1–2 ms	450 g 1–2 ms
Vibration loads	4 g 20–80 Hz 4 g 25 Hz				
Withdrawal of the aiming line	0.1 mrad	0.05 mrad	0.1 mrad	0.1 mrad	0.1 mrad
Transmition	Not less 85–90 %				
Field of view	6.3° 1.95°	3.1° 0.85°	6.6° 0.85°	20° 2.7°	20° 2.7°
Exit pupil diameter	10 mm 3 mm	10 mm 2.1 mm	9 mm 2.3 mm	9.5 mm 3 mm	9.5 mm 3 mm
Thermal loads	-40 °C – +50 °C				
Dust and moisture protection	IP68	IP68	IP67	IP67	IP68
Rotation force of the elements	70 N·m				
Alignment flywheel pitch	0.1 mrad				

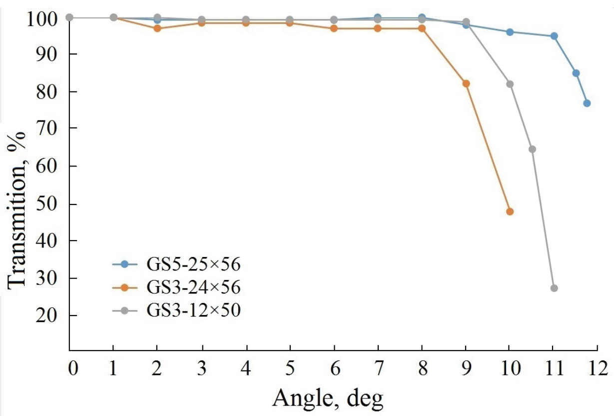

Figure 4 – Vignetting graph of GS3-24×56, GS5-25×56, GS3-12×50 sights at maximum magnification

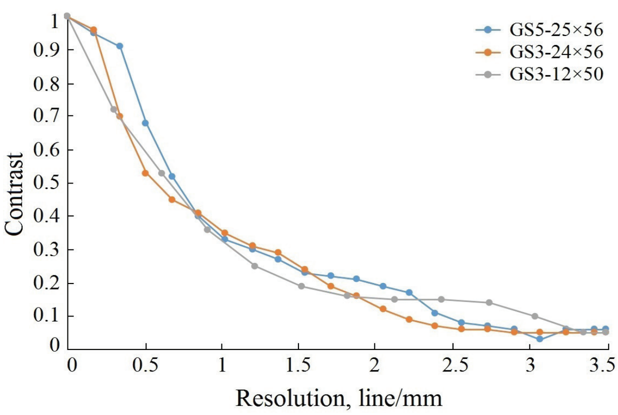

Figure 5 – Plot of the GS3-12×50, GS3-24×56, GS5-25×56 scopes at maximum magnification

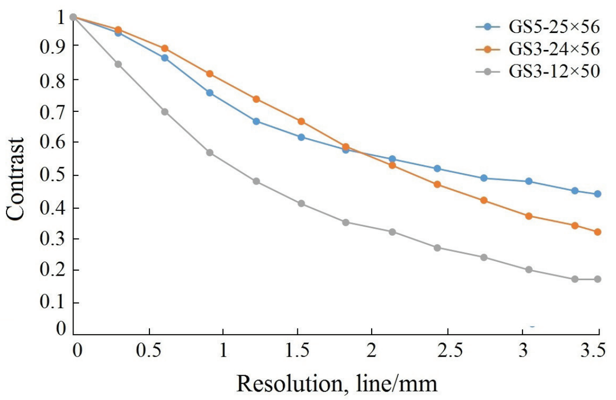

Figure 6 – Plot of the GS3-12×50, GS3-24×56, GS5-25×56 scopes at minimum magnification

Technological aspects of creating modern-level sights are due to the optimization of the manufacture of optical and mechanical parts, the assembly and alignment process, as well as quality control. At the same time the manufacturability and design of the sight is carried out taking into account the available equipment for processing and monitoring parts assemblies and the entire sight as a whole [8]. A special role is given to the choice of the method of fastening parts, optimizing the mechanical processes of applying both optical and mechanical coatings as well as ensuring the purity of the field of view and the absence of scree on all optical elements of the device. However the issue of high image quality of optical sights is solved not only by correcting the decentering and inclination of the optical elements relative to the common optical axis, but also by using high-quality glass, high precision processing of optical elements, matching the position of the optical elements of the pancratic system with the calculated magnification changes and the quality of the antireflection coatings of the optical surfaces of the sight [9].

Conclusion

High optical quality (an optical system can be considered of higher quality if the contrast at the same magnification of the optical system at the same resolution value is higher than the one being compared however for simple distinction the od should not be less than 0.2) can be manufactured only if the manufacturing processes are followed by careful element-by-element and operational control their parameters. Mechanical quality of the device (the absence of jamming during the rotation of the sight elements, as well as sufficient force for rotation – 70 H·m) important also. It is necessary to guarantee the preservation of these parameters at large temperature differences of the external environment – from minus 40 °C to plus 60 °C, high mechanical loads – impacts with acceleration 350–500 g which corresponds to acceleration 3432.3–4905.3 m/s^2.

Compliance with these requirements allows us to withstand all the tests imposed by the modern level of development of small arms and in some cases exceed the requirements for some fundamental parameters for small arms – accuracy of firing (0.2 angular minutes), immutability of the position of the aiming element – grid, stability in a wide range of temperatures which allows us to compete with the world's leading models produced by famous manufacturers.

References

1. Darko D. Jankovic, Darko M.Vasiljevic, Ljubisa D. Tomic, Sedan J. Duvnjak. Modern sniper rifles in the armament of the Serbian armed Forces. *Vojnotehnicki glaznik*, 2019, vol. 67, no. 3, pp. 663–688. **DOI:** 10.5937/vojtehg67-18141

2. Filipov M.A. On the wagging of the muzzle velocity of a bullet on the accuracy of sniper rifle shooting. *Proceedings of Tula State University. Technical Sciences*, 2018, pp. 241–249 (in Russian).

3. Belsky A.B. Pankratic sniper sights of the new generation. *Questions of Defense Technology*, 2009, no. 9–10, series 16 (in Russian).

4. Kiselyov Al.S., Kiselyov An.S., Nazarov V.N. Investigation of the influence of errors in the assembly and alignment of optical sights on the result of shooting. *Federal State Autonomous Educational Institution of Higher Education "St. Petersburg National Research University of Information Technologies, Mechanics and Optics"*, 2006, pp. 150–155 (in Russian).

5. INFRAMET. OPO-Z test station. Manual. Tester of telescopic sight, Poland, 2018.

6. Sosnov A.N., Sosnova N.K., Kritinina S.V. Optical methods for error control of manufacturing precision cylindrical lenses. Interexpo Geo-Siberia Publ., 2008.

7. Bao Bui Dinh, Latyev S.M., Theska R. Automation of lenses centering at gluing in the frame. *Scientific and Technical Bulletin of Information Technologies, Mechanics and Optics*, 2015, vol. 15, no. 6, pp. 1030–1035 (in Russian). **DOI:** 10.17586/2226-1494-2015-15-6-1030-1035

8. Latyev S.M. Design of precision (optical) instruments. St. Petersburg: Polytechnic Publ., 2007, 580 p.

9. Latyev S.M., Bao Bui Dinh. Methods of lens centering in optical systems. News of higher educational institutions. *Izvestiya Vysshikh Uchebnykh Zavedeniy. Priborostroenie* [Instrumentation], 2013, vol. 56, no. 11, pp. 66–72 (in Russian).

Development of Engineering Models of Nanosatellites for Student Training

V.E. Evchik, A.A. Spiridonov, D.V. Ushakov, V.S. Baranova, I.A. Shalatonin, V.A. Saechnikov

Belarusian State University,
Nezavisimosti Ave., 4, Minsk 220030, Belarus

Received 27.04.2022
Accepted for publication 06.09.2022

Abstract

The work purpose is the development of BSUIM-1 and BSUIM-2 complexes for training specialists in the aerospace industry with the used engineering test beds and experimental facilities.

Two sets of nanosatellite engineering models and ground stations had developed. They allow testing hardware and software of the onboard equipment and payload, simulating operation modes, and flight programs, and enable students to gain practical skills in working with ultra-small satellites. The complexes include ground stations, 2 ultra-small satellite simulators, BSUSAT-1 low-orbit nanosatellite, remote access laboratory, local and external servers for data storage. The complexes' website and database allow for full-time and remote training. The experience gained in conducting experiments, processing telemetry, and structuring information in the database is used for further development. All the developed equipment is made based on commercial off-the-shelf elements. It has reduced development costs, flexible equipment reconfiguration, and easier access to the simulator's internal architecture for demonstration purposes.

The developed complexes allow students to practically study the ultra-small satellite components design and ground stations, methods for receiving and processing telemetry and scientific information, attitude determination and control algorithms. The complexes allow to conduct of research in the development of individual onboard systems and special-purpose equipment of the nanosatellite and their testing in the loop.

The results obtained are introduced into the educational process and are used in lectures and laboratory classes for aerospace specialties students. The developed complexes make it possible to carry out term papers, theses, and master's works related to the design of hardware and software for nanosatellites and a ground station, the setting up of space experiments, the development of new algorithms and a flight program for ultra-small satellites.

Keywords: nanosatellite, Cubesat, ground station, education, onboard systems.

DOI: 10.21122/2220-9506-2022-13-3-172-179

Адрес для переписки:
Евчик В.Е.
Белорусский государственный университет,
пр-т Независимости, 4, г. Минск 220030, Беларусь
e-mail: slava97evev@gmail.com

Address for correspondence:
Evchik V.E.
Belarusian State University,
Nezavisimosti Ave., 4, Minsk 220030, Belarus
e-mail: slava97evev@gmail.com

Для цитирования:
V.E. Evchik, A.A. Spiridonov, D.V. Ushakov, V.S. Baranova, I.A. Shalatonin, V.A. Saechnikov.
Development of Engineering Models of Nanosatellites for Student Training.
Приборы и методы измерений.
2022. – Т. 13, № 3. – С. 172–179.
DOI: 10.21122/2220-9506-2022-13-3-172-179

For citation:
V.E. Evchik, A.A. Spiridonov, D.V. Ushakov, V.S. Baranova, I.A. Shalatonin, V.A. Saechnikov.
Development of Engineering Models of Nanosatellites for Student Training.
Devices and Methods of Measurements.
2022, vol. 13, no. 3, pp. 172–179.
DOI: 10.21122/2220-9506-2022-13-3-172-179

Разработка инженерных моделей наноспутников для обучения

В.Е. Евчик, А.А. Спиридонов, Д.В. Ушаков, В.С. Баранова, И.А. Шалатонин, В.А. Саечников

Белорусский государственный университет,
пр-т Независимости, 4, г. Минск 220030, Беларусь

Поступила 27.04.2022
Принята к печати 06.09.2022

Целью работы являлась разработка комплексов для подготовки специалистов аэрокосмических специальностей на основе практических тренажёров и экспериментальных установок.

Разработаны два комплекса инженерных моделей-имитаторов наноспутников и наземные станции приёма, которые позволяют проводить отработку оборудования и программного обеспечения бортовой аппаратуры и полезной нагрузки, имитацию режимов работы, программы полёта, дают возможность студентам получать практические навыки работы со сверхмалыми космическими аппаратами. Комплексы включают в себя: наземные станции приёма, 2 имитатора сверхмалых космических аппаратов, низкоорбитальный спутник BSUSAT-1, лабораторию удалённого доступа, локальный и внешний серверы для сбора и хранения данных. Собственный веб-сайт комплексов и база данных позволяет обеспечить как очное, так и удалённое проведение лабораторных работ. Полученный опыт в проведении экспериментов, обработки телеметрии и структурированная в базе данных информация используется для дальнейших разработок. Всё разработанное оборудование выполнено на основе доступной элементной базы. Это позволило снизить стоимость разработки, гибко реконфигурировать оборудование и облегчить доступ к внутренней архитектуре тренажёров для демонстрации.

Разработанные комплексы позволяют студентам практически изучать устройство сверхмалых космических аппаратов и наземных станций приёма, методы приёма и обработки телеметрии и научной информации, алгоритмы определения положения и управления спутником. Комплексы позволили проводить исследования в области разработки отдельных бортовых систем и целевой аппаратуры наноспутника и последующего их тестирования.

Полученные результаты внедрены в учебный процесс и используются при чтении лекций и проведении лабораторных занятий для студентов аэрокосмических специальностей. Разработанные комплексы позволяют выполнять курсовые, дипломные и магистерские работы, связанные с проектированием программно-аппаратных средств наноспутников и наземной станции, постановкой космических экспериментов, разработкой новых алгоритмов и программы полёта сверхмалого космического аппарата.

Ключевые слова: наноспутник, Cubesat, наземный комплекс управления, обучение, бортовые системы.

DOI: 10.21122/2220-9506-2022-13-3-172-179

Адрес для переписки:
Евчик В.Е.
Белорусский государственный университет,
пр-т Независимости, 4, г. Минск 220030, Беларусь
e-mail: slava97evev@gmail.com

Address for correspondence:
Evchik V.E.
Belarusian State University,
Nezavisimosti Ave., 4, Minsk 220030, Belarus
e-mail: slava97evev@gmail.com

Для цитирования:
V.E. Evchik, A.A. Spiridonov, D.V. Ushakov, V.S. Baranova,
I.A. Shalatonin, V.A. Saechnikov.
Development of Engineering Models of Nanosatellites
for Student Training.
Приборы и методы измерений.
2022. – Т. 13, № 3. – С. 172–179.
DOI: 10.21122/2220-9506-2022-13-3-172-179

For citation:
V.E. Evchik, A.A. Spiridonov, D.V. Ushakov, V.S. Baranova,
I.A. Shalatonin, V.A. Saechnikov.
Development of Engineering Models of Nanosatellites
for Student Training.
Devices and Methods of Measurements.
2022, vol. 13, no. 3, pp. 172–179.
DOI: 10.21122/2220-9506-2022-13-3-172-179

Introduction

There are currently dozens of leading manufacturing companies that provide both off-the-shelf onboard systems for CubeSats [1, 2], CubeSat simulators [3, 4], and complete satellites. It is common practice for developers to create their modules based on commercial off-the-shelf elements. This method provides the most effective compliance with the technical and operational requirements of the CubeSats. To confirm the performance and specified technical characteristics of the developed equipment or onboard system, it is necessary to conduct preliminary testing [5–7]. Comprehensive tests are performed in the joint operation of onboard systems and the ground control complex.

There are many engineering debugging models of nanosatellites [8–9]. For example, the Pumpkin CubeSat debug kit of the American company Pumpkin Ink [10] has a control system, data acquisition and processing, a communication system, and an expansion board with RS-232, USB PCI/ISA interfaces for the payload. But in the tested set, there are no attitude determination and control system (ADCS) and full-fledged power supply system. It does not allow comprehensive testing of all satellite systems in various operating modes. Also, this complex lacks additional interfaces, such as I2C, SPI, CAN, and RS-422/485, widely used in satellites. Another disadvantage of this kit is the lack of redundant systems. All this reduces the reliability of equipment testing.

The EyasSat nanosatellite engineering educational model [11] serves as a full-fledged demonstration model. It allows for conducting laboratory classes in the process of specialist training and retraining in the aerospace industry. This model can be used in the control algorithms of the development and educational programming of attitude dermination and control systems [12]. However, it is impossible to test the engineering model's components and the onboard system in various operation modes. But the main EyasSat engineering model disadvantage is the onboard systems redundancy lack.

This paper describes the technical features and capabilities of 2 practical and affordable test bed nanosatellite simulators – BSUIM-1 and BSUIM-2. The development and implementation were realized at the Faculty of Radiophysics and Computer Technologies Belarusian State University supported by the scientific research Republic of Belarus State programs "High-tech technologies and equipment" "Digital and space technologies, human, society and state security". The nanosatellite simulator's structural and hardware components are also considered as the education courses part.

BSUIM-1 on-board systems

First, the test bed BSUIM-1 is considered. This complex includes following software and hardware elements: remote control system (RCS); engineering nanosatellite model – nanosatellite simulator; software and information center for the development of onboard equipment; laboratory workshop "On-board systems and nano- and pico-satellites ground system".

The engineering model schematic diagram shows in Figure 1. The nanosatellite engineering model has a non-hermetic design, a vertical layout and consists of modules that simulate the operation of the basic onboard systems: onboard computer; communication system; electric power system; ADCS; interfaces module; payload. The primary purpose of this engineering model is to provide full-loop nanosatellite designing, onboard systems and payload verification in operation mode, conducting experiments on testing the equipment of the ground control center. It suggests use for practical education aerospace specialists.

The main engineering model onboard systems – the control system (onboard computer) and the communication module have been duplicated to ensure reliability. The remote control feature of onboard systems provides: power on/off, software operating modes switching depending on the onboard systems state; independent subsystems controlled by user commands. The control channels of the nanosatellite technical model have been duplicated using the main onboard computer (based on the industrial computer CM-720) and the backup computer (based on the STM32F429 microcontroller). Channels for receiving commands and transmitting telemetry to the ground station had implemented using two identical transceiver models TE-CC430F51-433 and an additional GSM modem. The nanosatellite engineering model has a primary MNP-M7 GPS receiver and a backup uBlox neo6-M GPS module to improve the accuracy of time stamps during testing.

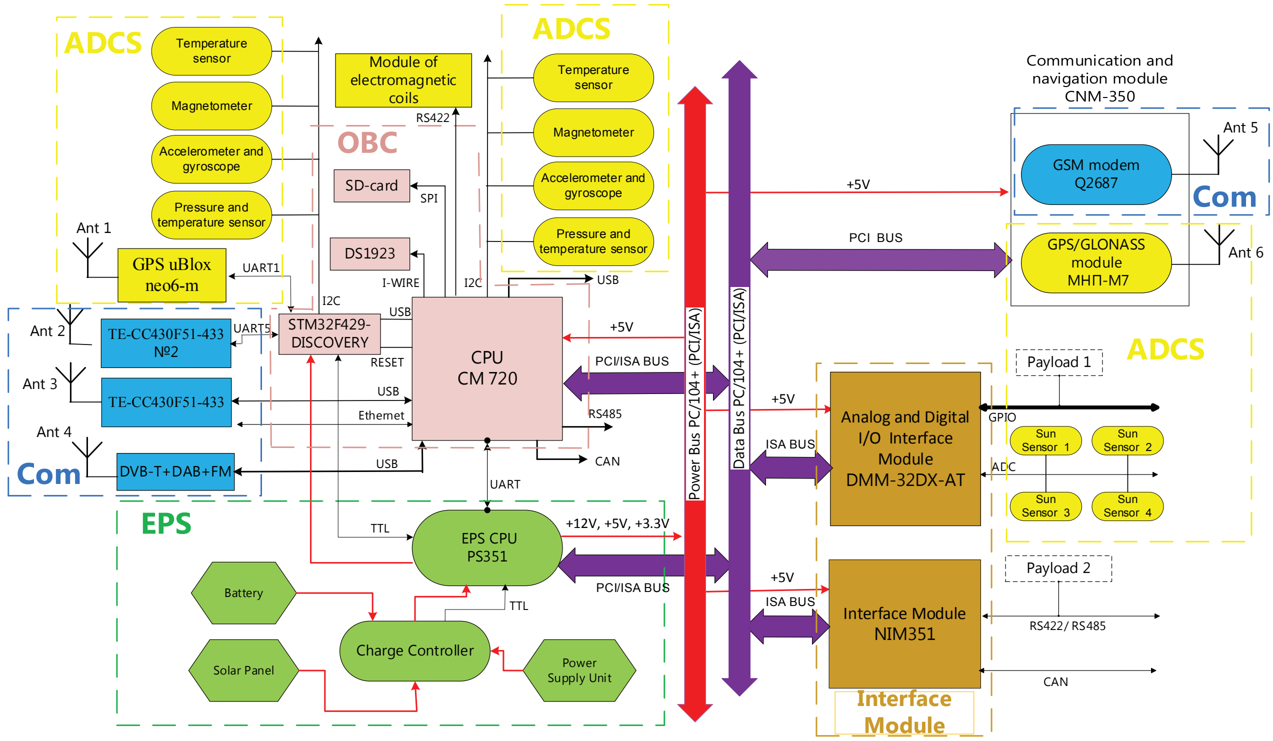

Figure 1 – The BSUIM-1 systems flowchart

Ground station of BSUIM-1

The remote control system (RCS) is a ground station for control and reception. It can receive telemetry and special-purpose information from the orbited ultra-small satellite. It also makes it possible to simulate the operation of the ground satellite control in co-verification with the BSUIM-1 nanosatellite simulator. The remote control system allows to generate and transmit control commands to the BSUIM-1 nanosatellite simulator, receive, process, and display response data packets on the control commands execution, telemetry, and payload information. It also makes it possible to config of an operating model of the satellite onboard equipment or the tested equipment on the simulator as a part of modeling routine work with the satellite.

The RCS includes software and hardware for working with orbited ultra-small satellites: transceiver IC-9100; antenna-feeder devices of the command-telemetry radio link; power amplifiers; modems; control computer with software; uninterrupted power supply; and a mobile module of the remote control system for testing on-board systems and payloads with the BSUIM-1 nanosatellite simulator in the loop.

The equipment of the RCS mobile module is duplicated to ensure reliability. The channels of the BSUIM-1 nanosatellite simulator for receiving telemetry and control duplicates by the main and backup mobile modules of the RCS. Also, in each of the RCS mobile modules, two transceivers based on the CC430 radio module (main and backup) are used. The remote control system features a user-friendly graphical interface for displaying command and telemetry information, voicing the main parameters of the simulator, transferring and storing data on the local and remote servers of the BSUIM-1 nanosatellite simulator [13] www.satellite.by.

For convenient operation, the special graphical user interface of the remote control system was developed [14]. It consists of two main panels – the Control Panel and the Telemetric Information Display Panel. The control panel allows flexible control of the onboard systems and payload of the BSUIM-1 nanosatellite simulator both using a large set of ready-made commands and commands developed by users. The telemetry panel displays raw telemetry packets in JSON format and structured (decoded) telemetry for onboard systems and the payload of the BSUIM-1 nanosatellite simulator. Each system has separate tabs with decoded information.

BSUIM-2 on-board systems

The second BSUIM-2 test bed complex includes:

– laboratory test bed simulating the onboard systems operation of an ultra-small satellite (onboard computer, attitude determination and control system, communication system, electric power system and payload) and ground control station;

– telemetry database of orbited ultra-small satellites and software for primary and secondary telemetry processing;

– hardware of remote access laboratory for simulator control, data transmission and data processing based on packet and web servers, transceivers and antenna-feeder systems;

– remote access laboratory website;

– a set of educational and methodological materials for training specialists in the areas of "Ground stations" and "Spacecrafts".

The second test bed allows to include in the architecture of the remote access laboratory, shown in Figure 2, a nanosatellite simulator made in the Cubesat 2U standard, the first test bed BSUIM-1 with a nanosatellite simulator and BSU's low-orbit nanosatellite "CubeBel-1" for training [15].

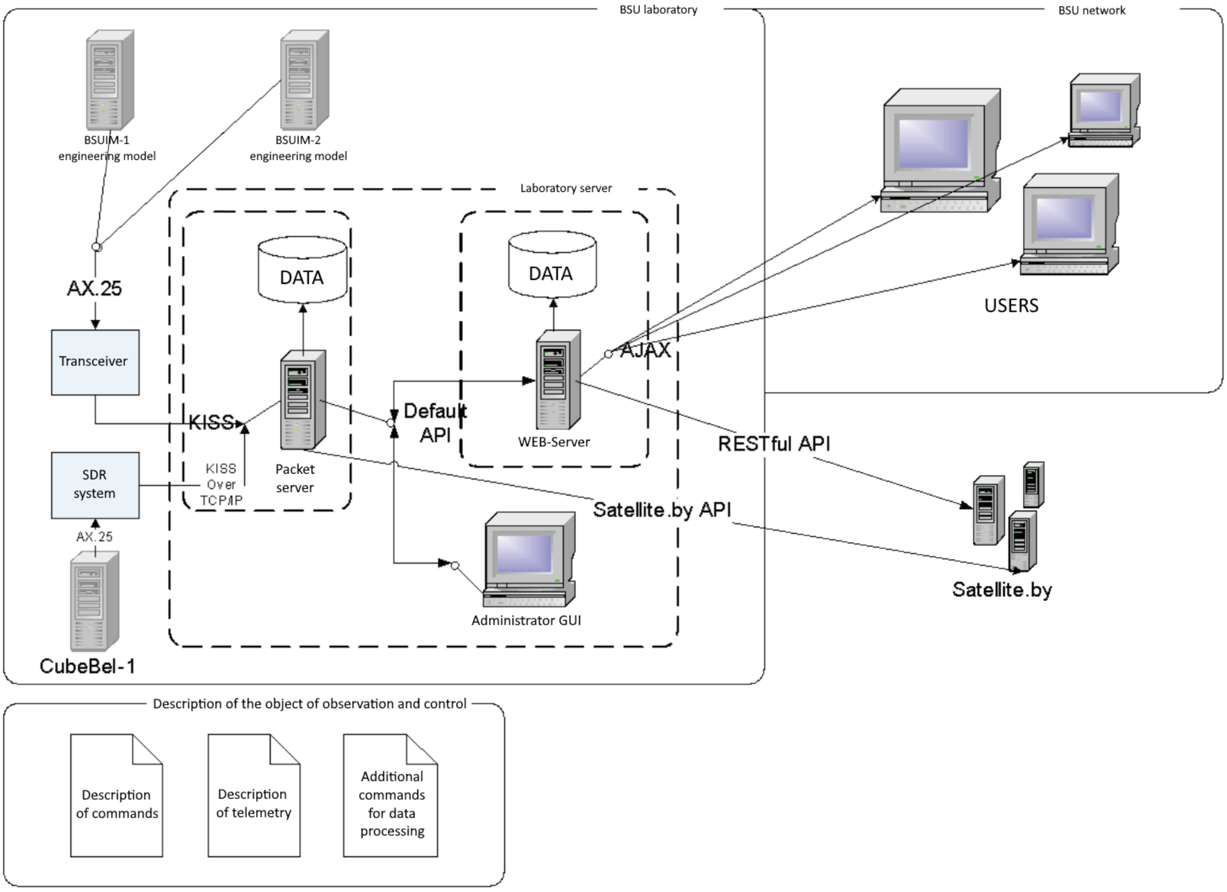

Figure 2 – Remote access laboratory architecture

The hardware part of the BSUIM-2 nanosatellite simulator systems is shown in Figure 3. It is made on a non-radioresistant element base and includes all the main onboard systems of an operated ultra-small satellite:

– two onboard computers based on STM32 ARM microcontrollers (main and backup);

– two onboard communication modules (main and backup) based on Si4463 transceivers and antennas;

– attitude determination and control system [16] based on: navigation module Lacosys MC1620; accelerometers and gyroscopes [17] (MPU-9250 and MPU-6050), pressure and temperature sensors (BMP280); magnetometers [18–20] (MAG3110 and MPU-9250); component parts of the stabilization system (electromagnetic coils);

– electric power system based on: rechargeable batteries; power regulators; solar cells.

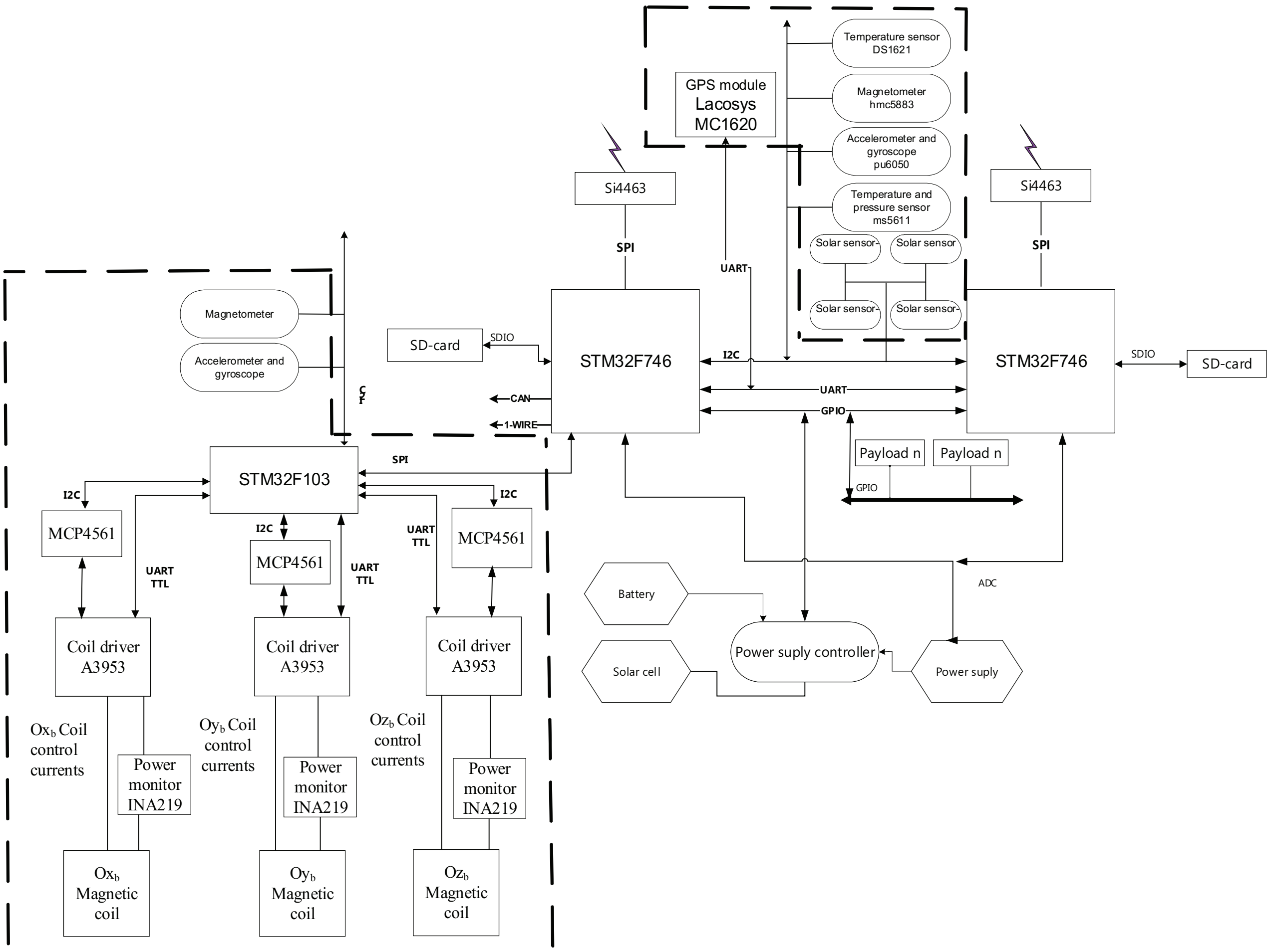

Figure 3 – The BSUIM-2 systems flowchart

Systems that simulate the operation of the ultra-small satellite onboard systems perform the following functions: power supply of onboard systems in all modes of operation; formation of regulated voltages 3.3 V, 5 V, 12 V; control of systems performance; systems configuration; packets formation for transmitting information over a radio channel; time binding of commands and parameters to onboard time; exchange of information with onboard systems via I2C, SPI, USB, CAN interfaces, through analog and digital input/output ports.

Ground station of BSUIM-2

Nanosatellite simulators have a core communication system for receiving commands and transmitting telemetry. Moreover, the provided backup system can replace the main one in a crash case. The communication system sends the telemetry data to the ground station in the form of nested association lists in MsgPack format using the AX.25 protocol [21]. The communication systems for each nanosatellite simulator have the same call sign but different SSIDs. Ground station transceivers are based on MSP430 microcontrollers [22] with KISS protocol control [23]. Commands for nanosatellite simulators are also association lists. The stack method uses to send them. Reception of telemetry from the orbited satellite CubeBel-1 provides by the SDR system [24]. It uses the existing UZ7HO sound modem software. It supports receiving packets using the KISS protocol over TCP/IP.

To support many different protocols for interaction with various orbited satellites (including those with one-way communication), the concept of a stack is introduced. The stack includes a set of protocols at different levels of interaction, similar to the OSI model [25]. For each stack variant specified by the configuration, a separated software component is launched that provides interaction with the satellites through the specified stack on the one hand with the package server core in a standard format on the other. Every protocol implementation on the stack can be reused. This allows multiple satellites to be supported at minimal cost.

Devices and Methods of Measurements
2022, vol. 13, no. 3, pp. 172–179
V.E. Evchik et al.

On the other hand, the batch server interacts with a number of different clients using different APIs. Some of them are defined as a single client (separate web server of a laboratory or collaborating university, local admin GUI). For some, only data transfer is used (for example, for Satellite.by). To support such a variety of clients, special modules are used that extend the Packet Server API and provide telemetry distribution tools (both for a specific client and for all clients at once).

The discussion of the results

Engineering model test beds (simulators of nanosatellites) for teaching students the basics of working with ultra-small satellites are considered. The possibility of checking the operating modes, flight program, hardware, and software of the onboard equipment and payload is described. The advantage of the developed complexes is the principle of modularity. It allows for the addition or changes onboard modules and payloads of simulators for debugging and testing the simulator/satellite firmware without creating a new expensive engineering model. The second advantage is the ability to study various algorithms and programs for the simulator operation (onboard systems and the payload) in various modes typical for a real flight [26]. Moreover, the flexible software of the simulator and the ground station provides the possibility of modifying.

The core function of the complexes is to train new specialists for further work with operated satellites and ground stations. Thanks to the complex, it is possible to train specialists in several areas: satellite design; design of special-purpose and scientific equipment; satellite onboard systems design; development of ground stations; design and conduct of scientific experiments [27]; receiving and processing telemetry; dynamics, ballistics, satellite motion control; navigation and orientation devices [28].

In addition to studying nanosatellites, the complex allows students to gain practical skills in working with ground stations: study their structure, software and hardware and remote control methods [29]. It also allows students to learn the basics of receiving, transmitting, modulating, encoding and encrypting data. The developed complexes make it possible to study various configurations of ground stations. So, for example, with the help of an amateur radio RTL-SDR, you can assemble additional radio receiving stations for working with simulators [30].

Conclusion

The developed complexes make it possible to carry out term papers, graduate works and master's thesis related to the design of hardware and software for nanosatellites and a ground station, the setting up of space experiments, the development of new algorithms and the flight program of an ultra-small satellite.

The results obtained are introduced into the educational process and are used in lectures and laboratory classes for students of aerospace specialties of BSU.

References

1. Khanov V.Kh., Shakhmatov A.V., Chekmarev S.A., Lepeshkina E.S. CubeSat onboard control system on the base of "system-on-chip" technology. *Journal of Instrument Engineering*, 2018, vol. 6, no. 5, pp. 403–408. **DOI:** 10.17586/0021-3454-2018-61-5-403-408

2. Davoli F., Kourogiorgas C., Marchese M., Patrone F. Small satellites and CubeSats: Survey of structures, architectures, and protocols. *International Journal of Satellite Communications and Networking*, 2019, vol. 37, no. 4, pp. 343–359. **DOI:** 10.1002/sat.1277

3. Chin Jamie, Coelho Roland, Foley Justin, Johnstone Alicia. Basic Concepts and Processes for First-Time CubeSat Developers. CubeSat101, CaliforDesign of a CubeSat Testbednia, 2017, 96 p.

4. Shiroma W.A., Martin L.K., Akagi J.M., Akagi J.T. CubeSats: A bright future for nanosatellites. *Central European Journal of Engineering*, 2011, vol. 1, no. 1, pp. 9–15.

5. Tavakoli A., Faghihinia A., Kalhor A. An Innovative test bed for verification of attitude control system. *IEEE Aerosp. Electron. Syst. Mag*., 2017, vol. 32, no. 6, pp. 16–22. **DOI:** 10.1109/MAES.2017.150198

6. Hurtado J., Goecks V.G., Probe A. Low-Cost Satellite Attitude Hardware Test Bed. In Proceedings of the ASEE Annual Conference and Exposition, New Orleans, LA, USA, 26–29 June 2016.

7. Edries M.Y., Tanaka A., Cho M. Design and Testing of Electrical Power Subsystem of a Lean Satellite, HORYU-IV. Trans. *Jpn. Soc. Aeronaut. Space Sci. Aerosp. Technol. Jpn*, 2016, vol. 14, no. 30, pp. 7–16.

8. Volodin K.I., Krohin I.A., Pahomov S.A. Cubesat-R – yet another modular educational kit for everybody. *Modern Information Technologies*, 2015, vol. 21, pp. 182–184.

9. Tanaka T., Kawamura Y., Tanaka T. Overview and operations of CubeSat FITSAT-1 (NIWAKA). *6th International Conference on Recent Advances in Space Technologies (RAST)*, 2013, pp. 887–892.
DOI: 10.1109/RAST.2013.6581339

10. Kalman A.E.. Overview of the CubeSat Kit. Pumpkin Inc., 2004, 30 p.

11. Barnhart D.J., Sellers J.J. EyasSat-cubed: a Low-cost On-ramp for Nanosatellite Programs. AIAA SPACE 2013 Conference and Exposition, San Diego, 2013.
DOI: 10.2514/6.2013-5325

12. Groenewald C.J. Attitude Determination and Control System for EyasSAT for Hardware In the Loop Application. Stellenbosch University Department of Electric and Electronic Engineering, 2014, 180 p.

13. Shalatonin I.A., Spiridonov A.A., Saechnikov V.A., Volkov A.V., Dombrovski V.V., Sacuta D.V., Koltun B.V., Stankevich D.S., Orlov O.A., Graevski V.V. Hardwares and softwares testing for nanosatellites laboratory development. Complex problems of technosphere safety, State educational establishment of higher professional education Voronezh state technical University, 2016, pp. 70–73.

14. Hryny D.N., Dombrowski V.V., Koltun B.V., Saechnikov V.A. , Spiridonov A.A. , Shalatonin I.A. Software of information complex for testing onboard systems and scientific equipment of nanosatellites. *Fundamental problems of system security*, Sevastopol, September 13–15, 2017, pp. 74–79.

15. Spiridonov A.A., Saechnikov V.A., Ushakov D.V., Kezik A.G., Cherny V.E., Verstakovskaya A.P., Evchik V.E. Research and educational network of ground stations for receiving and processing information from educational satellites. IOP Conference Series: Materials Science and Engineering.
DOI: 10.1088/1757-899X/966/1/012104

16. Evchik V.E., Samonov P.V., Saechnikov V.A., Spiridonov A.A., Ushakov D.V. Attitude determination and control system for nanosatellite simulator. Materials of the II International scientific-practical conference “Computer technologies and data analysis” (CTDA’2020), April 23–24, 2020, Minsk, pp. 233–237.

17. Zielinski B.M. Effective throughput of AX.25 protocol. *Bulletin of the Polish Academy of Sciences, Technical Sciences*, 2013, vol. 61, no. 3, pp. 639–647.
DOI: 10.2478/bpasts-2013-0068

18. Paci D., Cantoni A., Allegato G. Magnetometers. *Silicon Sensors and Actuators*, 2022, pp. 477–501.
DOI: 10.1007/978-3-030-80135-9_14

19. Hajiyev C., Soken H. In-Orbit Calibration of Small Satellite Magnetometers. *Fault Tolerant Attitude Estimation for Small Satellites*, 2020, pp. 277–316.
DOI: 10.1201/9781351248839-17

20. Yakupoglu S., Esit M., Soken H., Hajiyev C. Backup Magnetometer-Only Attitude Estimation Algorithm for Small Satellites. *IEEE Sensors Journal*, 2020, vol. 22, iss. 13, pp. 13544–13551.
DOI: 10.1109/JSEN.2022.3175261

21. Borik S., Babusiak B., Cap I. Device for Accelerometer and Gyroscope Measurements. *Information Technologies in Biomedicine*, 2014, vol. 4, pp. 139–146.
DOI: 10.1007/978-3-319-06596-0_13

22. LaMeres B.J. The MSP430. Embedded Systems Design using the MSP430FR2355 LaunchPad™. *Springer*, *Cham*, 2020, pp. 143–161.
DOI: 10.1007/978-3-030-40574-8_4

23. Ahmad Y.A., Nazim J., Yuhaniz S. Design of a terminal node controller hardware for CubeSat tracking applications. *IOP Conference Series: Materials Science and Engineering*, 2016, vol. 152, no. 1, p. 012031.
DOI: 10.1088/1757-899X/152/1/012031

24. Verstakovskaya A.P., Evchik V.E., Kezik A.G., Saechnikov V.A., Solovyov S.A., Spiridonov A.A., Ushakov D.V., Cherny V.E. Ground station for receiving telemetry and determining the orbit of an ultra-small satellites. Materials of the II International scientific-practical conference “Computer technologies and data analysis” (CTDA’2020), April 23–24, 2020, Minsk, pp. 224–228.

25. Mohammed M.A. OSI model. *Guide to OSI and TCP/IP Models*, 2014, pp. 5–17.
DOI: 10.1007/978-3-319-05152-9_2

26. Martínez Ú., Bravo L., Gligor D., Olfe K. Attitude control research with educational nanosatellites. A: “4th Symposium on Space Educational Activities”. Universitat Politècnica de Catalunya, 2022.
DOI: 10.5821/conference-9788419184405.032

27. Colombo C., Scala F., Trisolini M. CubeSat Mission Concept for Environmental Analysis in Low Earth Orbit. 72nd International Astronautical Congress (IAC 2021), Dubai, 2021, 15 p.

28. Modenini D., Bahu A., Tortora P. Nanosatellite-class dynamic attitude simulator for hands-on aerospace control education. *IFAC-PapersOnLine*, 2021, vol. 54, iss. 12, pp. 38–42.
DOI: 10.1016/j.ifacol.2021.11.007

29. Monowar M.I., Cho M.. Over-the-Air Firmware Update for an Educational CubeSat Project. *International Review of Aerospace Engineering (IREASE)*, 2021, vol. 14, no. 1, p. 39.
DOI: 10.15866/irease.v14i1.19832

30. Maheshwarappa M.R., Bridges C.P. Software defined radios for small satellites. NASA/ESA Conference on Adaptive Hardware and Systems (AHS), UK, 2014, pp. 172–179.
DOI: 10.1109/AHS.2014.6880174

Correction of the Contribution of Scattered Photon Radiation to the Ionization Chamber Readings During X-Ray Radiation Quality Assessment

A.A. Zaharadniuk[1,2], K.G. Senkovsky[1], R.V. Lukashevich[1]

[1]*SPE "ATOMTEX",*
Gikalo str., 5, Minsk 220005, Belarus

[2]*Belarusian State University,*
Nezavisimosty Ave., 4, Minsk 220030, Belarus

Received 27.06.2022
Accepted for publication 23.09.2022

Abstract

Reduction of the systematic error when determining the characteristics of the reference X-ray radiation fields is an essential task according to the ISO 4037-1:2019 standard. This task is especially important in dosimetry laboratories when establishing the qualities of reference photon fields. The aim of the study was to develop a method that allows taking into account the contribution of radiation scattered on the filter when determining the half-value layer of the photon field generated by the X-ray unit. Another goal was to reduce the computational cost of determining this contribution.

One of the major contributors to the systematic error in measuring the half-value layer is the radiation scattered on the filter material. The standard recommends that this error should be taken into account in the measurement. But it does not provide any methodology that would do this.

The study investigated the possibility of reducing the contribution of scattered radiation to the ionization chamber readings when assessing the radiation quality of the X-ray unit by the means of half-value layer. The study utilized the (N, H, L) quality series as reference fields according to ISO 4037-1:2019.

Contribution of the scattered radiation to the half-value layer was compensated with the correction coefficients; they were calculated with the FLUKA Monte Carlo software according to the zero-aperture approximation method. Unlike other similar methods, the proposed approach employs kinetic energy released to matter (kerma), to air in this case, as the main value, which, when utilized instead of deposited energy, reduces the program's runtime several fold.

Correctness of the results obtained in this work was verified by comparing the calculated values of the half-value layer with the tabulated ones provided in the ISO 4037-1:2019 standard. The deviation of calculated values from those specified in the standard does not exceed 2 %.

Calculation results showed that the error contributed by scattered radiation to the magnitude of the half-value layer in direct measurements does not exceed 5 %. The use of the air kerma allowed us to significantly reduce the time for calculating the correction coefficients by the factor of 6–16 times with respect to other methods, depending on the radiation quality series. This made it possible to calculate correction factors for the source-detector distance equal to 2.5 meters.

Keywords: Monte Carlo method, X-ray apparatus, scattered radiation.

Адрес для переписки:
Загороднюк А.А.
УП «АТОМТЕХ»,
ул. Гикало, 5, г. Минск 220005, Беларусь
e-mail: fiz.zagorodnAA@gmail.com

Address for correspondence:
Zaharadniuk A.A.
SPE "ATOMTEX",
Gikalo str., 5, Minsk 220005, Belarus
e-mail: fiz.zagorodnAA@gmail.com

Для цитирования:
A.A. Zaharadniuk, K.G. Senkovsky, R.V. Lukashevich.
Correction of the Contribution of Scattered Photon Radiation to the Ionization Chamber Readings During X-Ray Radiation Quality Assessment.
Приборы и методы измерений.
2022. – Т. 13, № 3. – С. 180–188.
DOI: 10.21122/2220-9506-2022-13-3-180-188

For citation:
A.A. Zaharadniuk, K.G. Senkovsky, R.V. Lukashevich.
Correction of the Contribution of Scattered Photon Radiation to the Ionization Chamber Readings During X-Ray Radiation Quality Assessment.
Devices and Methods of Measurements.
2022, vol. 13, no. 3, pp. 180–188.
DOI: 10.21122/2220-9506-2022-13-3-180-188

Коррекция вклада рассеянного фотонного излучения в показания ионизационной камеры при оценке качества рентгеновского излучения

А.А. Загороднюк[1, 2], К.Г. Сеньковский[1], Р.В. Лукашевич[1]

[1]*УП «АТОМТЕХ»,*
ул. Гикало, 5, г. Минск 220005, Беларусь

[2]*Белорусский государственный университет,*
пр-т Независимости, 4, г. Минск 220030, Беларусь

Поступила 27.06.2022
Принята к печати 23.09.2022

Уменьшение систематической погрешности при определении характеристик эталонных полей рентгеновского излучения в соответствии со стандартом ISO 4037-1:2019 является актуальной задачей при установлении качеств излучения в дозиметрических лабораториях. Целью работы являлась разработка метода, позволяющего учесть вклад излучения, рассеянного на фильтре, при определении слоя половинного ослабления поля фотонного излучения, генерируемого рентгеновской установкой, а также уменьшить затраты на определение этого вклада.

Одним из основных факторов, который вносит систематическую погрешность при измерении слоя половинного ослабления, является излучение, рассеянное на материале фильтра. Стандарт рекомендует учёт этой погрешности при проведении измерений, однако не содержит методики, которая позволила бы это сделать.

В работе исследовалась возможность уменьшения вклада рассеянного излучения в отклик ионизационной камеры при оценке характеристик полей излучения рентгеновской установки с помощью измерения слоёв половинного ослабления для *N*-серии, *L*-серии и *H*-серии качеств рентгеновского излучения согласно стандарту ISO 4037-1:2019. Компенсация вклада рассеянного излучения в результаты измерений производилась путём применения корректирующих коэффициентов. Расчёт коэффициентов производился методом нулевой апертуры, реализованным в Монте-Карло программе FLUKA. Основным отличием метода, предложенного в данной работе, является выбор воздушной кермы в качестве расчётной величины отклика компьютерной модели ионизационной камеры на воздействие фотонного излучения. Корректность результатов, полученных в данной работе, проверялась сопоставлением расчётных значений слоёв половинного ослабления с табличными значениями, приведёнными в стандарте ISO 4037-1:2019. Отклонение расчётных значений от указанных в стандарте не превышает 2 %.

Установлено, что погрешность, вносимая рассеянным излучением в величину слоя половинного ослабления при прямых измерениях, не превышает 5 %. Использование воздушной кермы позволило существенно сократить время расчёта коэффициентов коррекции (относительно других методов, где в качестве отклика модели ионизационной камеры используется поглощённая энергия) в 6–16 раз в зависимости от серии качества излучения. Это позволило произвести расчёт поправочных коэффициентов для расстояния источник–детектор, равного 2,5 м.

Ключевые слова: Монте-Карло моделирование, рентгеновская установка, рассеянное излучение.

DOI: 10.21122/2220-9506-2022-13-3-180-188

Адрес для переписки:
Загороднюк А.А.
УП «АТОМТЕХ»,
ул. Гикало, 5, г. Минск 220005, Беларусь
e-mail: fiz.zagorodnAA@gmail.com

Address for correspondence:
Zaharadniuk A.A.
SPE "ATOMTEX",
Gikalo str., 5, Minsk 220005, Belarus
e-mail: fiz.zagorodnAA@gmail.com

Для цитирования:
A.A. Zaharadniuk, K.G. Senkovsky, R.V. Lukashevich.
Correction of the Contribution of Scattered Photon Radiation to the Ionization Chamber Readings During X-Ray Radiation Quality Assessment.
Приборы и методы измерений.
2022. – Т. 13, № 3. – С. 180–188.
DOI: 10.21122/2220-9506-2022-13-3-180-188

For citation:
A.A. Zaharadniuk, K.G. Senkovsky, R.V. Lukashevich.
Correction of the Contribution of Scattered Photon Radiation to the Ionization Chamber Readings During X-Ray Radiation Quality Assessment.
Devices and Methods of Measurements.
2022, vol. 13, no. 3, pp. 180–188.
DOI: 10.21122/2220-9506-2022-13-3-180-188

Introduction

One of the main, integral characteristics used to assess the quality of X-ray radiation with respect to its penetration ability is the half-value layer (*HVL*). This value represents the thickness of the attenuating material after which the initial intensity of X-ray radiation is reduced by a half. In addition to the first *HVL* (*HVL*1), the second *HVL* value (*HVL*2) gives the thickness of the attenuating material which decreases the initial photon radiation intensity by the total factor of 4. In other words, the initial X-ray intensity is reduced by 4 through the material's attenuating layer of thickness *HVL*1 + *HVL*2.

The estimation procedure for both *HVL*1 and *HVL*2 according to the ISO 4037-1:2019 [1] can be described as follows:

– an ionization chamber (IC) is placed at a chosen distance from the focal spot of the X-ray tube;

– an attenuation plate made of the specified material (or the filter for short) is placed between the IC and the X-ray tube's focal spot;

– the operator can obtain the dependence $I = f(h)$, where I is an IC response, and h is the filter's thickness, with the latter being varied, thus also obtaining the *HVL*1 and the *HVL*2 values from the resulting *I*-curve.

Such approach to estimation of *HVL* values has one minor flaw: the IC catches not only the radiation attenuated by the photon absorption in the filter but it also registers photons scattered by the latter. The amount of scattered photon radiation getting inside the IC depends on the size of the transverse photon field in the area where the filter is located; that causes over-estimation of the IC response. As a consequence, the *HVL*1 and *HVL*2 values obtained by this method are also overestimated. The standard ISO 4037-1:2019 emphases that this contribution should be mitigated for a tube with the potential greater than 100 kV by the means of extrapolation to infinitely small field size, also known as the zero-aperture approximation method. Although the ISO standard stresses the need for such extrapolation, it does not stipulate a method to perform that.

A set of correction factors would make the zero-aperture approximation method possible for a reduction of scattered radiation's effect on *HVL*1 and *HVL*2 estimation. Implementing this by direct, precise, empirical measurements is a rather cumbersome procedure which would be time-consuming and require a lot of iterations; therefore, replacement of direct measurements with Monte Carlo modeling has been proposed [2]. Although that approach greatly simplifies acquisition of the correction factors, it also requires either a significant computer capability or a long processing time.

This paper proposes an improved version of the method presented in [2]. Slight changes to the initial algorithm can significantly reduce the time required for the correction factors to be calculated; that, in turn, makes it possible to implement the method on conventional desktop computers.

The zero-aperture approximation method

The underlying assumption for this method postulates that the amount of scattered photon radiation to penetrate the IC depends on the transverse photon field size of the X-ray unit in the area of the filter, which, in turn, implies that there is no scattered radiation penetrating the IC in the case when the transverse photon field size approaches zero.

The algorithm proposed for calculating of correction factors with Monte Carlo modeling proceeds as follows:

– With the help of an appropriate simulation package, FLUKA in this case, the user creates a computer model which contains a source of the initial photon radiation, an IC, and a filter.

– The user determines the dependence $I = f(h)$ by varying the filter's thickness for a given transverse photon field size d (the transverse field size is estimated as the transverse diameter of the field at a given distance from the source). An IC response is tentatively defined at this point as a given quantity calculated by the Monte Carlo program; a more rigorous definition is given in the relevant section later in this paper.

– The user calculates *HVL*1 and *HVL*2 with the dependence $I = f(h)$ thus obtained.

– By matching thus obtained values of *HVL*1 and *HVL*2 with the transverse photon field size d, the user determines $h_{HVL1} = g(d_1)$ and $h_{HVL2} = g(d_2)$, where h_{HVL} is a *HVL* thickness for a given transverse photon field size d. When d approaches zero, the dependence $h_{HVL} = g(d)$ enables calculation of the *HVL* thickness when scattered radiation at $d = 0$ is absent.

– The correction factor can be calculated as the ratio of the *HVL* for a given field size to the *HVL* at $d = 0$: $\alpha_x = h_{HVL(d=0)} / h_{HVL(d=x)}$.

Monte Carlo modeling

We used the FLUKA software [3, 4] (ver. 4.0.1) as the environment for the Monte Carlo implementation of the zero-aperture approximation method. The model (Figure 1) consists of two conical regions separated by a cylindrical copper filter placed at 50 cm from the source. At 1 m and 2.5 m from the source, there are two cylindrical areas corresponding to the active volume of the IC. The overall shape of the model's geometry makes it possible to cut off radiation that cannot enter the active volume of the IC.

Figure 1 – Graphical representation of the Monte Carlo model for the *HVL* calculation. IC 1 m and IC 2.5 m correspond to the location of the active volume of the ionization chambers at a distance of 1 m and 2.5 m from the source (created by using FLAIR program [5])

The source is a flat disc 5 mm in diameter, which corresponds to the size of the actual focal spot of the X-ray machine. The photon radiation field has a conical shape with the source at its top. For a given transverse photon field size d, the program gradually increases the filter thickness and calculates the IC value. One iteration of the program, a set of calculations for a given field size, is divided into 50 steps. Each subsequent step increases the filter thickness from 0 mm to 5 times the *HVL* in mm (the initial value of the *HVL* is taken from the ISO 4037-1:2019). One iteration yields the dependence $I = f(h)$, which is then approximated by a cubic spline with packages NumPy and SciPy for Python (Figure 2). The program changes the field size d and repeats the sequence.

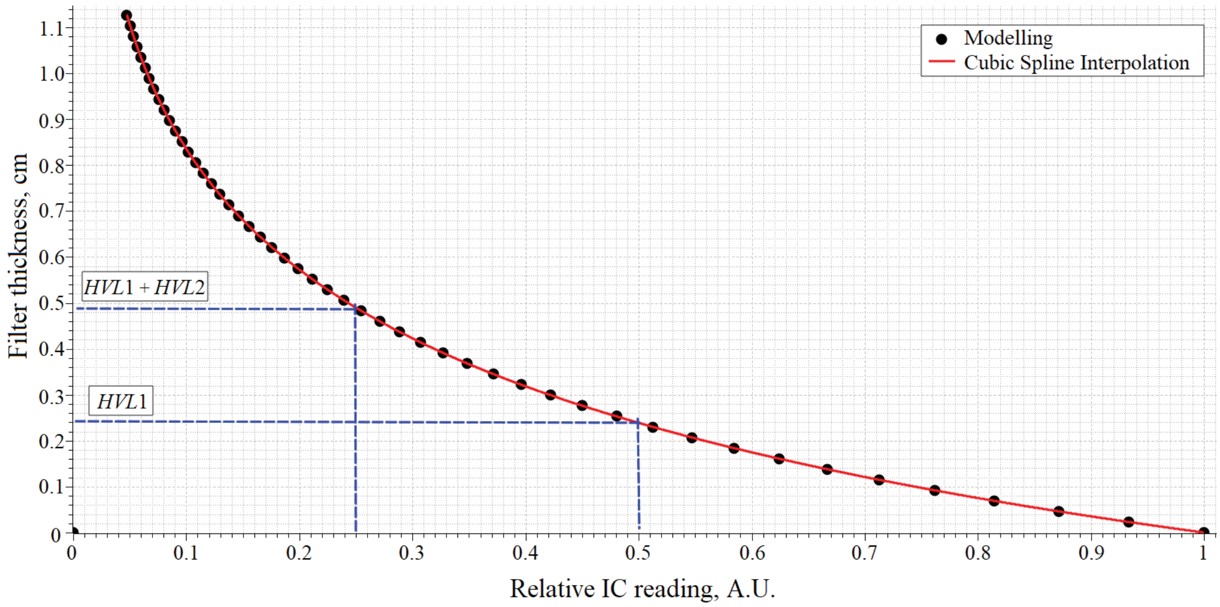

Figure 2 – The dependence of IC readings from filter thickness with cubic spline interpolation for one iteration. The case for the N150 radiation quality at the distance of 1 m from the source to the IC is shown. The transverse size of the field is 6 cm in diameter at the 50-cm distance from the source

Six iterations was performed for each radiation quality with the following set of transverse field diameters at the 50-cm distance from the source: 6 cm, 7 cm, 8 cm, 9 cm, 10 cm, 11 cm. The intermediate result of one iteration is the set of both *HVL*1 and *HVL*2 values for a given field size. Having completed all six iterations, the program draws the curve $h_{HVL} = g(d)$ for each *HVL*1 and *HVL*2. By making d approach zero, the program calculates $HVL(d = 0)$ and correction factors (Figure 3). The procedure was applied to the *N*-series, the *L*-series, and the *H*-series [6] according to ISO 4037-1:2019.

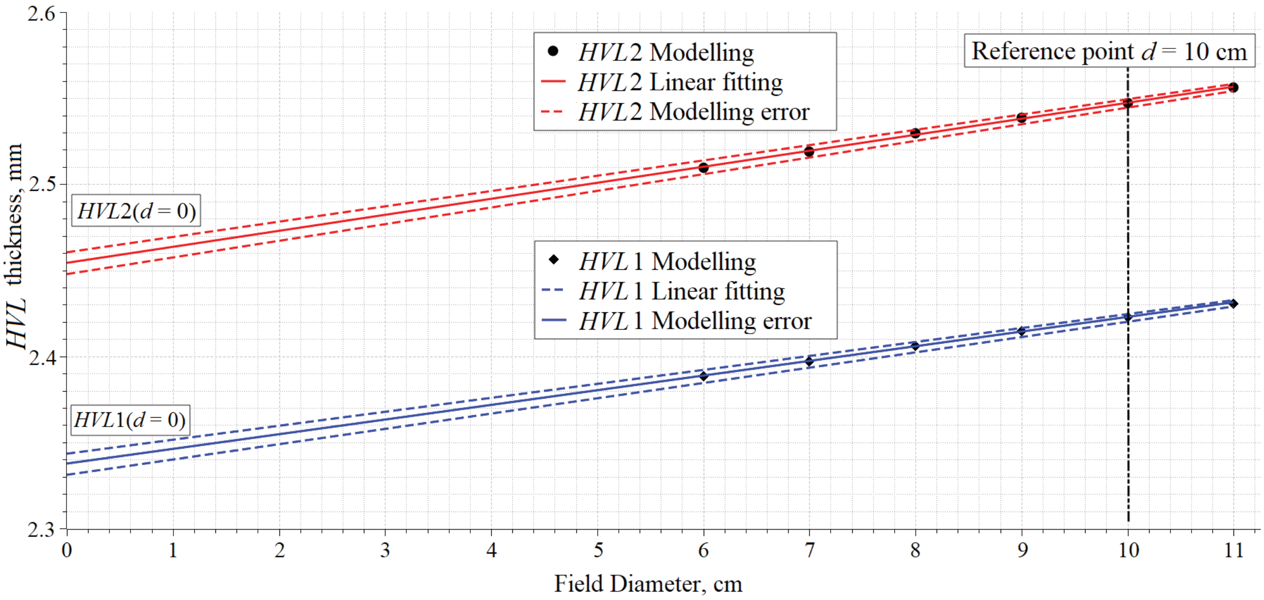

Figure 3 – The dependence of *HVL* thickness from transverse field diameter: in blue – calculation of *HVL*1, in red – calculation of *HVL*2. The figure shows the case for the N150 radiation quality. The distance between the source and the IC is 1 meter. The transverse dimension of the photon radiation field is 6 cm at a distance of 50 cm from the source

The main improvement which makes increasing the speed of the model's simulations and calculations by several times possible is the choice of the value for the IC response. The study in [2] has suggested previously to use energy deposited inside the active volume of the IC (the tally *F8 of the MCNP program [7]); however, interaction of photon radiation with air molecules is extremely rare due to the fact that air has a very low density (0.0012 g/cm^3 according to NIST). Therefore, to collect good statistics and reduce the calculation error, it is necessary for a Monte Carlo simulation to increase the number of primary particles *N*. This leads to a significant increase of the program's runtime because it linearly depends on the number of primary particles, i. e., $t \sim N$ [7], while calculation error has the dependence err $\sim 1/\sqrt{N}$.

Instead of using energy deposited inside the active volume, one can use air kerma as the IC response. That quantity has a simple relation with the photon fluence [8]:

$$K_{air} = \sum_i E_i \varphi_i \left(\frac{\mu_{en}}{\rho} \right)_i, \qquad (1)$$

where φ_i is photon fluence, 1/cm^2; $\left(\frac{\mu_{en}}{\rho} \right)_i$ is the mass energy-absorption coefficient, cm^2/g; E_i is the energy of photons, MeV.

The main advantage of using air kerma is the ability to use photon fluence instead of deposited energy when calculating an IC response. With respect to Monte Carlo modelling, the photon fluence is calculated as the ratio of the sum of particle tracks in a given region to the volume of this region. The calculation error does not depend on the number of interactions of photons with air inside the IC with this approach. The modelling discrepancy becomes inversely proportional to the number of photons crossing the given IC volume, which, in turn, makes it possible to reduce the number of simulated primary particles and, thus, the program's runtime.

Results and discussion

The correction factors calculation was carried out on a personal computer with the following configuration: two Intel Xeon Gold 6138 processors, the DDR4 SDRAM of 84 Gb, the SSD of 512 Gb. Modelling results have been validated by comparing the values for *HVL* at $d = 0$ produced by the program with tabulated values provided for *HVL* in ISO 4037-1:2019. Table 1 shows the results of *HVL* calculations at $d = 0$ using the IC response to deposited energy (HVL_{st}) [2] and to air kerma (HVL_{ak}).

Simulations were conducted for the source-IC distance at 1 m in both cases. The HVL_{st} calculations were performed for the number of initial particles at 6×10^9 for the *L*-series and at 16×10^9 for the *H*-series; the total modelling error for each quality did not exceed 2 %. For the HVL_{ak} calculations, the number of initial particles was 1×10^9 for both *L*-series and *H*-series with the total modelling error not exceeding 2 % again. This paper does not present the results of comparing HVL_{st} and HVL_{ak} for *N*-series due to anomalously large statistics required to obtain a satisfactory modelling error, i. e., a value equal to three standard deviations and expressed as a percentage of the calculated IC response.

Table 1

Comparison of *HVL*(*d* = 0) for radiation qualities in *L*-series and *H*-series (the source-IC distance is 1 m)

Quality	*HVL*1 ISO, mm	$HVL1_{st}$, mm	$HVL1_{ak}$, mm	*HVL*2 ISO, mm	$HVL2_{st}$, mm	$HVL2_{ak}$, mm
L70	0.483	0.479	0.483	0.505	0.507	0.504
L100	1.22	1.214	1.214	1.25	1.245	1.25
L125	1.98	1.992	2.012	2.02	2.076	2.049
L170	3.4	3.404	3.417	3.46	3.497	3.476
L210	4.52	4.576	4.530	4.55	4.533	4.571
L240	5.19	5.224	5.226	5.22	5.274	5.217
H80	0.176	0.177	0.178	0.268	0.268	0.270
H100	0.294	0.293	0.295	0.462	0.463	0.463
H150	0.808	0.801	0.811	1.21	1.203	1.220
H200	1.54	1.536	1.554	2.28	2.286	2.303
H250	2.42	2.448	2.441	3.24	3.276	3.279
H300	3.22	3.200	3.254	4.00	3.976	4.042

Table 2 shows the correction factors for the aforementioned quality series produced from both the IC response to deposited energy (HVL_{st}) [2] and to air kerma (HVL_{ak}). The factors were calculated for the transverse diameter of the photon field equal to 10 cm at the 50-cm distance from source.

Table 2

Comparison of correction factors for radiation qualities in *L*-series and *H*-series (the source-IC distance is 1 m; the reference transverse size of the field is 10 cm in diameter at the 50-cm distance from the source)

Quality	α_{st} (*HVL*1)	α_{ak} (*HVL*1)	discr, % (*HVL*1)	α_{st} (*HVL*2)	α_{ak} (*HVL*2)	discr, % (*HVL*2)
L70	0.988	0.984	0.407	0.992	0.984	0.813
L100	0.974	0.974	0.000	0.964	0.971	0.721
L125	0.957	0.967	1.034	0.985	0.965	2.073
L170	0.955	0.962	0.728	0.967	0.96	0.729
L210	0.972	0.962	1.039	0.955	0.961	0.624
L240	0.959	0.964	0.519	0.971	0.962	0.936
H80	0.989	0.989	0.000	0.989	0.989	0.000
H100	0.983	0.987	0.405	0.989	0.983	0.610
H150	0.974	0.978	0.409	0.96	0.970	1.031
H200	0.961	0.971	1.030	0.958	0.962	0.416
H250	0.969	0.966	0.311	0.962	0.963	0.104
H300	0.949	0.964	1.556	0.954	0.964	1.037

From data Table 1 it can be concluded in that both methods provide similar estimations for *HVL* values with respect to the ones tabulated in ISO 4037-1:2019 with the maximum deviation not exceeding 2 % and the average deviation not exceeding 1 %. For the correction factors in Table 2, it can be noted that the maximum contribution of scattered radiation to the IC response does not exceed 5 %. Using air kerma as the IC reading makes it possible to reduce the calculation time by the factor of 6 for *L*-series and by the factor of 16 for *H*-series. As an example, the total time necessary to calculate HVL_{st} values for *H*-series was approximately four months, while HVL_{ak} calculation took approximately one week. In both those cases, calculations were performed on the same aforementioned PC.

Table 3 gives the final calculation results of the HVL_{ak} and the α_{ak} quantities for the *H*, *L*, and *N* series. Both HVL_{ak} and α_{ak} were calculated for the source-IC distances of 1 m and of 2.5 m and for the transverse diameter of the photon field for α_{ak} being equal to 10 cm at the 50-cm distance from the source.

Table 3

$HVL(d = 0)$ and correction factors for air kerma as IC response for radiation qualities in *L*-series, *H*-series, and *N*-series (the reference transverse size of the field is 10 cm in diameter at the 50-cm distance from the source)

Quality	Source-IC distance is 1 m				Source-IC distance is 2.5 m			
	*HVL*1	*HVL*2	α_{HVL1}	α_{HVL2}	*HVL*1	*HVL*2	α_{HVL1}	α_{HVL2}
L70	0.483	0.504	0.984	0.984	0.483	0.506	0.991	0.993
L100	1.214	1.250	0.974	0.971	1.215	1.257	0.984	0.986
L125	2.012	2.049	0.967	0.965	2.013	2.050	0.979	0.977
L170	3.417	3.476	0.962	0.960	3.416	3.473	0.974	0.971
L210	4.530	4.571	0.962	0.961	4.515	4.576	0.970	0.975
L240	5.226	5.256	0.964	0.962	5.217	5.254	0.974	0.973
H80	0.178	0.270	0.989	0.989	0.181	0.273	0.994	0.996
H100	0.295	0.463	0.987	0.983	0.299	0.468	0.994	0.992
H150	0.811	1.220	0.978	0.970	0.816	1.226	0.989	0.981
H200	1.554	2.303	0.971	0.962	1.558	2.31	0.979	0.976
H250	2.441	3.279	0.966	0.963	2.449	3.272	0.978	0.970
H300	3.254	4.042	0.964	0.964	3.257	4.035	0.974	0.973
N100	1.093	1.153	0.975	0.975	1.096	1.157	0.986	0.987
N120	1.682	1.748	0.969	0.968	1.687	1.750	0.986	0.98
N150	2.337	2.454	0.965	0.963	2.340	2.455	0.983	0.976
N200	3.941	4.019	0.962	0.961	3.937	4.009	0.977	0.971
N250	5.129	5.190	0.964	0.963	5.121	5.185	0.973	0.973
N300	6.013	6.058	0.967	0.965	6.009	6.061	0.977	0.976

A direct comparison shows that both methods, either using the deposited energy or air kerma as the IC response, yield similar results with respect to both $HVL(d = 0)$ and the correction factors. The deviation of calculated *HVL* values from those specified in the standard does not exceed 2 %. However, using air kerma as the IC reading is preferable since this method makes the calculations much faster, down by 16 times for selected quality series. This time reduction for the correction factors is especially significant when the distance between the X-ray apparatus's focal spot and the IC is equal to 2.5 m.

The method proposed in this paper has several flaws, however. First of all, in order to use air kerma as the IC response according to formula (1), the mass-energy absorption coefficients must be obtained for every energy value in the photon spectrum. Those coefficients are stored in databases (the NIST database [9] was used for the results in this paper) as a set of tabulated values for a given set of energies. Such a database contains 41 mass-energy absorption coefficients for copper in the energy range between 1 keV and 20 MeV. A typical X-ray spectrum with maximum energy >100 keV contains more than 100 energy bins when properly measured by any modern spectrometer. The necessary mass absorption coefficients for formula (1) have to be obtained by interpolation; the first-order spline interpolation was used to generate those coefficients for the calculations described in this paper.

Secondly it has been discovered that program's output depends on the filter-splitting method. Different calculation results can be obtained for both *HVL* and correction factors by changing the maximum filter thickness and the number of steps. The project described in this paper attempted to optimize calculation results by varying the filter thickness. It was found that the maximum filter thickness of 5 *HVL*1 (according to the ISO4037-1:2019) split into 50 steps is a reasonable choice with respect to both the output discrepancy and the calculation time.

Finally the result produced by a simulation utilizing the presented method depends on the choice of the interpolation function for the dependence $I = f(h)$ (Figure 2). Interpolating with the sum of three decaying exponentials suggested in [2] seemed to be a good choice when the deposited energy was used as the IC response, but that interpolation technique has proved to be poor when using air kerma. The cubic spline interpolation was utilized for the air kerma calculations described in this paper. The choice of such an interpolation technique can very well be the reason for inflection points appearing in the resulting interpolated curve.

All these flaws can lead to discrepancies between the calculated and the ISO-tabulated *HVL* values regardless to the modelling error. This can also lead to discrepancies in the output results between the two methods, the one using deposited energy as the IC response and the presented one using air kerma, for the *HVL* and for correction factors.

It should be noted here that the contribution of scattered photon radiation to the IC response is always positive and leads to overestimation of *HVL* when directly measured. Considering this fact as well as the magnitude of the discrepancy caused by scattered photon radiation, it can be argued that the use of the correction factors obtained in this paper brings the result of direct *HVL* measurements closer to their experimental values.

Conclusion

The developed method allows taking into account the contribution of radiation scattered on the filter when determining the *HVL* of the photon radiation field generated by the X-ray unit. Its practical implementation was carried out in the FLUKA Monte Carlo program. The simulation showed that the contribution of the scattered radiation to the calculated *HVL* value does not exceed 5 % of its true meaning for X-ray radiation fields with the tube voltage under 300 kV.

It was found that the contribution of scattered radiation to the ionization chamber readings is a positive value. That in turn leads to overestimation of the *HVL* calculation result in direct measurements. This overestimation was mitigated by means of correction coefficients.

The main difference between the method proposed in this study and the analogues is the choice of the calculated value. The use of air kerma as a value of the model response to the influence of photon radiation made it possible to reduce the calculation time. In particular, the time spent on the calculation of the correction coefficients for the *H*-quality series was reduced by 16 times, for the *L*-quality series by 8 times, and for the *N*-quality series by 6 times (as compared to the standard method of calculation). This made it possible to calculate correction coefficients for the "source-detector" distance equal to 2.5 m (according to ISO4037-1:2019 requirements) for these quality series. Based on the analysis of similar scientific papers, we can assume that this result has never been published.

Due to its calculation speed the method proposed in this paper can be implemented on an ordinary workstation. This make it possible to extend its application to a wide range of users of X-ray equipment. Which in turn can contribute to a wider implementation of ISO 4037-1:2019.

References

1. ISO 4037-1:2019. Radiological protection-X and gamma reference radiation for calibrating dosemeters and doserate meters and for determining their response as a function of photon energy. Part 1: Radiation characteristics and production methods. Introd. 30.01.2019. International Organization for Standartization, 2019, 47 p.

2. Bandalo V., Greiter M.B., Brönner J., Hoedlmoser H. ISO 4037:2019 Validation of radiation qualities by means of half-value layer and Hp(10) dosimetry. *Radiation Protection Dosimetry*, 2019, no. 187, pp. 438–450.
DOI: 10.1093/rpd/ncz185

3. Battistoni G., Boehlen T., Cerutti F., Chin P.W., Esposito L.S., Fassò A., Ferrari A., Lechner A., Empl A., Mairani A., Mereghetti A., Garcia Ortega P., Ranft J., Roesler S., Sala P.R., Vlachoudis V., Smirnov G. Overview of the FLUKA code. *Annals of Nuclear Energy*, 2015, no. 82, pp. 10–18.
DOI: 10.1016/j.anucene.2014.11.007

4. Bohlen T.T., Cerutti F., Chin M.P.W., Fassò A., Ferrari A., Ortega P.G., Mairani A., Sala P.R., Smirnov G., Vlachoudis V. The FLUKA Code: Developments and Challenges for High Energy and Medical Applications. *Nuclear Data Sheets*, 2014, no. 120, pp. 211–214.
DOI: 10.1016/j.nds.2014.07.049

5. Vlachoudis V. FLAIR: A Powerful But User Friendly Graphical Interface For FLUKA. International Conference on Mathematics, Computational Methods and Reactor Physics, New York, 2009, pp. 2–11.

6. Ankerhold U. Catalogue of X-ray spectra and their characteristic data – ISO and DIN radiation qualities, therapy and diagnostic radiation qualities, unfiltered X-ray spectra. PTB, Braunschweig (Germany), 2000.

7. Briesmeister J.F. MCNP-A general monte Carlo N-particle Transport Code (Version 4C). [Electronic Resource]. Los Alamos National Laboratory, 2000. Available at: http://permalink.lanl.gov/object/tr?what=info:lanl-repo/lareport/LA-13709-M (accessed: 10 June 2022).

8. Attix H. Introduction to radiological physics and radiation dosimetry. Wiley, New York, 1986.

9. Hubbell J., Seltzer S. Tables of X-Ray Mass Attenuation Coefficients and Mass Energy-Absorption Coefficients 1 keV to 20 MeV for Elements Z = 1 to 92 and 48 Additional Substances of Dosimetric Interest. Maryland, USA, 1995. [Electronic Resource]. Available at: http://physics.nist.gov/PhysRefData/XrayMassCoef/cover.html (accessed: 10 June 2022).

Devices and Methods of Measurements
2022, vol. 13, no. 3, pp. 189–198
S.G. Sandomirski et al.

Calculation of Correction Factors for Vickers' Hardness Measurements on a Non-Planar Surface

Sergei G. Sandomirski, Aleksandr L. Val'ko, Sergej P. Rudenko

Joint Institute of Mechanical Engineering of the National Academy of Sciences of Belarus, Akademicheskaya str., 12, Minsk 220072, Belarus

Received 11.05.2022
Accepted for publication 21.07.2022

Abstract

The exact determination of Vickers HV hardness is important for determining of the product material mechanical properties. An important aspect of measuring HV is to obtain its values on a non-planar surface. Regulatory documents contain table values of correction factors K which depend on the surface shape (convex or concave, spherical or cylindrical), its curvature (diameter D) and hardness (arithmetic mean d of indentation diagonal lengths) but this does not solved the problem. The K values for d/D ratios not given in the tables are determined by interpolation from the closest to the measured tabulated d/D values. The error in the representation of these tabulated d/D values is fully included in the error of determining the K coefficient for the measured d/D ratio. The aim of the work was to simplify the calculation of correction factors K for Vickers hardness measurements on non-planar surfaces and to reduce the calculation error compared to the methodology governed by the regulations.

The method presented is based on a statistical analysis of K coefficients, presented in regulatory documents for cases considered in the form of tables. The sufficiency of using of a quadratic power function for approximating $K(d/D)$ dependences and the necessity of fulfilling the physically justified condition $K \equiv 1$ at zero curvature of tested surface have been substantiated. Simplification of calculation of K coefficient and decrease of calculation error in comparison with the recommended in the regulatory documents obtaining of K value by linear interpolation relative to two adjacent table values are shown.

The reduction of the calculation error in comparison with the calculation recommended in the regulatory documents occurred because of the reason that when calculating by the developed formulas, the error in the value of the calculated for a specific value of d/D coefficient K is averaged over all n values of d/D given in the table of GOST for a given surface. That is, the error is reduced by a factor of about $\sqrt{n/2}$ in comparison with the calculation according to the regulated procedure. This is illustrated by the above numerical data and an example of the use of the method.

The obtained formulas for calculation of correction coefficients K when measuring hardness HV on spherical and cylindrical (concave and convex) surfaces are reasonable to use for automatic calculation of HV on items with a non-planar surface.

Keywords: hardness measurements, Vickers method, concave and convex surfaces, correction factors.

DOI: 10.21122/2220-9506-2022-13-3-189-198

Адрес для переписки:
Сандомирский С.Г.
Объединенный институт машиностроения
Национальной академии наук Беларуси,
ул. Академическая, 12, г. Минск 220072, Беларусь
e-mail: sand_work@mail.ru

Address for correspondence:
Sandomirski S.G.
Joint Institute of Mechanical Engineering of the National Academy of Sciences of Belarus,
Akademicheskaya str., 12, Minsk 220072, Belarus
e-mail: sand_work@mail.ru

Для цитирования:
Sergei G. Sandomirski, Aleksandr L. Val'ko, Sergej P. Rudenko.
Calculation of Correction Factors for Vickers' Hardness Measurements on a Non-Planar Surface.
Приборы и методы измерений.
2022. – Т. 13, № 3. – С. 189–198.
DOI: 10.21122/2220-9506-2022-13-3-189-198

For citation:
Sergei G. Sandomirski, Aleksandr L. Val'ko, Sergej P. Rudenko.
Calculation of Correction Factors for Vickers' Hardness Measurements on a Non-Planar Surface.
Devices and Methods of Measurements.
2022, vol. 13, no. 3, pp. 189–198.
DOI: 10.21122/2220-9506-2022-13-3-189-198

Devices and Methods of Measurements
2022, vol. 13, no. 3, pp. 189–198
S.G. Sandomirski et al.

Расчёт поправочных коэффициентов при измерении твёрдости по Виккерсу на неплоской поверхности

С.Г. Сандомирский, А.Л. Валько, С.П. Руденко

*Объединенный институт машиностроения Национальной академии наук Беларуси,
ул. Академическая, 12, г. Минск 220072, Беларусь*

Поступила 11.05.2022
Принята к печати 21.07.2022

Точное определение твёрдости HV по Виккерсу важно для определения механических свойств материала изделий. Важным аспектом измерения HV является получение её значений на неплоской поверхности. Включение в нормативные документы табличных значений поправочных коэффициентов *K*, зависящих от формы (выпуклая или вогнутая, сферическая или цилиндрическая) поверхности, её кривизны (диаметра *D*) и твёрдости (среднего арифметического *d* длин диагоналей отпечатка) не решает проблему. Значения *K* для отношений *d*/*D*, не приведённых в таблицах, определяют интерполяцией от ближайших к измеренному табличных значений *d*/*D*. Погрешность представления этих табличных значений *d*/*D* полностью включается в погрешность определения искомого коэффициента *K* для измеренного отношения *d*/*D*. Цель работы – упрощение расчёта поправочных коэффициентов *K* при измерении твёрдости по Виккерсу на неплоских поверхностях и снижение погрешности расчёта по сравнению с методикой, регламентированной нормативными документами.

Разработка основана на статистическом анализе коэффициентов *K*, представленных в нормативных документах для рассмотренных случаев в виде таблиц. Обоснована достаточность использования квадратичной степенной функции для аппроксимации зависимостей *K*(*d*/*D*) и необходимость выполнения физически обоснованного условия $K \equiv 1$ при нулевой кривизне испытуемой поверхности. Показано упрощение расчёта коэффициента *K* и снижение погрешности расчёта по сравнению с рекомендованным в нормативных документах получением значения *K* линейной интерполяцией относительно двух соседних табличных значений.

Снижение погрешности расчёта по сравнению с расчётом, рекомендованным в нормативных документах, происходит за счёт того, что при расчёте по разработанным формулам погрешность в значении рассчитанного для конкретного значения *d*/*D* коэффициента *K* усредняется по всем *n* значениям *d*/*D*, приведённым в таблице ГОСТа для данной поверхности. То есть снижается примерно в $\sqrt{n/2}$ раз по сравнению с расчётом по регламентированной методике. Это иллюстрируют приведённые численные данные и пример использования методики.

Полученные формулы для расчёта поправочных коэффициентов *K* при измерении твёрдости HV на сферических и цилиндрических (вогнутых и выпуклых) поверхностях целесообразно использовать для автоматического расчёта HV на изделиях с неплоской поверхностью.

Ключевые слова: измерения твёрдости, метод Виккерса, вогнутые и выпуклые поверхности, поправочные коэффициенты.

DOI: 10.21122/2220-9506-2022-13-3-189-198

Адрес для переписки:
Сандомирский С.Г.
Объединенный институт машиностроения
Национальной академии наук Беларуси,
ул. Академическая, 12, г. Минск 220072, Беларусь
e-mail: sand_work@mail.ru

Address for correspondence:
Sandomirski S.G.
Joint Institute of Mechanical Engineering of the National Academy of Sciences of Belarus,
Akademicheskaya str., 12, Minsk 220072, Belarus
e-mail: sand_work@mail.ru

Для цитирования:
Sergei G. Sandomirski, Aleksandr L. Val'ko, Sergej P. Rudenko.
Calculation of Correction Factors for Vickers' Hardness Measurements on a Non-Planar Surface.
Приборы и методы измерений.
2022. – Т. 13, № 3. – С. 189–198.
DOI: 10.21122/2220-9506-2022-13-3-189-198

For citation:
Sergei G. Sandomirski, Aleksandr L. Val'ko, Sergej P. Rudenko.
Calculation of Correction Factors for Vickers' Hardness Measurements on a Non-Planar Surface.
Devices and Methods of Measurements.
2022, vol. 13, no. 3, pp. 189–198.
DOI: 10.21122/2220-9506-2022-13-3-189-198

Introduction

Hardness measurement is one of the main methods for assessing of strength characteristics of metals [1–3]. An indentor of a specified shape is pressed into the surface under test with a specified load for a specified time. After the load is removed from the indentor, an indentation remains on the surface and the area of the indentation is determined. The ratio of the indenting load to the area of the indentation is the hardness value. Because of their speed and ease of measurement, hardness values are widely used in metallurgical examinations.

The hardness of small thickness parts and surface layers is determined by Vickers (HV) [4, 5] – by pressing a four-sided diamond pyramid into the ground metal surface and determining the hardness HV by the formula:

$$\mathrm{HV} = \frac{2P\sin(\alpha/2)}{d^2} \approx 1.854\frac{P}{d^2}, \qquad (1)$$

where P is load on the pyramid; $\alpha = 136^{\circ}$ is angle between opposite sides of the pyramid at the top; d, mm is arithmetic mean of the lengths of the print diagonals measured after the load is removed (the difference of the print diagonals should not exceed 2 % of the smaller of them).

In accordance with [5], depending on the applied load P, the following terms are used:

– for a load of 49.03 N or higher is the term "Vickers hardness" and the range of hardness scales is designated "HV ≥ 5";

– 1.961 to 49.03 N is the term "low load hardness"; the hardness scales is labeled "0.2 ≤ HV < 5";

– for loads between 0.09807 and 1.961 N is the term "microhardness" and the range of hardness scales denote "0.01 ≤ HV < 0.2".

These criteria are formal and have no physical substantiation [6].

The method of microhardness or hardness with small load is the only method that allows to determine the hardness of phases and structural components of multicomponent alloys. It is established that in the range of microhardness there is an "Indentation Size Effect" [7]. It manifests itself in the fact that hardness values determined after removing the indenter from the test specimen, the higher the lower the load. Attempts to establish an analytical dependence of microhardness on load and to relate micro- and macrohardness have not been successful. It was shown in [8] that the dimensional effect is related to the fact that the elastic deformation of the material, which develops during indenter penetration and disappears after its removal, is not taken into account in hardness estimation. In contrast, in the macrohardness range, hardness values are load-independent due to the small fraction of elastic deformation.

The importance of accurate determination of HV hardness by Vickers is also due to the fact that its use ("in some particular cases" [4]) is recommended in determining the mechanical properties of the product material [6, 9, 10] and their distribution in the product [11].

Another important aspect of measuring the Vickers HV hardness is to obtain its values on a non-planar surface of products. This problem has been solved by including in normative documents [4, 5] correction factors K depending on the shape (convex or concave, spherical or cylindrical) of the surface, its curvature (diameter D) and hardness (arithmetic mean d of the indentation diagonals). In [4, 5] the values of K-factors are given in tabular form (the data [4] and [5] coincide, except for a misprint in [4] in the value $d/D = 0.079$ for the spherical convex surfaces). The K coefficient values given in [4, 5] from the value of 0.995 or 1.005 with a discreteness of 0.005 correspond to the values (accurate to the third decimal place) of the ratio d/D. The K values corresponding to the d/D ratio ratios not given in the d/D ratio tables in [5, Appendix B] propose to determine (examples are given for spherical and cylindrical surfaces) by "interpolation" of the K coefficient values given in the corresponding tables for the d/D ratio values closest to the measured one.

The regulated in [5] method of determining the correction coefficients K, taking into account the shape and curvature of the non-planar surface of the measured product, is not convenient to use and is not accurate enough. According to it, to determine the value of correction coefficient K for the ratio d/D obtained as a result of measurement, the closest tabular values of d/D ratio are used, the accuracy of representation of which is limited to the third decimal place after the decimal point. The error in represen-ting these "closest" d/D ratio values is completely included in the error in determining the desired correction factor K for the measured d/D ratio. This reduces the achievable accuracy of the Vickers HV hardness measurement method for products with curved surfaces, including the hardness of thin films applied to them [12].

The aim of the work was to simplify the calculation of correction factors K for Vickers hardness measurements on non-planar surfaces and to reduce the calculation error compared to the methodology governed by the regulations.

Development of the required analytical expressions

Let us use the data on the relationships between the values of the correction factor K and the values of the ratio d/D for surfaces of different shapes and curvatures given in [5, Tables B.1–B.6]. These data are grouped in Tables 1–3.

Table 1

Correction factors *K* for spherical surfaces

Convex surfaces			Concave surfaces		
d/D	Correction factor K		d/D	Correction factor K	
	According to [5]	Calculation of the (2)		According to [5]	Calculation of the (3)
0.004	0.995	0.99395	0.004	1.005	1.00454
0.009	0.990	0.99039	0.008	1.010	1.00924
0.013	0.985	0.98621	0.012	1.015	1.01410
0.018	0.980	0.98107	0.016	1.020	1.01913
0.023	0.975	0.97601	0.020	1.025	1.02431
0.028	0.970	0.97104	0.024	1.030	1.02967
0.033	0.965	0.96617	0.028	1.035	1.03518
0.038	0.960	0.96138	0.031	1.040	1.03942
0.043	0.955	0.95667	0.035	1.045	1.04522
0.049	0.950	0.95115	0.038	1.050	1.04968
0.055	0.945	0.94575	0.041	1.055	1.05423
0.061	0.940	0.94049	0.045	1.060	1.06044
0.067	0.935	0.93534	0.048	1.065	1.06520
0.073	0.930	0.93033	0.051	1.070	1.07006
0.079	0.925	0.92544	0.054	1.075	1.07500
0.086	0.920	0.91991	0.057	1.080	1.08004
0.093	0.915	0.91454	0.060	1.085	1.08517
0.100	0.910	0.90935	0.063	1.090	1.09039
0.107	0.905	0.90433	0.066	1.095	1.09571
0.114	0.900	0.89949	0.069	1.100	1.10111
0.122	0.895	0.89416	0.071	1.105	1.10477
0.130	0.890	0.88907	0.074	1.110	1.11032
0.139	0.885	0.88361	0.077	1.115	1.11597
0.147	0.880	0.87899	0.079	1.120	1.11979
0.156	0.875	0.87407	0.082	1.125	1.12559
0.165	0.870	0.86944	0.084	1.130	1.12951
0.175	0.865	0.86463	0.087	1.135	1.13547
0.185	0.860	0.86017	0.089	1.140	1.13949
0.195	0.855	0.85607	0.091	1.145	1.14355
0.206	0.850	0.85197	0.094	1.150	1.14972

Table 2

Correction factors *K* for concave cylindrical surfaces

Correction factor *K* according to [5]	The diagonals are rotated 45º about the axis		One of the diagonals is parallel to the axis	
	d/*D* according to [5]	Calculation *K* of the (4)	*d*/*D* according to [5]	Calculation *K* of the (5)
1.005	0.009	1.00522	0.008	1.00365
1.010	0.017	1.00992	0.016	1.00808
1.015	0.025	1.01468	0.023	1.01261
1.020	0.034	1.02009	0.030	1.01774
1.025	0.042	1.02497	0.036	1.02262
1.030	0.050	1.02991	0.042	1.02794
1.035	0.058	1.03490	0.048	1.03371
1.040	0.066	1.03995	0.053	1.03885
1.045	0.074	1.04505	0.058	1.04430
1.050	0.082	1.05021	0.063	1.05006
1.055	0.089	1.05478	0.067	1.05489
1.060	0.097	1.06005	0.071	1.05991
1.065	0.104	1.06470	0.076	1.06647
1.070	0.112	1.07008	0.079	1.07056
1.075	0.119	1.07483	0.083	1.07617
1.080	0.127	1.08031	0.087	1.08199
1.085	0.134	1.08515	0.090	1.08648
1.090	0.141	1.09004	0.093	1.09108
1.095	0.148	1.09497	0.097	1.09738
1.100	0.155	1.09995	0.100	1.10224
1.105	0.162	1.10496	0.103	1.10721
1.110	0.169	1.11003	0.105	1.11059
1.115	0.176	1.11513	0.108	1.11574
1.120	0.183	1.12028	0.111	1.12101
1.125	0.189	1.12473	0.113	1.12458
1.130	0.196	1.12996	0.116	1.13003
1.135	0.203	1.13523	0.118	1.13372
1.140	0.209	1.13978	0.120	1.13747
1.145	0.216	1.14514	0.123	1.14318
1.150	0.222	1.14976	0.125	1.14705

Table 3

Correction factors *K* for convex cylindrical surfaces

Correction factor *K* according to [5]	The diagonals are rotated 45º about the axis		One of the diagonals is parallel to the axis	
	d/*D* according to [5]	Calculation *K* of the (6)	*d*/*D* according to [5]	Calculation *K* of the (7)
0.995	0.009	0.99481	0.009	0.9956
0.990	0.017	0.99024	0.019	0.99091
0.985	0.026	0.98513	0.029	0.98644
0.980	0.035	0.98007	0.041	0.98135
0.975	0.044	0.97506	0.054	0.97618
0.970	0.053	0.97009	0.068	0.97101
0.965	0.062	0.96516	0.085	0.96529
0.960	0.071	0.96027	0.104	0.95963
0.955	0.081	0.95490	0.126	0.95403
0.950	**0.090**	**0.95010**	0.153	0.94855
0.945	**0.100**	**0.94483**	0.189	0.94366
0.940	**0.109**	**0.94013**	0.243	0.94147
0.935	0.119	0.93496		
0.930	0.129	0.92985		
0.925	0.139	0.92478		
0.920	0.149	0.91978		
0.915	0.159	0.91482		
0.910	0.169	0.90993		
0.905	**0.179**	**0.90508**		
0.900	**0.189**	**0.90029**		
0.895	**0.200**	**0.89508**		

Correlation fields between the values of correction factors *K* and ratios *d*/*D* for surfaces of different shapes and curvatures are shown in Figures 1–3. The "Microsoft Excel" program and numerical values of *K* and *d*/*D* given in Tables 1–3 respectively were used for their construction. Statistical processing of correlation dependencies between *K* and *d*/*D* shown in Figures 1–3, construction of trend lines (polynomials of the second degree) of these dependencies and calculation of reliability of approximation R^2 (square of *R* correlation coefficient) was performed in the "Microsoft Excel" program. It should be noted that trend lines, equations of which are shown in Figures 1–3, are forcibly (programmatically) drawn through physically correct value of $K \equiv 1$ at zero curvature of tested surface (at $d/D = 0$).

Analysis of the results obtained

The following equations for determining the correction factors *K* for HV Vickers hardness measurements from the results of *d*/*D* ratios in the cases considered (sequentially for the dependencies shown in Figures 1*a*, 1*b*, 2*a*, 2*b*, 3*a*, 3*b*) were obtained:

$$K = 1.7729(l/D)^2 - 1.0838(l/D) + 1; \quad (2)$$

$$K = 5.0954(l/D)^2 + 1.1138(l/D) + 1; \quad (3)$$

$$K = 0.4446(l/D)^2 + 0.5759(l/D) + 1; \quad (4)$$

$$K = 6.1573(l/D)^2 + 0.4067(l/D) + 1; \quad (5)$$

$$K = 0.2711(l/D)^2 - 0.5788(l/D) + 1; \quad (6)$$

$$K = 1.0598(l/D)^2 - 0.4984(l/D) + 1. \quad (7)$$

The results of calculating the K coefficients according to the developed formulas (2)–(7) for the d/D values given in Tables 1–3 are given in these tables for the considered cases of the surface shape.

Information on the equations for calculating the correction coefficients K for HV Vickers hardness measurements on a non-planar surface in the cases considered are summarized in Table 4. The results of their statistical processing are also presented there: the reliability of R^2 approximation and the average values δ of the relative deviation module between the results of K_i coefficient K calculation by the developed formulas (2)–(7) and their tabulated (according to [5]) K_i(tabl) values for the curved surfaces under consideration.

The values of δ are calculated by the formula:

$$\delta = \frac{100\%}{n} \sum_{i=1}^{n} \frac{|K_i - K_i(\text{tabl})|}{K_i(\text{tabl})}, \quad (8)$$

where n is the number of values of the coefficient K in the corresponding columns of Tables 1–3.

Table 4

Information on equations for calculating *K*-correction factors for HV Vickers hardness measurements on a non-planar surface

Surface form	Indenter location	Table No, Figure No	Calculation formula	R^2	δ, %
Spherical, convex	Randomly	Table 1, Figure 1*a*	(2)	0.9995	0.0907
Spherical, concave		Table 1, Figure 1*b*	(3)	0.9998	0.0456
Cylindrical, convex	The diagonals are rotated 45° about the axis	Table 3, Figure 3*a*	(4)	1.0000	0.0153
Cylindrical, concave		Table 2, Figure 2*a*	(5)	1.0000	0.0132
Cylindrical, convex	One of the diagonals is parallel to the axis	Table 3, Figure 3*b*	(6)	0.9959	0.1069
Cylindrical, concave		Table 2, Figure 2*b*	(7)	0.9986	0.1293

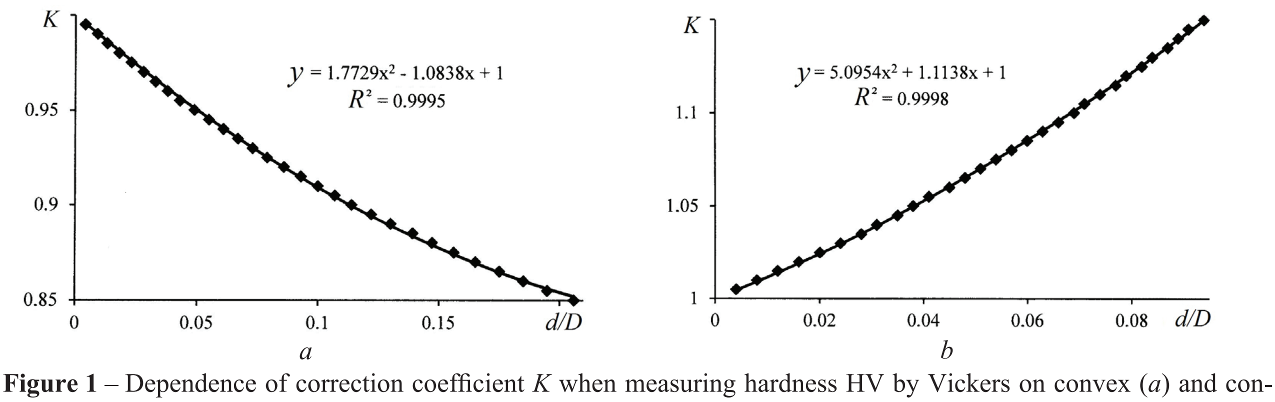

Figure 1 – Dependence of correction coefficient K when measuring hardness HV by Vickers on convex (*a*) and concave (*b*) spherical surfaces on the ratio d/D of arithmetic mean d of indentation diagonal lengths to surface diameter D. Table data (points) according to Table 1 (Table B.1 (*a*) and Table B.2 (*b*) in [5]), their interpolating power trend line passing through the value $K = 1$ at $d/D = 0$, its equation and reliability of R^2 approximation

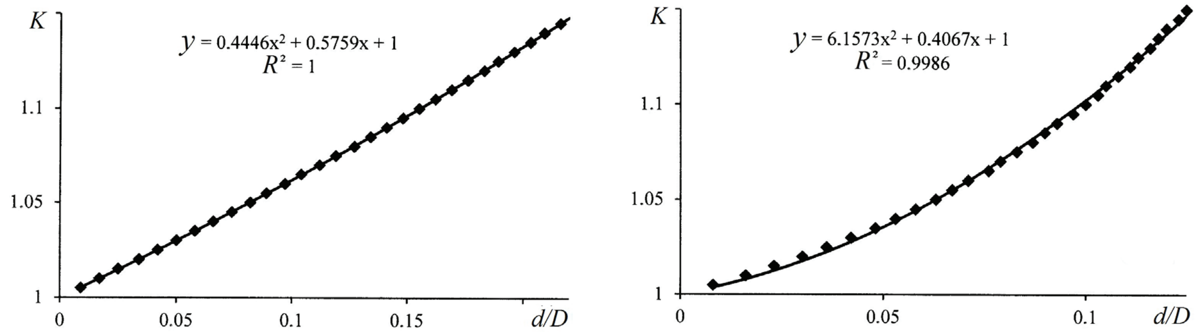

a *b*

Figure 2 – Dependence of the correction factor K when measuring HV hardness according to Vickers on a concave cylindrical surface when one of the diagonals of the indentation is oriented at an angle of 45º (*a*) and parallel (*b*) to the cylinder axis on the ratio *d*/*D*. Table data (points) according to Table 2 (Table B.4 (*a*) and Table B.6 (*b*) in [5]), their interpolating power trend line passing through the value $K = 1$ at $d/D = 0$, its equation and reliability of R^2 approximation

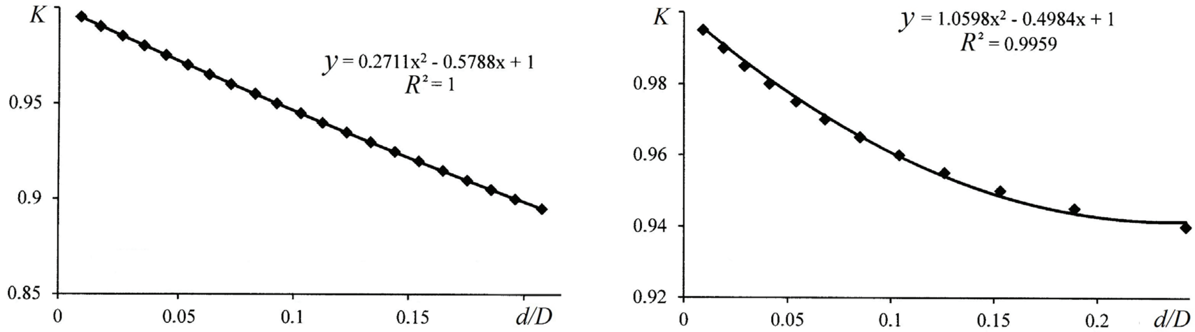

a *b*

Figure 3 – Dependence of the correction factor K when measuring HV hardness on a convex cylindrical surface with one of the indentation diagonals oriented at an angle of 45º (*a*) and parallel (*b*) to the cylinder axis on the ratio *d*/*D*. Table data (points) according to Table 3 (Table B.3 (*a*) and Table B.5 (*b*) in [5]), their interpolating power trend line passing through the value $K = 1$ at $d/D = 0$, its equation and reliability of R^2 approximation

The analysis of the results of statistical proces-sing of calculations of correction coefficients K when measuring HV hardness by Vickers on a non-planar surface presented in Table 4 showed that the quadratic power functions (2)–(7) provide close to "1" reliability of approximation of the tabulated data [5] about the value K and not significant numerical deviations in their calculations. These deviations do not exceed the units of the lowest digit of the tabulated data [5] (see Tables 1–3) and are more accurate than the tabulated data, because they have less discreteness and better monotonicity (it is clearly seen, for example, for *d*/*D* values, highlighted in Table 3 in bold type) of $K(d/D)$ dependences. In this connection, approximation of the experimental data by polynomials of higher powers or by functions of another kind does not make sense.

The calculation error is reduced in comparison with the calculation recommended in the normative documents due to the fact that the K coefficient value calculated according to the standard method includes the errors of the K coefficient representation for two neighboring points of surface curvature in Tables [5] due to the discreteness of their representation. When calculating by the developed formulas (2)–(7), the error in the value of the K coefficient calculated for a particular value of surface curvature is averaged over all n values given in the tables [5] for this type of surface. That is, the error is reduced by a factor of about $\sqrt{n/2}$ as compared with the calculation by the method [5]. This increases the accuracy of the Vickers HV hardness measurement method for products with curved surfaces. This is illustrated by the numerical data in Tables 1–3 and the following example of using the method of calculating correction factors.

The application of the formulas (2)–(7) to calculate the correction factors K in measuring the Vickers HV hardness on a non-planar surface is illustrated by their definition for a convex cylindrical surface of a wire 0.5 mm in diameter, on which a hardening coating is applied. Suppose the HV Vickers hardness measurements [5] on two parts of the wire yielded average values of diagonals (diagonals are turned 45° relative to the wire axis) of 0.0535 mm and 0.0585 mm, which correspond to d/D values of 0.107 and 0.117 respectively. By formula (6) we easily determine the values of correction factors K: they are equal to 0.94117 and 0.93599 accordingly. In determining the correction factors K by the standard procedure it would have been necessary to use the values 0.100 and 0.109; 0.109 and 0.119, the corresponding values of the correction factors 0.945 and 0.940; 0.940 and 0.935 (Table 3), to make the corresponding interpolations, and to determine the unknown values of K. The calculation result would have included the errors due to the discrepancy between the tabulated d/D and K values.

Thus, when determining the value of the correction factor K for the measured d/D ratio, which does not coincide with the tabulated values, the calculation according to the developed formulas provided a result more simple and accurate than the methodology regulated in [5].

Conclusion

Statistical analysis of correction coefficients K in measuring HV hardness according to Vickers on spherical and cylindrical (concave and convex) surfaces presented in normative documents in the form of tables has given analytical expressions for calculating K in all analyzed cases. The sufficiency of use of the quadratic power function for approximation of the obtained dependences and the necessity of fulfilling the physically justified condition $K \equiv 1$ at zero curvature of the tested surface have been substantiated. The simplification is shown and the decrease in the error of calculating the K coefficients according to the developed formulas is substantiated in comparison with the obtained K value by interpolation with respect to two neighboring table values recommended in the normative documents. It is reasonable to use the obtained expressions for automatic calculation of HV hardness according to Vickers on articles with a non-planar surface.

References

1. Agamirov L.V. *Mashinostroenie. Enciklopediya* [Engineering. Encyclopedia]. *V 40 t. Razd. 2. Materialy v mashinostroenii* [Materials in mechanical engineering]. *T. 2–1. Fiziko-mekhanicheskie svojstva. Ispytaniya metallicheskih materialov* [Physical-mechanical properties. Tests of metallic materials]. Moscow: Mashinostroenie Publ., 2010.

2. *Metallovedenie i termicheskaya obrabotka stali: spravochnik. V 3 t.* Ed. M.L. Bershtejna, A.G. Rahshtadta. *4 izdanie, pererabotannoe i dopolnennoe* [Metallurgy and Heat Treatment of Steel: Handbook]. Moscow: Metallurgiya Publ., 1991. – Vol. 1. *Metody ispytanij i issledovaniya* [Test and research methods]: v 2 knigah.

3. Mal'kov O.V., Litvinenko A.V. *Izmerenie tverdosti metallov. Elektronnoe uchebnoe izdanie* [Measuring the hardness of metals. Electronic textbok]. Moscow: MGTU imeni Baumana, 2011.

4. GOST 2999–75. Metally i splavy. Metod izmereniya tverdosti po Vikkersu [Metals and alloys. Vickers hardness test by diamond pyramid]. 01.07.76. Izmenennaya redakciya, Izmeneniya № 1, 2. Moscow: Izdatel'stvo standartov, 1987.

5. ISO 6507-1:2005. Metallic materials – Vickers hardness test – Part 1: Test method (IDT).

6. Golovin YU.I. *Nanoindengirovanie kak sredstvo kompleksnoj ocenki fiziko-mekhanicheskih svojstv materialov v submikroob"emah* [Nanoindentation as a tool for comprehensive assessment of physical and mechanical properties of materials in submicro-volumes]. *Zavodskaya laboratoriya. Diagnostika materialov* [Factory laboratory. Diagnostics of materials], 2009, vol. 75, no. 1, pp. 45–58.

7. Gerberich W.W., Tymiak N.I., Grunlan J.C., Horste-Meyer M.F., Baskes M.I. Interpretations of Indentation Size Effects. *Journal of Applied Mechanics*, 2002, vol. 69, pp. 433–442.

8. Adaskin A.M., Sapronov I.YU. *Opredelenie sootnosheniya uprugoj i plasticheskoj sostavlyayushchej raboty deformirovaniya v diapazone mikrotverdosti pri indentirovanii po velichinam vosstanovlennogo i nevosstanovlennogo otpechatkov* [Determination of the ratio between the elastic and the plastic component of the work of deformation in the microhardness range during indentation by the values of the restored and unrestored imprints]. *Materialy VII Mezhdunarodnoj konferencii "Deformaciya i razrushenie materialov i nanomaterialov"* [Deformation and Fracture of Materials and Nanomaterials]. Moscow: IMET RAN Publ., 2017, pp. 62–63.

9. Mil'man YU.V., CHugunova S.I., Goncharova I.V. *Harakteristika plastichnosti, opredelyaemaya metodom indentirovaniya. Voprosy atomnoj nauki i*

tekhniki [Plasticity characteristic determined by indentation method. Issues of Atomic Science and Technology], 2011, no. 4. *Seriya: Fizika radiacionnyh povrezhdenij i radiacionnoe materialovedenie* (98) [Series: Physics of Radiation Damage and Radiation Materials Science], pp. 182–187.

10. Sandomirski S.G. Estimation of the Ultimate Tensile Strength of Steel from Its HB and HV Hardness Numbers and Coercive Force. *Russian Metallurgy (Metally)*, vol. 2017, no. 11, pp. 989–993.
DOI: 10.1134/S003602951711012X

11. Rudenko S.P., Val'ko A.L., Parfenchik V.N. Influence of Sulfur on the Anisotropy of the Plastic Properties in Structural Steel. *Steel in Translation*. February 2018, vol. 48, iss. 2, pp. 126–129.
DOI: 10.3103/S0967091218020122

12. Bykov YU.A., Karpuhin S.D., Panfilov YU.V., Bojchenko M.K., CHepcov V.O., Osipov A.V. *Izmerenie tverdosti tonkih plenok* [Measuring the hardness of thin films]. *Metallovedenie i termicheskaya obrabotka metallov* [Metallurgy and heat treatment of metals], 2003, no. 10, pp. 32–35.

Devices and Methods of Measurements
2022, vol. 13, no. 3, pp. 199–207
V.A. Solodukha et al.

Spectral Ellipsometry as a Method of Investigation of Influence of Rapid Thermal Processing of Silicon Wafers on their Optical Characteristics

V.A. Solodukha, U.A. Pilipenko, A.A. Omelchenko, D.V. Shestovski

*JSC "Integral" – "Integral" Holding Management Company,
Kazinca str.,121A, Minsk 220108, Belarus*

*Received 26.07.2022
Accepted for publication 29.09.2022*

Abstract

One of the possible ways of improvement of the surface properties of silicon is the solid phase recrystallization of the surface silicon layer after the chemical-mechanical polishing with application of the rapid thermal treatment with the pulses of second duration. The purpose of the given paper is investigation of influence of the rapid thermal treatment of the initial silicon wafers of the various doping level and reticular density on their optical characteristics by means of the spectral ellipsometry method.

The investigation results are presented by means of the spectral ellipsometry method of the rapid thermal processing influence on the initial silicon wafers (KDB12 orientation <100>, KDB10 orientation <111> and KDB0.005 orientation <100>) of the various level of doping and reticular density influence on their optical characteristics: refraction and absorption ratios. Influence was confirmed of the silicon reticular density on its optical characteristics before and after the rapid thermal processing. It was shown, that reduction of the refraction and absorption ratios in the center of the Brillouin zone for the silicon samples with the high Boron concentration after the rapid thermal processing as compared with the low doped silicon. In the area of the maximum absorption peak, corresponding to the energy of the electron exit from the silicon surface (4.34 eV) the refraction indicator of the high doped silicon becomes higher, than of the low doped silicon, which is determined by the high concentration of the vacant charge carriers on the silicon surface in this spectral range.

It was established, that the spectral area 3.59–4.67 eV, corresponding to the work of the electrons, exiting the silicon surface, the most informative way shows the difference of the 3 optical parameters of silicon of the different orientation, and for evaluation of influence of the silicon doping level on its optical characteristics the most informative is the spectral range of 3.32–4.34 eV.

Keywords: rapid thermal processing, absorption ratio; refraction ratio.

DOI: 10.21122/2220-9506-2022-13-3-199-207

Адрес для переписки:
*Омельченко А.А.
ОАО «ИНТЕГРАЛ» – управляющая компания холдинга «ИНТЕГРАЛ»,
ул. Казинца, 121А, г. Минск 220108, Беларусь
e-mail: anna.omelchenko.13177@mail.ru*

Address for correspondence:
*Omelchenko A.A.
JSC "Integral" – "Integral" Holding Management Company,
Kazinca str.,121A, Minsk 220108, Belarus
e-mail: anna.omelchenko.13177@mail.ru*

Для цитирования:
V.A. Solodukha, U.A. Pilipenko, A.A. Omelchenko, D.V. Shestovski.
Spectral Ellipsometry as a Method of Investigation of Influence of Rapid Thermal Processing of Silicon Wafers on their Optical Characteristics.
Приборы и методы измерений.
2022. – Т. 13, № 3. – С. 199–207.
DOI: 10.21122/2220-9506-2022-13-3-199-207

For citation:
V.A. Solodukha, U.A. Pilipenko, A.A. Omelchenko, D.V. Shestovski.
Spectral Ellipsometry as a Method of Investigation of Influence of Rapid Thermal Processing of Silicon Wafers on their Optical Characteristics.
Devices and Methods of Measurements.
2022, vol. 13, no. 3, pp. 199–207.
DOI: 10.21122/2220-9506-2022-13-3-199-207

Спектральная эллипсометрия как метод изучения влияния быстрой термообработки кремниевых пластин на их оптические характеристики

В.А. Солодуха, В.А. Пилипенко, А.А. Омельченко, Д.В. Шестовский

*ОАО «ИНТЕГРАЛ» – управляющая компания холдинга «ИНТЕГРАЛ»,
ул. Казинца, 121А, г. Минск 220108, Беларусь*

Поступила 26.07.2022
Принята к печати 28.09.2022

Одним из возможных путей улучшения поверхностных свойств кремния является твердофазная рекристаллизация поверхностного слоя кремния после химико-механической полировки с использованием быстрой термической обработки импульсами секундной длительности. Целью данной работы являлось исследование влияния быстрой термической обработки исходных кремниевых пластин различного уровня легирования и ретикулярной плотности на их оптические характеристики методом спектральной эллипсометрии.

Приведены результаты исследования методом спектральной эллипсометрии влияния быстрой термообработки исходных кремниевых пластин (КДБ-12 ориентации <100>, КДБ-10 ориентации <111> и КДБ-0,005 ориентации <100>) различного уровня легирования и ретикулярной плотности на их оптические характеристики: коэффициенты преломления, поглощения. Подтверждено влияние ретикулярной плотности кремния на его оптические характеристики до и после быстрой термообработки. Установлено уменьшение коэффициентов преломления и поглощения в центре зоны Бриллюэна для образцов кремния с высокой концентрацией бора после быстрой термообработки по сравнению с низколегированным кремнием. В области пика максимума поглощения, соответствующего энергии выхода электрона с поверхности кремния (4.34 эВ) показатель преломления высоколегированного кремния становится выше, чем у низколегированного кремния, что обусловлено высокой концентрацией свободных носителей заряда на поверхности кремния в этом спектральном диапазоне.

Установлено, что спектральная область 3.59–4.67 эВ, соответствующая работе выхода электронов с поверхности кремния, наиболее информативно показывает различие оптических параметров кремния различной ориентации, а для оценки влияния уровня легирования кремния на его оптические характеристики наиболее информативен спектральный диапазон 3.32–4.34 эВ.

Ключевые слова: быстрая термическая обработка, коэффициент поглощения, коэффициент преломления.

DOI: 10.21122/2220-9506-2022-13-3-199-207

Адрес для переписки:
Омельченко А.А.
ОАО «ИНТЕГРАЛ» – управляющая компания холдинга «ИНТЕГРАЛ»,
ул. Казинца, 121А, г. Минск 220108, Беларусь
e-mail: anna.omelchenko.13177@mail.ru

Address for correspondence:
Omelchenko A.A.
JSC "Integral" – "Integral" Holding Management Company,
Kazinca str.,121A, Minsk 220108, Belarus
e-mail: anna.omelchenko.13177@mail.ru

Для цитирования:
V.A. Solodukha, U.A. Pilipenko, A.A. Omelchenko, D.V. Shestovski.
Spectral Ellipsometry as a Method of Investigation of Influence of Rapid Thermal Processing of Silicon Wafers on their Optical Characteristics.
Приборы и методы измерений.
2022. – Т. 13, № 3. – С. 199–207.
DOI: 10.21122/2220-9506-2022-13-3-199-207

For citation:
V.A. Solodukha, U.A. Pilipenko, A.A. Omelchenko, D.V. Shestovski.
Spectral Ellipsometry as a Method of Investigation of Influence of Rapid Thermal Processing of Silicon Wafers on their Optical Characteristics.
Devices and Methods of Measurements.
2022, vol. 13, no. 3, pp. 199–207.
DOI: 10.21122/2220-9506-2022-13-3-199-207

Introduction

The main factor, influencing the quality and reliability of the modern integrated circuits is the surface condition of the initial silicon wafers. In view of this, a great attention is paid to the aspects of the silicon surface preparation. As it is known, one of the possible ways of improving the surface properties of silicon is the solid phase recrystallization of the silicon surface layer after the chemical-mechanical polishing with application of the rapid thermal processing (RTP) with the pulses one second long [1, 2]. The important parameters, bearing information about the surface condition of the silicon wafer are in its optical characteristics, and, namely, the ratios of refraction, absorption and reflection, which are most sensitive to presence of the disrupted layer, available on the surface of the silicon wafers after the chemical-mechanical polishing [3]. However no references in publications have been found which are dedicated to reviewing the dependence of optical properties of silicon wafers upon its orientation and the level of doping in broad spectral range, that is from visible light to deep ultraviolet prior to RTP and after that.

The purpose of the given paper was investigation of influence of the rapid thermal treatment of the initial silicon wafers of the various doping level and reticular density on their optical characteristics by means of the spectral ellipsometry method.

Procedure of the experiment

As one of the most sensitive control methods of the optical characteristics of the silicon surface layers is the method of ellipsometry, based on the analysis of the characteristics of the reflected polarized irradiation, the given method was used during performance of the given investigations. Taking into consideration, that the ellipsometrical analysis should be performed in the wide spectral range, as the equipment for the investigations, the use was made of the spectral ellipsometer UVISEL 2, that ensures operation in the spectral range from 2100 to 200 nm (0.6–6.0 eV) and to obtain the results of high accuracy, resolution and the excellent ratio of signal/noise.

As the samples we used the wafers of the initial silicon with the diameter of 100 mm, in particular, of KDB12 orientation <100> (hereinafter – KDB12<100>), KDB10 orientation <111> (hereinafter – KDB10<111>) and KDB0.005 orientation <100> (hereinafter – KDB0.005<100>), that passed the standard chemical-mechanical polishing.

Measurements of the refraction ratio and the absorption ratio of the initial samples were performed on the spectral ellipsometer UVISEL 2 (made by the company Horiba Scientific, France, in the spectral range from 0.6–6.0 eV (2100–200 nm.)). The angle of arrival of the light beam on the sample constituted 70°. Treatment of the spectra and their visualization were performed with application of the software UVISEL 2.

Further, the given samples were subjected to the rapid thermal processing with irradiation by means of the light pulse from the non-operational side of the wafer for 7 s in the medium of Ar (the annealing temperature of 1100 °C). After completion of the process of the rapid thermal processing the initial samples were repeatedly subjected to control of the optical parameters.

Analysis of the initial silicon wafers before rapid thermal processing

As silicon in the infrared zone is transparent, the predominant interest lies in the investigation results of the optical characteristics of the silicon surface in the ultraviolet and visible range of the spectrum of 1.6–6 eV (760–200 nm). Analysis of the given results showed, that in the spectral range from 1.6 to 3.33 eV for the silicon samples of the various orientation and the doping concentration one can observe the “normal dispersion”, i. e. there’s increase of the silicon refraction ratio with reduction of the irradiation wave length. During transition into the ultraviolet zone of the spectrum there takes place the abrupt reduction of the refraction ratio, i. e. in evidence is the “anomalous dispersion” of the refraction ratio. Usually it is observed in the areas of the frequencies, corresponding to the bands of the intensive light absorption in the given medium, which is present in the given case. This is determined by the fact, that during influence of the ultraviolet irradiation there’s concentration rise of the charge carriers because of bond ruptures of Si-Si (bond energy of Si-Si is equal to 2.3 eV). As a result of this, in the spectral zone from 3.33 to 6 eV there takes place the “anomalous dispersion” of the silicon refraction ratio close to the maximum absorption points (see Figures 1, 3), corresponding to:

– G-point (Van Hove singularity point M1) of the Brillouin zone center with the energy of 3.46–3.48 eV (the energy of the direct transition of 3.43 eV) (see Figures 1, 3, point 2, curves *c*, *d*, *h*);

– maximum absorption, that corresponds to the energy of the electrons, exiting the silicon surface of 4.34 eV (exit work of electron for Si is equal to 3.59–4.67 eV) (see Figures 1, 3, point 4, curves *c*, *d*, *h*);

– maximum absorption, corresponding to the energy of the electrons, exiting the natural oxide surface due to rupture of the bonds Si-O about 5.42 eV (the bond energy of Si-O is equal to 4.79 eV).

The spectral dependence of the reflection ratio *R*, as a rule, hardly depends on the photon energy, and the spectral changes in the intensity of the reflected beam are related mainly to alterations of the absorption ratio. Thus, the spectral dependence of the reflection ratio *R* has the similar expression of the absorption ration dependence. Meanwhile, it is specific with the spikes of the maximum reflection in the area of 3.42 eV (when adjacent to the G-point of the Brillouin zone center) (see Figures 2, 4, point 5, curves *i*, *f*, *e*), 4.6 eV (corresponding to the electron exit work from the silicon surface) (see Figures 2, 4, point 6, curves *i*, *f*, *e*) and about 5.75 eV (corresponding to the energy rupture of the bonds Si-O) (see Figures 2, 4) [4, 5].

The comparative analysis of the optical parameters of the silicon samples KDB12<100> and KDB10<111> with the different orientation of the surface revealed (see Figures 1, 2), that in the region of the refraction ratio maxima, corresponding to the energy of 3.33–3.34 eV (see Figure 1, point 1, curves *a*, *b*), 4.1 eV (see Figure 1, point 3, curves *a*, *b*), as well as in the region of the maximum absorption, corresponding to the energy of the electrons, exiting the silicon surface with the value of 4.34 eV (see Figure 1, point 4, curves *c*, *d*) for the silicon orientation <111> the ratios of absorption, refraction and reflection are greater than for the silicon with orientation <100>. In the absorption maximum of the G-point (Van Hove singularity point M1) of the Brillouin zone center (see Figure 1, point 2, curves *c*, *d*) the absorption ratio for the silicon with orientation <111> is greater than for the silicon with orientation <100> by $\Delta k = 0.03$, but in a different way behaves the refraction indicator with the difference $\Delta n = 0.065$. It is explained by the fact, that in the plane {111} the atoms packs are of the maximum density, i. e. the silicon of orientation <111> possesses the higher reticular density [6, 7].

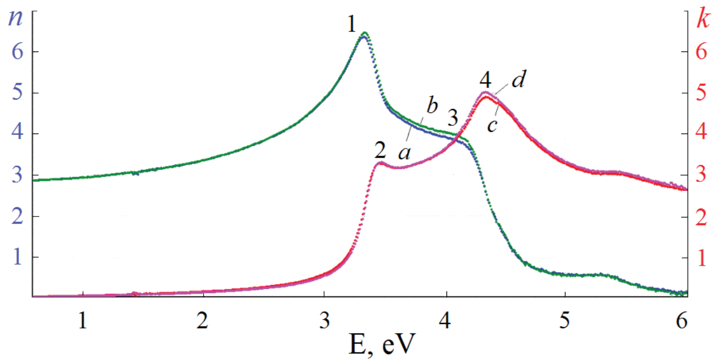

Figure 1 – Spectral dependence of the absorption *k* and refraction *n* ratios of the initial silicon KDB12<100> and KDB10<111> before rapid thermal processing: *a* – *n* KDB12<100>; *b* – *n* KDB10<111>; *c* – *k* KDB12<100>; *d* – *k* KDB10<111>

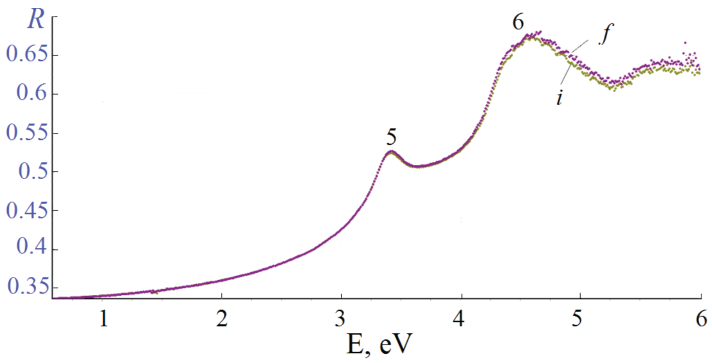

Figure 2 – Spectral dependence of reflection *R* ratios of the initial silicon KDB12<100> (*i*) and KDB10<111> (*f*) before rapid thermal processing

Devices and Methods of Measurements
2022, vol. 13, no. 3, pp. 199–207
V.A. Solodukha et al.

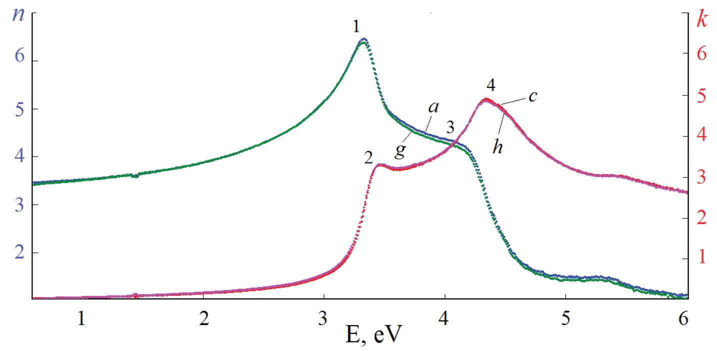

Figure 3 – Spectral dependence of the absorption *k* and refraction *n* ratios of the initial silicon KDB12<100> and KDB0.005<100> before rapid thermal processing: *a* – *n* KDB12<100>; *c* – *k* KDB12<100>; *g* – *n* KDB0.005<100>; *h* – *k* KDB0.005<100>

Meanwhile, for the spectral region nearby the maximum point of the refraction ratio with the energy of 4.1 eV one can observe the greatest difference of $\Delta n = 0.126$, and in the maximum of absorption with the energy of 4.34 eV (see Figure 1, point 4, curves *c*, *d*) the absorption ratio of the silicon with orientation <111> is higher by $\Delta k = 0.118$ than for the silicon with orientation <100>. The given result can be explained by influence of the higher concentration of the vacant charge carriers on the silicon surface with orientation <111> in this spectral range.

From this it ensues, that the spectral region 3.59–4.67 eV, determined by the electrons work, exiting the silicon surface, is more informative in demonstration of the difference of the optical parameters of the silicon of the different orientation.

Investigation of the silicon doping level influence on its optical characteristics on the samples KDB12<100> and KDB0.005<100>, possessing the same orientation and the different doping degree, revealed (see Figures 3, 4), that the maxima of the refraction ratios in the region of energy of 3.33 eV (see Figure 3, point 1, curves *a*, *g*) and 4.1 eV (see Figure 3, point 3, curves *a*, *g*), as well as in the maximum of the absorption ratio of the G-point (Van Hove singularity point M1) of Brillouin zone center (see Figure 3, point 2, curves *c*, *h*) for the silicon with the high concentration of Boron KDB0.005<100> the higher values of the absorption ratios are observed, but the lower values of the refraction indicators than for the silicon KDB12<100> with the difference $\Delta n = 0.082$, $\Delta k = 0.081$, 0.014, 0.016. The given result is determined by step-up in deformation of the silicon crystal lattice with the higher doses of its doping and with the significant content of the point defectswith the higher concentration of the Boron admixture in silicon. And, consequently, in the region of the absorption maximum, corresponding to the exit energy of the electrons from the silicon surface of 4.34 eV (see Figure 3, point 4, curves *c*, *h*) resulting in the additional appearance of the vacant charge carriers on the silicon surface, which is confirmed by the lower value of by refraction ratio by $\Delta n = 0.084$, of the absorption ratio by $\Delta k = 0.056$, than in case of the low alloy silicon. The given circumstance is explained, as it is shown in [8], by dependence of the silicon optical characteristics on concentration of the vacant charge carriers on the silicon surface.

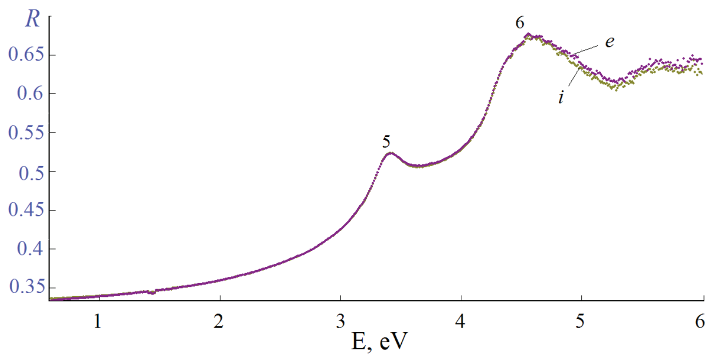

Figure 4 – Spectral dependence of the reflection *R* ratios of the initial silicon KDB12<100> (*i*) and KDB0.005<100> (*e*) before rapid thermal processing

On the basis of this it follows, that for assessment of the silicon doping level influence on its optical characteristics the most informative range is the spectral range of 3.32–4.34 eV.

Analysis of the initial silicon wafers after the rapid thermal processing

Analysis of dependences of the ratios of refraction, absorption and reflection in the spectral range of 0.6–6 eV after RTP showed (see Figure 5), that they are of the same nature as prior to treatment.

The comparative analysis of the optical parameters of the silicon samples KDB12<100> and KDB10<111> with the different orientation of the surface, i. e. possessing the different reticular density, revealed (see Table 1), that after RTP in the region of maxima of the refraction ratio, corresponding to the energy of 3.33–3.34 eV (see Table 1, point 1), 4.1 eV (see Table 1, point 3), as well as in the region of the absorption maxima, corresponding to the G-point (Van Hove singularity point M1) of Brillouin zone center (see Table 1, point 2) and the exit energy of the electrons from the silicon surface of 4.34 eV (see Table 1, point 4) for the silicon of orientation <111> the ratios of absorption, refraction and reflection were greater than for the silicon of orientation <100>.

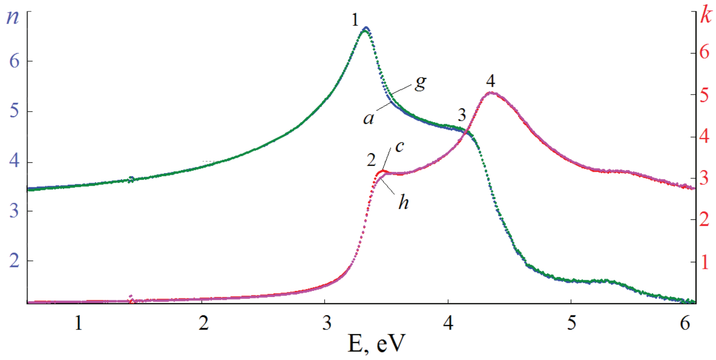

Figure 5 – Spectral dependence of the absorption *k* and refraction *n* ratios of the initial silicon KDB12<100> and KDB0.005<100> after the rapid thermal treatment: a – *n* KDB12<100>; *c* – *k* KDB12<100>; *g* – KDB0.005<100> *n*; *h* – *k* KDB0.005<100>

This has the analogous explanation, as in the case of the initial samples: the planes {111} possess the maximum density of the atoms packing, i. e. the silicon of orientation <111> possesses the higher reticular density [6, 7], and, consequently, in the result of the solid phase recrystallization of the disrupted layer after RTP the smaller deformation potential and the denser natural oxide.

In the absorption maximum with the energy of 4.34 eV the refraction indicator of the silicon of orientation <100> is slightly greater by $\Delta n = 0.004$, than for the silicon with orientation <111>. The given result can be explained by influence of the higher concentration of the vacant charge carriers on the silicon surface in this spectral range [8].

Meanwhile, for the spectral area nearby the maximum point of the refraction ratio with the energy of 4.1 eV one can observe the significant difference of $\Delta n = 0.098$, and in the absorption maximum with the energy of 4.34 eV the difference by the absorption ratio also rises and constitutes $\Delta k = 0.077$. On the basis of this it ensues, that the spectral area of 3.59–4.67 eV, determined by the exit work of the electron from the silicon surface, is more informative in demonstration of the difference in the optical parameters of silicon of the different orientation [6].

Investigation of the silicon doping level influence on its optical characteristics on the samples KDB12<100> and KDB0.005<100>, possessing the same orientation and the different doping degree, showed (see Table 2), that in the region of the absorption maxima, corresponding to the G-point (Van Hove singularity point M1) of Brillouin zone center (see Table 2, point 2) and the exit energy of the electrons from the silicon surface of 4.34 eV (see Table 2, point 4) for the silicon with the high concentration of Boron KDB0.005<100> one can observe the lower va-lues of the optical parameters, than for the silicon KDB12<100>. Just like indicated above, in the region of the refraction ration maximum point, corresponding to the energy of 3.32–3.33 eV (see Table 2, point 1).

For the lightly doped silicon KDB12<100> this can be explained by depletion of the surface layer with Boronbecause of its diffusion to the surface and the subsequent escape into the surrounding environment at the high temperatures of RTP. In case of silicon with the high admixture concentration, despite depletion of the surface layer, deformation of the crystal lattice will be higher, as there's a significant content of the point defects, and, consequently, the optical parameters turn out to be lower, than with the lightly doped silicon.

Table 1

Measurement results of the optical parameters of the silicon wafers after the rapid thermal processing

After RTP		KDB12<100>	KDB10<111>	Δ
1	*R*	0.508	0.511	0.003
	k	1.972	2.043	0.071
	n	6.669	6.722	0.053
	E(eV)	3.33	3.34	0.01
2 (G-point of the conductivity zone)	*R*	0.517	0.519	0.002
	k	3.168	3.193	0.025
	n	5.495	5.549	0.054
	E(eV)	3.48	3.48	0
3	*R*	0.544	0.545	0.001
	k	3.886	3.907	0.021
	n	4.611	4.709	0.098
	E(eV)	4.1	4.1	0
4 (exit energy of electrons from the silicon surface)	*R*	0.631	0.636	0.005
	k	5.053	5.13	0.077
	n	3.502	3.498	-0.004
	E(eV)	4.34	4.34	0

Table 2

Measurement results of the optical parameters of the silicon wafers after the rapid thermal processing

After RTP		KDB12<100>	KDB0.005 <100>	Δ
1	*R*	0.508	0.502	-0.006
	k	1.972	1.829	-0.143
	n	6.669	6.597	-0.072
	E(eV)	3.33	3.32	-0.001
2 (G-point of the conductivity zone)	*R*	0.517	0.514	-0.003
	k	3.168	3.102	-0.066
	n	5.495	5.454	-0.041
	E(eV)	3.48	3.51	0.03
3	*R*	0.544	0.545	0.001
	k	3.886	3.908	0.022
	n	4.611	4.665	0.054
	E(eV)	4.1	4.1	0
4 (exit energy of electrons from the silicon surface)	*R*	0.631	0.629	-0.002
	k	5.053	5.042	-0.011
	n	3.502	3.545	0.043
	E(eV)	4.34	4.34	0

Devices and Methods of Measurements
2022, vol. 13, no. 3, pp. 199–207
V.A. Solodukha et al.

The growth concentration of the ionized acceptors of the heavily doped silicon KDB0.005<100> at the high temperatures of RTP results in the increase and the effect of widening absorption in the region of the G-point of the conductivity zone, which explains the peak shift of the G-point to the value of 3.51 eV (see Figure 5, point 2, curves *c*, *h*) [9].

It should be also noted, that in the region of the refraction ration maximum point with the energy of 4.1 eV for silicon with the high Boron concentration KDB0.005<100> one can observe the higher values of the optical parameters, than for silicon KDB12<100>. Thus, in the absorption maximum point with the energy of 4.34 eV (see Table 2, point 4) the refraction indicator of the heavily doped silicon is greater by $\Delta n = 0.043$, than with KDB12<100>. The obtained result can be explained by the fact, that in the given spectral range there's a higher concentration of the vacant charge carriers on the silicon surface, resulting in its diffusion into the surrounding environment at the high temperatures of heating. This means, that after RTP the surface layer is depleted with the vacant charge carriers, and, consequently, in compliance with [8, 10] there should be the rise in the optical characteristics of silicon.

For the spectral area near the refraction ration maximum point with the energy of 3.32–3.33 eV one can observe the following alteration of the optical characteristics: $\Delta k = 0.143$, $\Delta n = 0.072$, $\Delta R = 0.006$. At the same time in the maximum of absorption with the energy of 4.48–3.51 eV the difference by the absorption ratio is more significant ($\Delta k = 0.066$), than with the energy value of 4.34 eV.

This means, that for evaluation of influence of the silicon doping level on its optical characteristics the most informative is the spectral range of 3.32–4.34 eV.

Conclusion

By means of the spectral ellipsometry method under investigation was influence of the rapid thermal treatment of the initial silicon wafers of the various doping level and reticular density on their optical characteristics.

Thus, influence was confirmed of the reticular density of silicon of the different orientation on its optical characteristics before and after rapid thermal processing. The significant reduction was established of the ratios of refraction and absorption in the center of Brillouin zone for the silicon samples with the high concentration of Boron after rapid thermal processing as compared with the low alloy silicon because of the more considerable depletion of the silicon surface with Boron in the first case as a result of the diffusion processes on the boundary of silicon-silicon dioxide. In the area of the absorption maximum peak, corresponding to the exit energy of the electron from the silicon surface, with the energy of 4.34 eV the refraction indicator of the heavily doped silicon becomes higher than in case of the low alloy silicon, which is determined by the high concentration of the vacant charge carriers on the silicon surface in this spectral range, resultant in the Boron diffusion into the sounding environment at the high temperatures of heating.

It has been ascertained that the spectral area 3.59–4.67 eV, corresponding to the electrons work function from silicon surface more exhaustively demonstrates the difference between the optical parameters of silicon with various orientation, and for estimation of the impact produced by the level of silicon doping at its optical characteristics the spectral range 3.32–4.34 eV happens to be more descriptive.

References

1. Nalivaiko O.Yu., Saladukha V.A., Pilipenka U.A., Kolos V.V., Belous A.I., Lipinskaya T.I. The Fundamental Technological Processes for Fabrication of the Semiconductor Devices and Integrated Circuits on Silicon. Vol. 1. Edited by Prof. A.S. Turtsevich. Minsk: Integralpolygraph Publ., 2013, 703 p.

2. Solodukha V.A., Gorushko V.A., Omelchenko A.A., Pilipenko V.A. Solid Phase Recrystallization of the Mechanically Disrupted Silicon Layer during the Rapid Thermal Processing. *Published Reports of the National Academy of Science of Belarus*, 2018, vol. 62, no. 3, p. 7, p. 6 (in Russian).

3. Bondarev V., Gorushko V., Pilipenko V., Solo-dukha V. Characteristic Features of Heating SemiconductorSilicon Structures during the Rapid Thermal Processing in the VLSI Technology. *High Temperature Material Process: An International Quarterly of High-Technology Plasma Processes*, 2018, vol. 22, iss. 1, pp. 1–6.
DOI: 10.1615/HighTempMatProc.2018026506

Devices and Methods of Measurements
2022, vol. 13, no. 3, pp. 199–207
V.A. Solodukha et al.

4. Tolstoi V.P. Introduction to Optical Absorption Spectroscopy of Nano-Materials. St.Peterburg, SOLO Publ., 2014, pp. 21, 39–48.

5. Postnikov V.S. Optical Material Science. Perm, Publishing House at Perm State Research Technical University, 2013, pp. 22–38.

6. Orlov A.M., Kostishko B.M., Skvortzov A.A. Physical Fundamentals of Technology for Semiconductor Devices and Integrated Microcircuits. Uljanovsk, Uljanovsk State University, 2014, pp. 33–35.

7. Voroshilov Yu.V., Pavlishin V.I. Fundamentals of Crystallography and Crystal Chemistry. Radiographic Analysis of Crystal, Ukraine, TOV “KNT”, 2011, pp. 80–84.

8. Kononenko V.V., Zavedeev E.V., Latushko M.I., Pashinin V.P., Konov V.I., Dianov E.M. Excitation of the Electronic Subsystem of Silicon by Means of the femtosecond laser irradiation. *Quantum Electronics*, 2012, vol. 42, no. 10, p. 925–930 (in Russian).

9. Pikhtin A.N., Khegazee Kh.Kh. Edge of Proper Absorption of Semiconductor Solid Solutions with Straight Structure of Energy Bands. *Semiconductor Physics and Engineering*, 2009, vol. 43, iss. 10, pp. 1301–1307 (in Russian).

10. Khirunenko L.I., Pomozov Yu.V., Sosnin M.G. Optical Properties of Silicon with High Boron Content. *Semiconductor Physics and Engineering*, 2013, vol. 47, iss. 2, pp. 232–238 (in Russian).

Devices and Methods of Measurements
2022, vol. 13, no. 3, pp. 208–215
V.M. Romanchak, P.S. Serenkov

Non-Additive Quantity Measurement Model

V.M. Romanchak, P.S. Serenkov

Belarusian National Technical University,
Nezavisimosty Ave., 65, Minsk 220013, Belarus

Received 15.08.2022
Accepted for publication 14.09.2022

Abstract

This work considers a model for measuring non-additive quantities, in particular a model for subjective measurement. The purpose of this work was to develop the measurement theory and form of a measurement model that uses the corrected S. Stevens measurement model.

A generalized structure was considered that included an empirical system, a mathematical system, and a homomorphism of the empirical system into a numerical system. The main shortcomings of classical measurement theories seem to be: 1) homomorphism does not display operations (in this case, one cannot speak of the meaningfulness of the model); and 2) there is no empirical measurement model that could confirm the existence of a homomorphism. To overcome the shortcomings of existing theories a definition of the measurement equation is given. As a result a measurement model is obtained that is free from the shortcomings of classical measurement theories. The model uses the corrected model of S. Stevens and the reflection principle of J. Barzilai.

The measurement model was tested using laws that were obtained empirically. Using the model it is shown that Fechner's empirical law is equivalent to Stevens's empirical law. This means that the problem which has attracted attention of many researchers for almost a century, has been solved.

A numerical example demonstrates the possibilities of the proposed measurement model. It is shown that the model can be used for extended analysis of expert assessments.

Keywords: measurement theory, Fechner's law, Stevens' law, Rasch model, concept of meaningfulness.

DOI: 10.21122/2220-9506-2022-13-3-208-215

Адрес для переписки:
Серенков П.С.
Белорусский национальный технический университет,
пр-т Независимости, 65, г. Минск 220013, Беларусь
e-mail: pavelserenkov@bntu.by

Address for correspondence:
Serenkov P.S.
Belarusian National Technical University,
Nezavisimosty Ave., 65, Minsk 220013, Belarus
e-mail: pavelserenkov@bntu.by

Для цитирования:
V.M. Romanchak, P.S. Serenkov.
Non-Additive Quantity Measurement Model.
Приборы и методы измерений.
2022. – Т. 13, № 3. – С. 208–215.
DOI: 10.21122/2220-9506-2022-13-3-208-215

For citation:
V.M. Romanchak, P.S. Serenkov.
Non-Additive Quantity Measurement Model.
Devices and Methods of Measurements.
2022, vol. 13, no. 3, pp. 208–215.
DOI: 10.21122/2220-9506-2022-13-3-208-215

Devices and Methods of Measurements
2022, vol. 13, no. 3, pp. 208–215
V.M. Romanchak, P.S. Serenkov

Модель измерения неаддитивной величины

В.М. Романчак, П.С. Серенков

*Белорусский национальный технический университет,
пр-т Независимости, 65, г. Минск 220013, Беларусь*

*Поступила 15.08.2022
Принята к печати 14.09.2022*

Предложена модель измерения неаддитивной величины, в частности модель субъективного измерения. Целью данной работы являлось развитие теории измерений и формирование модели субъективного измерения. Для обоснования модели использована скорректированная модель Стивенса.

Рассмотрена обобщенная структура модели измерения, которая включает эмпирическую систему, математическую систему и гомоморфизм эмпирической системы в числовую систему. Установлено, что основными недостатками классических теорий измерения являются: 1) гомоморфизм не отображает операции в системах, что позволило бы говорить об осмысленности теоретической модели измерений; 2) отсутствует модель эмпирического измерения, которая могла бы подтвердить существование гомоморфизма. Для преодоления недостатков существующих теорий определено уравнение измерения, связывающее результаты отображения эмпирической операции в числовую, а также сформулирована модель эмпирического измерения. Для построения модели измерения предложено использовать скорректированную модель Стивенса, которая дополнена принципом отражения Дж. Барзилая. В основу модели количественного измерения положены два способа измерений, с помощью которых эмпирически измеряется особый параметр – рейтинг, связанный с разностью или отношением искомых значений величины. Обосновано предположение о том, что оба способа измерения можно использовать совместно для измерения одной и той же величины. Причём результаты измерения будут в определённом смысле эквивалентны.

Показано, что такой подход позволяет получить модель количественного измерения, которая свободна от недостатков классических теорий измерения. Сформулирован алгоритм количественного измерения, а также принцип отражения, обеспечивающий соответствие эмпирической и числовой систем модели.

Предложенная модель измерения подтверждена эмпирически. С её помощью показано, что эмпирический закон Фехнера эквивалентен эмпирическому закону Стивенса. Тем самым получено решение классической проблемы субъективного измерения.

На конкретном примере продемонстрированы возможности предложенной модели измерения. Показано, что модель можно использовать для расширенного анализа экспертных оценок.

Ключевые слова: теория измерений, закон Фехнера, закон Стивенса, модель Раша, концепт осмысленности.

DOI: 10.21122/2220-9506-2022-13-3-208-215

Адрес для переписки:
*Серенков П.С.
Белорусский национальный технический университет,
пр-т Независимости, 65, г. Минск 220013, Беларусь
e-mail: pavelserenkov@bntu.by*

Address for correspondence:
*Serenkov P.S.
Belarusian National Technical University,
Nezavisimosty Ave., 65, Minsk 220013, Belarus
e-mail: pavelserenkov@bntu.by*

Для цитирования:
V.M. Romanchak, P.S. Serenkov.
Non-Additive Quantity Measurement Model.
Приборы и методы измерений.
2022. – Т. 13, № 3. – С. 208–215.
DOI: 10.21122/2220-9506-2022-13-3-208-215

For citation:
V.M. Romanchak, P.S. Serenkov.
Non-Additive Quantity Measurement Model.
Devices and Methods of Measurements.
2022, vol. 13, no. 3, pp. 208–215.
DOI: 10.21122/2220-9506-2022-13-3-208-215

Introduction

Measurement theory permits us to consider both objective and subjective measures from a unified point of view. Objective measures are associated with metrology [1]. Metrology is the science of measuring. The basis of metrology is units of measurement. Metrology also includes measuring instruments. The theory of objective measures is well developed. The theory of subjective measurements is based on the opinions and assessments of experts and requires further development [2].

Measurement is currently referred to as the process of obtaining an experimental value or values of a quantity that can reasonably be attributed to a quantity [3]. Every science experiment should follow the basic principles of proper investigation. An objective experiment is carried out using technical devices. Subjective experiments are based on expert opinions, feelings, and general impressions. And, if the justification of an objective experiment is technical devices, then further development of the measurement theory is required to verify the adequacy of the results of the subjective measurements [4].

Measurement theory permits us to consider both objective and subjective measures from a unified point of view. Objective measures are associated with metrology. Metrology is the science of measuring. The basis of metrology is units of measurement. Metrology also includes measuring instruments. The theory of objective measures is well developed. The theory of subjective measurements is based on the opinions and assessments of experts and requires further development [5].

The additive representation of the measurement process assumes that the addition operation has an empirical meaning. Representative measurement theory was created to overcome the limitations of additive measurement theory [6–8], (Figure 1). The representational measurement theory was originated by S.S. Stevens and other scientists. Representational measurement theory is based on the properties of binary relations and defines measurement as a mapping between two relational structures, an empirical one and a numerical one. For simplicity, since algebraic operations can be reduced to relations without loss of generality, representative theory does not include algebraic operations.

Empirical system	Mapping	Mathematical system
Objects $A_1, A_2, A_1, \dots$ Relationships (A_i, A_j)	$u_i = u(A_i)$ depends on the type of measurement scale	Values of the magnitude $u_1, u_2, u_3, \dots$

Figure 1 – Model by representative measurement theory

S. Stevens (1946) believed that numerical values should be assigned to objects according to certain rules. A measurement scale is a classification that describes the assignment rules.

New trends have appeared in the theory of measurements, which should be taken into account to substantiate a model of measurement. For example, a mathematical model of an empirical system was considered [9–10]. The model for measuring is proposed in the papers [11–12]. Let the general measurement model (Figure 2) include an empirical system, a mathematical system, and a mapping from an empirical system to a mathematical system:

1. Empirical system. Objects of measurement $A_1, A_2, A_3, \dots$ and pairs of objects (A_i, A_j).

2. Mathematical system. u_i is a numerical value, and $(u_i - u_j)$ is the operation result.

3. Mapping. Each object A_i maps to a value u_i and each pair of objects (A_i, A_j) maps to the operation results $(u_i - u_j)$.

Mathematical model of an empirical system	Mapping	Mathematical system
Objects $A_1, A_2, A_3, \dots$	$u_i = u(A_i)$	Values of the magnitude $u_1, u_2, u_3, \dots$
Ordered pairs (A_i, A_j)	Measurement result $R_{ij} = R(A_i, A_j)$	The result of the operation $R(A_i, A_j) = u_i - u_j$

Figure 2 – General measurement model

Devices and Methods of Measurements
2022, vol. 13, no. 3, pp. 208–215
V.M. Romanchak, P.S. Serenkov

Objects are mapped to values by the function $u_i = u(A_i)$, and pairs of objects (A_i, A_j) are mapped to the difference of values $(u_i - u_j)$. Hence, there are two mappings (see Figure 2). Let the empirical system be an affine line. Let A_1, A_2 and A_3 are arbitrary points on a straight line, and (A_1, A_2), (A_2, A_3) and (A_1, A_3) are rigid rods (Figure 3). Let's measure the length of these rods (Figure 3).

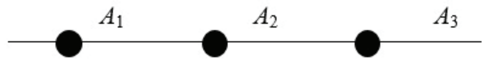

Figure 3 – Empirical system. The rod (A_1, A_3) consists of two rods (A_1, A_2) and (A_2, A_3)

The model for measuring the length of the rod (Figure 4) follows from the general measurement model (Figure 2).

Empirical system	Mapping	Mathematical system
Points on a straight line $A_1, A_2, A_3, \ldots$	$u_i = u(A_i)$	u_i – point coordinate values
Vectors $(A_1, A_2), (A_2, A_3), (A_1, A_3)$	Vector mapping $R_{ij} = R(A_i, A_j)$	Measurement equation $R(A_i, A_j) = u_i - u_j$

Figure 4 – Rod length measurement

Here the expression (A_i, A_j) means a vector. The point A_i is known as the start point, and the point A_j, is known as the end point. A vector is the result of an empirical measurement that characterizes the difference in position of two points on a straight line. Each vector (A_i, A_j) is assigned the value $R_{ij} = R(A_i, A_j)$. The formula $R(A_i, A_j) = u_i - u_j$ is used to calculate the measurement result. The formula $R(A_i, A_j) = u_i - u_j$ is used to determine the values of the quantity.

The measurement result of the vector (A_1, A_3) is equal to the sum of the measurement results of the vectors (A_1, A_2) and (A_2, A_3).

For the practical implementation of measurement, i. e., for empirical measurements, an appropriate model of measurement is needed. Stevens proposed a model in which he used a certain group of objects whose magnitude changed uniformly [4]. For example, in Figure 3, the position of points A_1, A_2 and A_3 on a straight line, changes uniformly. Then the vectors (A_1, A_2) and (A_2, A_3) are equal and, consequently, the measurement results of $R(A_1, A_2)$ and $R(A_2, A_3)$ coincide. Figure 5 shows the model of S.S. Stevens.

Empirical system	Mapping	Mathematical system
Vectors $(A_1, A_2), (A_2, A_3), (A_1, A_3)$	Vector mapping $R_{ij} = R(A_i, A_j)$	Measurement equation $R(A_i, A_j) = u_i - u_j$
Measurement $(A_1, A_2) = (A_2, A_3)$	Result mapping $R(A_1, A_2) = R(A_2, A_3)$	Measurement equation $u_1 - u_2 = u_1 - u_2$

Figure 5 – Empirical measurement model according to S. Stevens [4]

So far, the model for measuring the difference of values has been considered. A model for measuring the ratio of values can be obtained in a similar way. The Stevens model contains two measurement equations: for the difference and for the ratio of quantities. In the first case, the values are determined on a scale of intervals; in the second case, on a log-interval scale. S. Stevens used this model of measurement to classify measurement scales [4]. It only remains to add that the Stevens classification also needs to be corrected.

The aim of the work was to develop the theory of measurements based on the corrected model of measurements by S.S. Stevens. This work is a continuation of the work [11–12].

A critical analysis of the Stevens measurement model

The four scales were suggested by S.S. Stevens in 1946. Later, in 1957, S. Stevens added a fifth, the log-interval scale, but came to the conclusion that this scale was useless. And the logarithmic scale is no longer in use today. Stevens' model corresponds to the concept of realism. According to J. Michell [13–14], numbers are ratios between quantities and exist in space and time. An empirical relational system is posited as an objective, independently existing structure able to be numerically represented.

Such an empirical structure was considered in 1923 by the physicist A. Friedman. Following A. Friedman, let's axiomatically define "an exceptional group of objects that allows us to make a special evaluation". Let the objects A_1, A_2, A_3, … be sorted in ascending order of quantity, and the quantity of these objects changes uniformly; $u_i = u(A_i)$, where u_i is the value of the quantity; the differences in values $(u_{i+1} - u_i)$ are equal to each other: $u_2 - u_1 = u_3 - u_2 = \ldots = u_n - u_{n-1}$. In accordance with the definition of A. Friedman, such a special assessment is called a measurement. Difference values are defined using equality:

$$u_i - u_j = \lambda_1 (i - j), \tag{1}$$

where λ_1 is an unknown constant, $\lambda_1 > 0$. The values u_j are determined by a linear transformation, that is, on the interval scale.

Let $v_i = v(A_i)$, where v_i is the value of the quantity and the rations of the values are equal: $v_2/v_1 = v_3/v_2 = \ldots = v_n/v_{n-1}$. Then the ratios of values are determined by the formula:

$$\ln (v_i/v_j) = \lambda_2 (i - j), \tag{2}$$

where λ_2 is an unknown constant, $\lambda_2 > 0$. The logarithms of the values are determined up to a linear transformation, i. e., on the scale of log-intervals scale. As a result, two measurement equations are obtained (1) and (2), with two different measurement operations: subtraction and division. Values are determined on an interval scale and a log-interval scale. S.S. Stevens used a similar measurement model to classify measurement scales.

The concept of measurement scales looks convincing, and only the "unnecessary" fifth scale breaks the logic. S.S. Stephens thought a log scale was mathematically interesting, but it, like many mathematical models, has proven empirically useless. Such a claim is controversial. Let's take an example of measuring a non-additive quantity. Density is an example of a non-additive quantity. Let the density of the two samples be equal to 1 kg/m^3 and 2 kg/m^3. Then the sum of densities is not defined, but the ratio of densities is defined.

Example. Let the densities of samples A_1, A_2, A_3, A_4 and A_5 change uniformly. Density values can be measured in two ways. 1. The difference between two density values is calculated by the formula (1) $u_i - u_j = i - j$, where u_i are the values that characterize the density; $i, j = 1, 2, ..., 5$; $\lambda_1 = 1$. The ratios of density values satisfy the equality $v_{i+1} / v_i = 2$, where v_i are the density values. To calculate the ratios, use the formula $(v_i / v_j) = (2^i / 2^j)$; $i, j = 1, 2, ..., 5$.

Density values u_i are determined up to a constant factor, while values v_i are determined up to an arbitrary constant. In a particular case, the values are given in Table 1. The values have a natural interpretation. For example, the third sample ($i = 3$) has a density four times greater than the first, or two orders of magnitude greater than the first.

Table 1

The density values are obtained on the interval and log-interval scales

Interval scale of "density" values u_i	1	2	3	4	5
Log-interval scale of density values v_i	2	2^2	2^3	2^4	2^5

The example confirms that if the value of objects A_1, A_2, ... changes uniformly, it is reasonable to consider two measurement scales: the intervals scale and the log-intervals scale (Table 1). Stevens believed that the scale of logarithmic intervals was useless [4]. But density is not defined on the scale of relations since density is a non-additive quantity. The density is determined on the logarithmic scale of intervals. Therefore, there is reason to believe that the Stevens model requires adjustment.

The measurement model (the adjusted Stevens model)

From equalities (1) and (2), it follows that the interval scale values and log interval scale values are interconnected by the formula:

$$(u_i - u_j) = \lambda \ln(v_i/v_j), \tag{3}$$

where $i, j = 1, 2, \ldots, n$; u_i and v_i are the values of the quantity; $\lambda = \lambda_2/\lambda_1$. It is straightforward to demonstrate that equality (3) is satisfied for the values u_i and v_i in Table 1.

Equality (3) means that the mapping $u = \ln(v)$ preserves the measurement operation: the ratio of values maps to the difference of values. In addition, for the values u_i and v_i, there is a one-to-one correspondence between the values of u_i and v_i using the mapping $u = \ln(v)$. The mapping $u = \ln(v)$ is an isomorphism of two algebraic structures: the set of positive integers under the operation of division, onto the set of real numbers under the operation of subtraction. As a result, isomorphic structures cannot be distinguished from one another solely on the basis of structure; they are equivalent [15].

During the measurement process each pair of objects is assigned a value $(u_i - u_j)$ or (v_i/v_j). This means that the result of an empirical measurement is equal to the result of an arithmetic operation and not the value of the quantity. To unify the measurement process, it is convenient to introduce a rating definition based on equality (3):

$$R_{ij} = \lambda_1(u_i - u_j); \tag{4}$$

$$R_{ij} = \lambda_2 \ln(u_i/v_j), \tag{5}$$

where $i, j = 1, 2, \ldots n$. The quantity values are u_i and v_i, $v_i > 0$, and the positive constants are λ_1, λ_2.

For objects whose quantity changes uniformly, the rating is determined up to a constant factor λ:

$$R_{ij} = \lambda(i - j). \tag{6}$$

Such a definition of the rating will be called classical. The classic definition of rating follows from the Stevens measurement model. The rating does not depend on the choice of measurement model (5) or (6). A direct check shows that the rating values satisfy the consistency condition:

$$R_{ij} = R_{ik} + R_{kj}. \tag{7}$$

The axiomatic model of measurement includes the compatibility condition (7) and two measurement models (4) and (5), where u_i and v_i are values, and R_{ij} are rating values. Let the values of the quantity be on the interval scale if they are the solution of the system of equations (5), and on the logarithmic scale if they are the solution of the system of equations (6). The ratio scale is an interval scale modified to include an inherent zero starting point. The ratio scale is an auxiliary scale.

As a result, a theoretical measurement model was obtained, which can be used for both subjective and objective measurements. For the measurement models the measurement algorithm is:

1. Select the measurement model (4) or (5).
2. Find the measurement results $(u_i - u_j)$ or (v_i/v_j).
3. Calculate the rating R_{ij}.
4. Check the compatibility conditions (7).
5. Select the measurement equation (4) or (5) and find the values of the measured quantity.

The values of the quantity are defined in the scale of intervals if they are the solution of the system of equations (5), and in the scale of log-intervals if they are the solution of the system of equations (5). The ratio scale is a scale of intervals in which the zero element, the reference point, is defined. The ratio scale is an auxiliary scale.

In addition, the measurement model follows the principles:

1. The principle of reflection. Operations within the mathematical system are applicable if and only if they reflect corresponding operations within the empirical system.
2. The principle of equivalence. The interval scale and the log-interval scale are equivalent.

From the equivalence principle, organically follows:

1. Fechner's law in the form of paired comparisons [11].
2. Stevens' law in the form of paired comparisons [11].
3. Rasch model [16].

Stevens' Experimental Law (1947) was proposed to replace Fechner's Experimental Law (1848). The contradiction between the laws of Fechner and Stevens still exists. The proposed model measurement solves this problem. In addition, the experimental laws of psychophysics follow from the measurement model (5) and (6). Thus, the measurement model has strong empirical support.

An example implementation of a quantification model

Five samples of the drinks are evaluated by seven experienced experts (ISO 11056). Drinks contain different amounts of caffeine. Let A_i be a coffee brand, k be the expert's serial number, and u_{ki} be assessments of the coffee brand. Table 2 shows the assessments of brands, u_{ki}.

Devices and Methods of Measurements
2022, vol. 13, no. 3, pp. 208–215
V.M. Romanchak, P.S. Serenkov

Table 2

Data related to the five samples

v_{ki}	A_1	A_2	A_3	A_4	A_5
1	10	20	35	40	70
2	8	20	38	44	85
3	8	20	36	40	75
4	7	15	32	37	70
5	12	25	38	40	75
6	12	22	35	40	80
7	9	18	35	40	84

The values were assigned based on the relation; if an attribute is twice as intense, it has been assigned a value twice as high. The assessment can be considered as a measurement on the log interval scale. Individual r_k ratings for each expert are calculated using the formula $r_{ki} = \ln(v_{ki}/v_{k1})$.

Table 3

Individual rating values

v_{ki}	A_1	A_2	A_3	A_4	A_5
1	0.00	0.69	1.25	1.39	1.95
2	0.00	0.92	1.56	1.70	2.36
3	0.00	0.92	1.50	1.61	2.24
4	0.00	0.76	1.52	1.67	2.30
5	0.00	0.73	1.15	1.20	1.83
7	0.00	0.61	1.07	1.20	1.90

The group rating R (Table 4) is calculated as the average of individual ratings (see Table 3) for each brand of coffee. A criterion for the consistency of expert assessments is proposed: the significance of the correlation coefficients ρ, $\rho_k = \rho(r_k, R)$. Correlation coefficients according to Student's t-test are significant with a significance level of 0.05. Therefore, the hypothesis of the consistency of expert assessments is accepted.

Table 4

Group assessment of the rating

A	A_1	A_2	A_3	A_4	A_5
R	0.00	0.76	1.35	1.47	2.10

The rating measurements can be used in demand forecasting and sales planning models. Suppose that the expert consistently compares all brands with the first one. Let p_i be the probability of choosing brand A_i in this situation. Then the ratios of probabilities p_i/p_1 are related to the rating by formula (6), which we write as:

$$R_i = \lambda \ln(p_i/p_1), \tag{8}$$

where λ for formula (7) can be found by using additional information. Formula 7 is the Rasch model [16].

The example shows that the measurement results can be interpreted using the rating definition. In the example under consideration, the scale of log intervals was chosen based on the recommendations for conducting such studies. To confirm that the measurement scale is log-interval, it is necessary to check (at least partially) the compatibility condition (3).

Conclusion

The measurement of non-additive quantities is a problem that was considered in this article. For example, subjective measurements are measurements of non-additive quantities. The analysis of modern works on the theory of measurements shows that this problem is still relevant. These problems are considered in the works of J. Barzilai and J. Michel. It has been established that there is no measurement equation in measurement theory that defines the natural connection between the empirical and mathematical systems.

The concept of realism has been applied to the formation of measurement models. In particular, this means that empirical structures that support measurement must naturally produce real numbers. The realistic principle for obtaining scale values is formed on the basis of the Stevens model. The Stevens model is the rationale for the classification of measurement scales. However, the analysis of the Stevens model showed that it needs to be refined.

Taking into account the concept of realism, a model of quantitative measurement is proposed. This model was used by S.S. Stevens for the classification of measurement scales.

The model includes two measurement operations. The result of a measurement operation is a difference or ratio of values. The definition of the rating allows you to consider both measurement operations at the same time. The rating is a generalized result of the measurement, which does not depend on the choice of the measurement operation. The assumption that both measurement operations can be used together to measure the same quantity is substantiated. Moreover, the measurement results in this case are equivalent. On this basis, the principle of equivalence is formulated.

An algorithm for quantitative measurement is formulated, as well as a reflection principle that ensures the correspondence between the empirical and mathematical systems.

The proposed model of measurement has convincing experimental confirmation. The model eliminated the contradiction between the empirical laws of Fechner and Stevens. It is shown that they are equivalent.

The definition of the measurement equation is given. The measurement equation maps an empirical system into a mathematical system. From the measurement equation follows the definition of the measurement scale. In general, the concept of measurement has been formed, which considers subjective and objective measurements from a single point of view.

An example of the application of the measurement model is given. It is shown that an extended analysis of expert assessments can be performed using a measurement model. Such an analysis can be used to solve the problem of forecasting supply and demand in the economy.

References

1. Raghavendra N.V., Krishnamurthy L. Engineering metrology and measurements. New Delhi: Oxford University Press, 2013, 676 p.

2. Maul A., Irribarra D.T., Wilson M. On the philosophical foundations of psychological measurement. *Measurement*, 2016, vol. 79, pp. 311–320.
DOI: 10.1016/j.measurement.2015.11.001

3. Joint Committee for Guides in Metrology-JCGM. JCGM 200: 2008. International vocabulary of metrology: basic and general concepts and associated terms (VIM), 2008.

4. Wichmann F.A., Jäkel F., Wixted J. Methods in psychophysics. *Stevens handbook of experimental psychology and cognitive neuroscience*, 2018, vol. 5, pp. 265–306.

5. Makransky G., Terkildsen T.S., Mayer R.E. Role of subjective and objective measures of cognitive processing during learning in explaining the spatial contiguity effect. *Learning and Instruction*, 2019, vol. 61, pp. 23–34. **DOI:** 10.1016/j.learninstruc.2018.12.001

6. Luce R.D., Suppes P., Krantz D.H. Foundations of measurement: representation, axiomatization, and invariance. *Courier Corporation*, 2007, vol. 3.

7. Cecconi P., Franceschini F., Galetto M. Measurements, evaluations and preferences: a scheme of classification according to the representational theory. *Measurement*, 2006, vol. 39, no. 1, pp. 1–11.
DOI: 10.1016/j.measurement.2005.10.012

8. Michell J. Representational measurement theory: Is its number up? *Theory & Psychology*, 2021, vol. 31, no. 1, pp. 3–23.
DOI: 10.1177/0959354320930817

9. Barzilai J. Preference function modelling: the mathematical foundations of decision theory. *Trends in multiple criteria decision analysis*, 2010, pp. 57–86.

10. Barzilai J. Demand theory is founded on errors. *Real-World Economic Review*, 2014, iss. 68, pp. 62–65.

11. Romanchak V.M. [Model of Rating of Non-Physical Quantity]. *Sistemnyj analiz i prikladnaya informatika* [System analysis and applied information science], 2017, no. 4, pp. 39–44 (in Russian).
DOI: 10.21122/2309-4923-2017-4-39-44

12. Romanchak V.M. [Subjective measurements (rating theory)]. *ZHurnal Belorusskogo gosudarstvennogo universiteta. Filosofiya. Psihologiya* [Journal of the Belarusian State University. Philosophy and Psychology], 2020, no. 3, pp. 87–98 (in Russian).

13. Michell J. The Rasch paradox, conjoint measurement, and psychometrics: Response to Humphry and Sijtsma. *Theory & Psychology*, 2014, vol. 24, no. 1, pp. 111–123. **DOI:** 10.1177/0959354313517524

14. Michell J. "The constantly recurring argument": Inferring quantity from order. *Theory & Psychology*, 2012, vol. 22, no. 3, pp. 255–271.
DOI: 10.1177/0959354311434656

15. Michell J. Constructs, inferences, and mental measurement. *New Ideas in Psychology*, 2013, vol. 31, iss. 1, pp. 13–21. **DOI:** 10.1016/j.newideapsych.2011.02.004

16. Dummit D.S., Foote R.M. Abstract algebra. Hoboken: Wiley Publ., 2004, vol. 3.

17. Briggs D.C. Interpreting and visualizing the unit of measurement in the Rasch Model. *Measurement*, 2019, vol. 146, pp. 961–971.
DOI: 10.1016/j.measurement.2019.07.035

17. Lubashevsky I. Psychophysical laws as reflection of mental space properties. *Phys. Life Rev.*, 2019, vol. 31, pp. 276–303.

Devices and Methods of Measurements
2022, vol. 13, no. 3, pp. 216–227
Y. Saukova, M. Hundzina

Tensor Calculus in Digital Colorimetry

Y. Saukova, M. Hundzina

Belarusian National Technical University,
Nezavisimosty Ave., 65, Minsk 220013, Belarus

Received 10.05.2022
Accepted for publication 17.08.2022

Abstract

Any object can have many implementations in the form of digital images and any digital image can be processed many times increasing or decreasing accuracy and reliability. Digital colorimetry faces the need to work out issues of ensuring accuracy, metrological traceability and reliability. The purpose of this work was to generalize approaches to the description of multidimensional quantized spaces and show the possibilities of their adaptation to digital colorimetry. This approach will minimize the private and global risks in measurements.

For color identification digital colorimetry uses standard color models and spaces. Most of them are empirical and are improved during the transition from standard to real observation conditions taking into account the phenomena of vision and the age of observers. From the point of view of measurement, a digital image can be represented by a combinatorial model of an information and measurement channel with the appearance of the phenomenon of a color covariance hypercube requiring a significant amount of memory for data storage and processing. The transition from the covariance hypercube to high-dimensional matrices and tensors of the first, second and higher ranks provides the prospect of optimizing the color parameters of a digital image by the criterion of information entropy.

Tensor calculus provides opportunities for expanding the dynamic range in color measurements describing multidimensional vector fields and quantized spaces with indexing tensors and decomposing them into matrices of low orders.

The proposed complex approach based on tensor calculus. According to this approach the color space is a set of directed vector fields undergoing sampling, quantization and coding operations. Also it is a dynamic open system exchanging information with the environment at a given level and to identify color with specified levels of accuracy, reliability, uncertainty and entropy.

Keywords: colorimetry, image, tensor, uncertainty, entropy.

DOI: 10.21122/2220-9506-2022-13-3-216-227

Адрес для переписки:
Савкова Е.Н.
Белорусский национальный технический университет,
пр-т Независимости, 65, г. Минск 220013, Беларусь
e-mail: savkova@bntu.by

Address for correspondence:
Saukova Y.
Belarusian National Technical University,
Nezavisimosty Ave., 65, Minsk 220013, Belarus
e-mail: savkova@bntu.by

Для цитирования:
Y. Saukova, M. Hundzina.
Tensor Calculus in Digital Colorimetry.
Приборы и методы измерений.
2022. – Т. 13, № 3. – С. 216–227.
DOI: 10.21122/2220-9506-2022-13-3-216-227

For citation:
Y. Saukova, M. Hundzina.
Tensor Calculus in Digital Colorimetry.
Devices and Methods of Measurements.
2022, vol. 13, no. 3, pp. 216–227.
DOI: 10.21122/2220-9506-2022-13-3-216-227

Тензорное исчисление в цифровой колориметрии

Е.Н. Савкова, М.А. Гундина

Белорусский национальный технический университет,
пр-т Независимости, 65, г. Минск 220013, Беларусь

Поступила 10.05.2022
Принята к печати 17.08.2022

Поскольку любой объект может иметь множество реализаций в виде цифровых изображений, а любое цифровое изображение может быть множество раз подвергнуто обработке, повышающей или понижающей точность и достоверность, цифровая колориметрия сталкивается с необходимостью проработки вопросов обеспечения точности, метрологической прослеживаемости и достоверности. Цель данной работы – обобщить подходы к описанию многомерных квантованных пространств и показать возможности их адаптации к цифровой колориметрии, что позволит минимизировать частные и глобальные риски, возникающие в измерениях.

Для идентификации цвета цифровая колориметрия использует стандартные цветовые модели и пространства, большинство из которых являются эмпирическими и совершенствуются при переходе от стандартных к реальным условиям наблюдения с учётом феноменов зрения и возраста наблюдателей. Цифровое изображение с точки зрения измерения может быть представлено комбинаторной моделью информационно-измерительного канала с возникновением феномена цветового ковариационного гиперкуба, требующего значительного объёма памяти для хранения и обработки данных. Переход от ковариационного гиперкуба к матрицам высоких размерностей и тензорам первого, второго и более высоких рангов предоставляет перспективу оптимизации цветовых параметров цифрового изображения по критерию информационной энтропии.

Тензорное исчисление предоставляет возможности расширения динамического диапазона в измерениях цвета, описания многомерных векторных полей и квантованных пространств с индексацией тензоров и разложением их на матрицы низких порядков.

Предложенный комплексный подход, основанный на тензорном исчислении, позволяет рассматривать цветовое пространство как совокупность направленных векторных полей, подвергающихся операциям дискретизации, квантования и кодирования, как динамическую открытую систему, обменивающуюся информацией с окружающей средой с заданным уровнем, и идентифицировать цвет с заданными уровнями точности, достоверности, неопределённости и энтропии.

Ключевые слова: колориметрия, изображение, тензор, неопределённость, энтропия.

DOI: 10.21122/2220-9506-2022-13-3-216-227

Адрес для переписки:
Савкова Е.Н.
Белорусский национальный технический университет,
пр-т Независимости, 65, г. Минск 220013, Беларусь
e-mail: savkova@bntu.by

Address for correspondence:
Saukova Y.
Belarusian National Technical University,
Nezavisimosty Ave., 65, Minsk 220013, Belarus
e-mail: savkova@bntu.by

Для цитирования:
Y. Saukova, M. Hundzina.
Tensor Calculus in Digital Colorimetry.
Приборы и методы измерений.
2022. – Т. 13, № 3. – С. 216–227.
DOI: 10.21122/2220-9506-2022-13-3-216-227

For citation:
Y. Saukova, M. Hundzina.
Tensor Calculus in Digital Colorimetry.
Devices and Methods of Measurements.
2022, vol. 13, no. 3, pp. 216–227.
DOI: 10.21122/2220-9506-2022-13-3-216-227

Introduction

Digital colorimetry focused on qualitative and quantitative methods for determining color from digital images faces the need to work out issues of ensuring accuracy, metrological traceability and reliability, since any object can have many implementations in the form of digital images, and any digital image can be processed many times, increasing or decreasing accuracy and reliability. It is because any object can have many implementations in the form of digital images, and any digital image can be processed many times, increasing or decreasing accuracy and reliability. Basic colorimetry assumes normalized observation conditions, and higher colorimetry includes "methods for assessing the perception of a color stimulus presented to an observer in a complex environment that we observe in everyday life" [1]. Methods of transmitting color information of an image in telecommunication systems are based on the use of the principles of higher colorimetry [2]. The concepts of "absolute" (differential) and "relative" colorimetry take into account the possibilities of color reproduction of technical means [3]. The idea of differential colorimetry consists in determining minor color differences on conditional virtual scales being developed for example in express methods of analytical measurements using a smartphone [4] terrain studies using satellite images [5, 6]. Relative colorimetry takes place in color-rendering systems allowing colors to be shifted taking into account the movement of the "white point" to a new position taking into account the limitations of the color coverage of technical devices [3, 7]. At the same time, there is a need to expand the dynamic range of digital images objectively limited by the color coverage of recording, transmitting and displaying devices in order to bring them as close as possible to the dynamic range of human vision (0.000001–100000000 cd/m^2) [8, 9].

In areas not related to measurements (television, computer games and design) multilayer HRDI images are used [8] to improve their visual perception with the transition from standard (SDR) 005–100 cd/m^2 to high (HDR) 0.0005–10000 cd/m^2 dynamic range and vice versa using special transfer functions in accordance with the recommendations of BT.709 [10], BT.1886 [11], BT.2100 [12] of the International Telecommunication Union (ITU). At the same time, traceability is ensured by setting "white", "black", 18 % and 75 % brightness levels adaptable to a standard monitor and standard observation conditions [12]. The sources of metrological traceability of color in measurements are standards (standard samples, reference measuring instruments) and reference measurement techniques that serve to establish reference points of conditional virtual scales in color spaces. The issues that arise when expanding the dynamic range of digital images are as follows: 1) should the measurement results be viewed each time in a new interpretation of the color space, or should the same space be used? 2) is the color space static or a dynamic system? According to the authors, when implementing the measurement the color space should be considered as an open dynamic system taking into account the operations of sampling and quantization from the stand point of a single integrated approach based on tensor calculus. A large number of works are devoted to the development in colorimetry of the concept of a color tensor in relation, however, to the development of an equidistant color space [13]. We are interested in the further development of this topic namely the issues of dynamic range and quantization of spaces that have found application in theoretical physics.

The purpose of this work was to generalize approaches to the description of multidimensional quantized spaces and to show the possibilities of their adaptation to digital colorimetry, which will minimize private and global risks arising in measurements.

The problem of color multivariance and the phenomenon of covariance hypercube

A digital image is an information model "an image more or less similar (but not identical) to the depicted object" [14] described according to ISO/IEC 19794-5 [1] by a two-dimensional representation of the brightness and texture of an object under certain lighting conditions, a discrete-continuous structure consisting of a finite number of elements (pixels) each of which has a geometric reference to the displayed object and its state in time. Color measurement consists in determining the color coordinates in the hardware-dependent *RGB* color space by averaging the intensity values in the red (*R*), green (*G*) and blue (*B*) color channels over the selected

[1] ISO/IEC 19794-5:2011 Information technology – Biometric data interchange formats. Part 5: Face image data

area of the digital image, comparing the obtained values with the built-in scale of virtual measures providing metrological traceability, transforming the obtained values into hardware-independent the space (for example, *XYZ*) and the calculation of the chromaticity coordinates. Each control point on the surface of the object is an equally bright non-point emitter and the pixel area of the digital image corresponding to this control point is considered as a finite set of nominally identical intensity samples in the *R*, *G*, *B* color channels [15]. We understand by metrological traceability the property of the measurement result according to which the result can be correlated with the basis for comparison through a documented unbroken chain of calibrations each of which contributes to the measurement uncertainty. The digital image is the result of convolution of the spectral distribution functions of the elements "illuminator", "illuminated surface", "recording device", "software", "display device" in the color space and an information model of any of them, provided that all other elements are validated [15].

If X_j is an input quantity (spectral distribution function or averaged intensity) the j-th element of the information and measurement channel and x_{kj} is the k-th random variable implementation with uncertainty $u(x_{ki})$, $I = 1, .., m$, then the parameter $u(x_{ki}, x_{lj})$ is the covariance of x_{ki} and x_{lj} as shown in Table.

Table

Validation model of the information and measurement channel

Realization K	Element j					Output param.
	Illuminator X_1	Illuminated surface X_2	Recording device X_3	Software X_4	Display device X_5	
K_1	x_{11} $u^2(x_{11})$	x_{12} $u(x_{12}, x_{21})$	x_{13} $u(x_{13}, x_{31})$	x_{14} $u(x_{14}, x_{41})$	x_{15} $u(x_{15}, x_{51})$	Y_1
K_2	x_{21} $u(x_{21}, x_{12})$	x_{22} $u^2(x_{22})$	x_{23} $u(x_{23}, x_{32})$	x_{24} $u(x_{24}, x_{42})$	x_{25} $u(x_{25}, x_{52})$	Y_2
K_3	x_{31} $u(x_{31}, x_{13})$	x_{32} $u(x_{32}, x_{23})$	x_{33} $u^2(x_{33})$	x_{34} $u(x_{43}, x_{43})$	x_{35} $u(x_{35}, x_{53})$	Y_3
K_4	x_{41} $u(x_{41}, x_{14})$	x_{42} $u(x_{42}, x_{24})$	x_{43} $u(x_{43}, x_{34})$	x_{44} $u^2(x_{44})$	x_{45} $u(x_{45}, x_{54})$	Y_4
K_5	x_{51} $u(x_{51}, x_{15})$	x_{52} $u(x_{52}, x_{25})$	x_{53} $u(x_{53}, x_{35})$	x_{54} $u(x_{54}, x_{45})$	x_{55} $u^2(x_{55})$	Y_5
…						
K_m	x_{m1} $u(x_{m1}, x_{1m})$	x_{m2} $u(x_{m2}, x_{2m})$	x_{m3} $u(x_{m3}, x_{3m})$	x_{m4} $u(x_{m4}, x_{4m})$	x_{m5} $u(x_{m5}, x_{5m})$	Y_m

The elements highlighted with a gray fill are measurement objects. Let's focus on implementations K_1–K_5 (implementations with two or more unknowns that increase information entropy are not considered here). The output parameter Y_k is defined by a set of chromaticity coordinates in a hardware independent space:

$$Y_k = A\begin{pmatrix} r \\ g \\ b \end{pmatrix}, \tag{1}$$

where A is the matrix of transition to the chromaticity coordinates of the hardware independent space; r, g, b are the chromaticity coordinates in space RGB [7]:

$$r=\frac{R}{R+G+B};\quad g=\frac{G}{R+G+B};\quad b=\frac{B}{R+G+B}, \tag{2}$$

where R, G, B are color coordinates determined by averaging the intensities over a region of $M\times N$ pixels in the red, green and blue color channels of a digital image:

$$R=\frac{1}{M\,N}\sum_{i=1}^{M}\sum_{k=1}^{N-1}R_{ik};\quad G=\frac{1}{M\,N}\sum_{i=1}^{M}\sum_{k=1}^{N-1}G_{ik};\quad B=\frac{1}{M\,N}\sum_{i=1}^{M}\sum_{k=1}^{N-1}B_{ik}. \tag{3}$$

In turn, each element of the information-measuring channel, described by the value X_j, can be represented by a set of W variables (aperture, viewing angle, exposure time, illumination, type of quantization, coding, etc.) characterizing the multivariate states of the information-measuring system. Therefore, Table of the model $VM(K_i, X_i, Y_i)$ can be represented as a family of covariance matrices.

According to ISO/IECGuide 98-3/Suppl 2:2011[2] the covariance matrix is a positively semidefinite matrix of dimension $N\times N$, where N is the number of input quantities, on the main diagonal of which there are squares of standard uncertainties corresponding to the estimates of the magnitude, and the remaining members of the matrix represent covariances between pairs of corresponding estimates of the elements of the magnitude:

$$u(x_{ji},x_{kl})=\frac{1}{m-1}\sum\sum_{x\in C}(x_{ji}-\mu_1)(x_{kl}-\mu_2), \tag{4}$$

where μ_1, μ_2 are mathematical expectations by signs; C is multiple points in a class.

So for each j-th implementation, the dimension of the matrix will be 5×5. To implement K_1, the matrix has the form:

$$u_1(X_1,..X_5)=\begin{pmatrix} u^2(x_{11}) & u(x_{11},x_{12}) & u(x_{11},x_{13}) & u(x_{11},x_{14}) & u(x_{11},x_{15}) \\ u(x_{12},x_{11}) & u^2(x_{12}) & u(x_{12},x_{13}) & u(x_{12},x_{14}) & u(x_{12},x_{15}) \\ u(x_{13},x_{11}) & u(x_{13},x_{12}) & u^2(x_{13}) & u(x_{13},x_{14}) & u(x_{13},x_{15}) \\ u(x_{14},x_{11}) & u(x_{14},x_{12}) & u(x_{14},x_{13}) & u^2(x_{14}) & u(x_{14},x_{15}) \\ u(x_{15},x_{11}) & u(x_{15},x_{12}) & u(x_{15},x_{13}) & u(x_{15},x_{14}) & u^2(x_{15}) \end{pmatrix}. \tag{5}$$

The abbreviated form of writing this matrix:

$$u_{1ij}=\begin{cases} u^2(x_{1j}) & i=j \\ u(x_{1i},x_{1j}) & i\neq j \end{cases}, \tag{6}$$

where $u^2(x_{ij})$ is variance of the estimate x_{ij}; $u(x_{ij}, x_{mh})$ is covariance between values x_{ij} and x_{mh}.

Similarly, we write for implementations K_2–K_5. The uncertainty $u(Y_1)$ is calculated from the expression:

$$u(Y_i)=Cu(X_i)C^T, \tag{7}$$

where C is matrix of sensitivity coefficients with dimension $N\times N$.

The sensitivity coefficients can be defined as partial derivatives of the original function f connecting the variables $X_1, X_2, \ldots, X_5$ [15]:

$$C_j=\left(\frac{\partial f}{\partial x_j}\right). \tag{8}$$

For the case of the triad X_1, X_2, X_3 the covariance cube of the information and measurement system is shown in Figure 1 on the faces of which the matrix elements are located. There are only six triads as six faces of this cube can be displayed. In this case, the covariance cube contains $3\times(m\times m)$ elements.

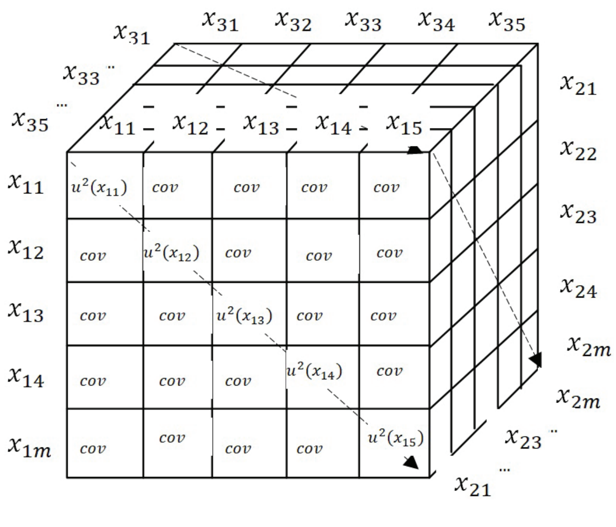

Figure 1 – Covariance cube of the information and measurement system $VM(K_i, X_1, X_2, X_3, Y_i)$, $i = 1, \ldots, m$

[2] ISO/IECGuide 98-3/Suppl 2:2011 Uncertainty of measurement. Part 3: Guide to the expression of uncertainty in measurement (GUM:1995). Supplement 2: Extension to any number of output quantities

Considering that the covariance cube generally contains jWm^2 elements (where j is the number of variables X_j, and m is the number of implementations K_i), it can be further considered a covariance hypercube of the information and measurement channel.

Transition to orthogonal matrices of high dimensions

The problem of color multivariance in digital colorimetry is solved with the help of orthogonal matrices of high dimensions that allow displaying the states of the information and measurement channel in a multidimensional space. The graphical representation of a hypercube through 5-matrices with fixed (a, b, c) and sliding (α, β, γ) indices in the form of a set of 3-matrices of n-dimensions can be represented compactly in the interpretation of Penrose diagrams [16, 17], as illustrated in Figure 2.

This diagram is an image of multilinear functions or tensors and represents several shapes connected by lines. Each element of the original matrix is multiplied by the corresponding element of the convolution matrix. By the derivative f_x of the image f we will understand:

$$f_x(i,j) = \left.\frac{\partial f(x,y)}{\partial x}\right|_{\substack{x=x_i \\ y=y_j}} = f_{i,j} - f_{i-1,j}. \qquad (9)$$

Under the convolution matrix, we will understand the matrix of coefficients which is “multiplied” by the values of the pixel intensities of the image to obtain the desired result. An example of such matrices used to detect lines in [18] is shown in Figure 3.

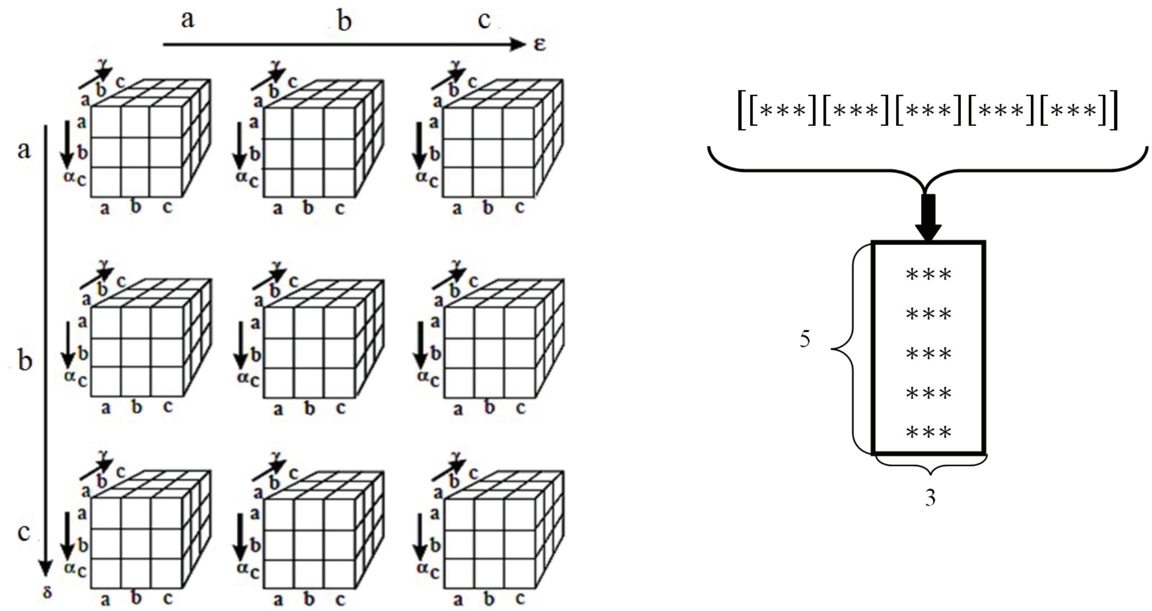

a *b*

Figure 2 – Representation of the 5-matrix *A*aßγδε in the form of a set of matrices: *a* – based on the Crohn’s methodology; *b* – in the form of Penrose diagrams

-1	-1	-1
2	2	2
-1	-1	-1

-1	-1	2
-1	2	-1
2	-1	-1

-1	2	-1
-1	2	-1
-1	2	-1

2	-1	-1
-1	2	-1
-1	-1	2

Figure 3 – Example of convolution matrices

Then the total sum of these products is found, which, if necessary, is divided by the normalization coefficient (the sum of the elements of the convolution matrix). This is necessary in order for the average intensity to remain unchanged. Then the brightness value of the current pixel can be set by the formula:

$$L_{ij} = \sum_{i=1}^{n\times m} w_i z_i, \tag{10}$$

where z_i is the brightness value of the pixel corresponding to the mask coefficient w_i.

For example a command in *Wolfram Mathematica* system, that displays the original image of the motherboard as well as its modified images, as shown in Figure 4 is written according to the developed program [19] as follows: {*f*,*ImageConvolve*[*f*,*maska1*]//*ColorNegate*, *ImageConvolve*[*f*,*maska2*]//*ColorNegate*,*ImageConvolve*[*f*,*maska4*]//*ColorNegate*}.

The figure demonstrates the reduction of degrees of freedom due to the use of convolution matrices during the transition from full-color to halftone and binary images. The most commonly used filter based on convolution matrices is the Gaussian filter (the matrix is filled according to the normal law). In this case, the elements of the matrix are normalized. An example of such a matrix is shown in Figure 5.

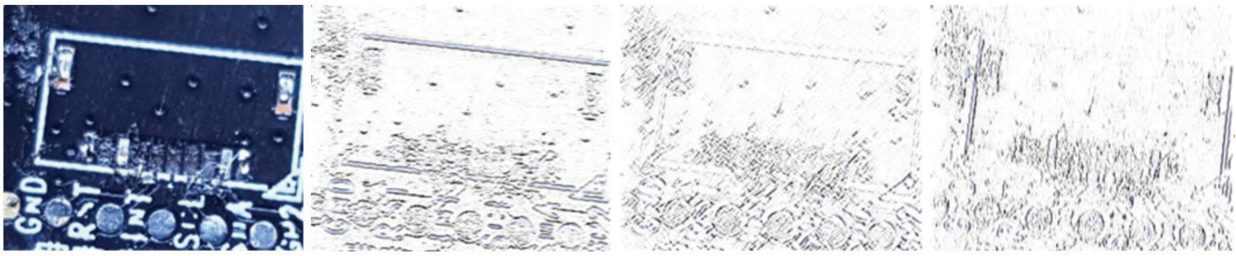

Figure 4 – Line detection on the motherboard snapshot

0.00987648	0.0796275	0.00987648
0.0896275	0.641984	0.0796275
0.00987648	0.0796275	0.00987648

Figure 5 – Convolution matrix

Matrix elements can be defined using the built-in function GaussianMatrix in the *Wolfram Mathematica* system.

Color tensors in spaces of directed fields

Taking into account the recording of orthonomized matrices distributed according to the normal law for some image f the structural tensor takes the form (subscripts denote spatial derivatives and the dash indicates convolution with a Gaussian filter) [19]:

$$G = \begin{pmatrix} \overline{f_x^2} & \overline{f_x f_y} \\ \overline{f_x f_y} & \overline{f_y^2} \end{pmatrix}. \tag{11}$$

The tensor describes the local differentiated structure of the image and is suitable for finding edges and corners. The original image has the form:

$$f = \begin{pmatrix} R \\ G \\ B \end{pmatrix}. \tag{12}$$

If the structural tensor G is considered a color tensor, then for the RGB color space it can be written as:

$$G = \begin{pmatrix} \overline{R_x^2 + G_x^2 + B_x^2} & \overline{R_x R_y + G_x G_y + B_x B_y} \\ \overline{R_x R_y + G_x G_y + B_x B_y} & \overline{R_y^2 + G_y^2 + B_y^2} \end{pmatrix}. \tag{13}$$

If a color tensor describes a two-dimensional structure at a certain point in the image then its own value can be determined for it by the formula [13, 20] (the superscript T denotes the transpose operation):

$$\lambda_1 = 0,5(\overline{f_x^T f_x}\ \overline{f_y^T f_y} + \sqrt{(\overline{f_x^T f_x} - \overline{f_y^T f_y})^2 + (2\overline{f_x^T f_y})^2}). \tag{14}$$

The parallel operation of determining the intensities of a digital image using a structural color tensor in the color channels R, G, B is carried out using the commands *ImageHistogram*[*f*, *Apperance->"Separated"*], as shown in the Figure 6 [18].

The eigenvalue indicates the local orientation on the image with the maximum color change. The elements of the tensor G are invariant when the spatial axes rotate and move. This representation is applicable for classifying the color in the image taking into account situations when the color change is caused by a shadow or darkening of the image the influence of the presence of glare.

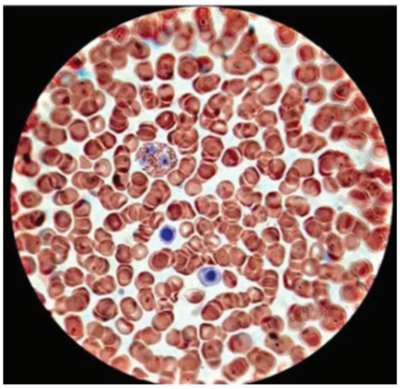

a

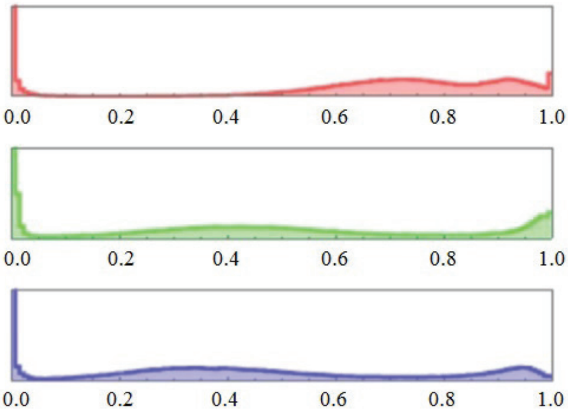

b

Figure 6 – The result of using a structural tensor: *a* – digital image of a blood sample obtained using a microscope; *b* – *RGB*-image histograms

The second-rank color tensor is described in [13] and is used to construct Macadam balls describing the *XYZ* color space as a "single-cavity hyperboloid in four-dimensional spacetime having the form" [13]:

$$R_{ab} - \frac{R}{2} g_{ab} = 0, \tag{15}$$

where R_{ab} is the Ricci curvature tensor obtained from the R_{abcd} space-time curvature tensor by convolving it by a pair of indices; R is scalar curvature that is, the collapsed Ricci tensor; g_{ab} is metric tensor.

Then you can map a certain color vector to any point on the color locus. "Since all vectors of type 0*S* start from the zero point, the length of these vectors (color saturation) is determined by a simple expression of the type" [13]:

$$D = \sqrt{x^2 + y^2 + L^2}, \tag{16}$$

where x, y is coordinates of the end of the vector in the coordinate system x' y'; L is brightness of the end point of the vector.

The divalent symmetric color tensor G_{ab} can be expressed by decomposing the color vector g_i by the orts of the basis e_1, e_2, e_3 [20]:

$$G_{ab} = \begin{pmatrix} H & 0 & 0 \\ 0 & S & 0 \\ 0 & 0 & L \end{pmatrix} = \\ = \begin{pmatrix} arctg(x/y) & 0 & 0 \\ 0 & \sqrt{x^2+y^2+L^2} \,/\, \sqrt{x_a{}^2 + y_a{}^2 + L_a{}^2} & 0 \\ 0 & 0 & L \end{pmatrix}, \tag{17}$$

where H is color tone; S is saturation.

The essence of this tensor is to set the coordinates for the metric tensor at a specific point on the color diagram [13]. Moving from the single-cavity hyperboloid shown in Figure 7 to the standard color body of the *XYZ* space, we will deal with tensors of higher orders.

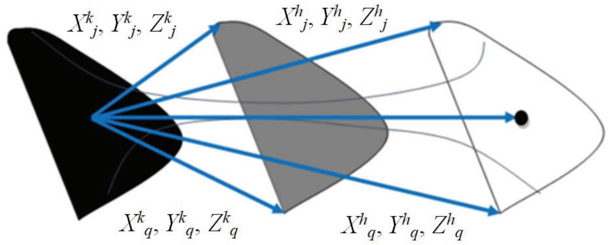

Figure 7 – Representation of the *XYZ* color space as a one-band hyperboloid with decomposition into families of vectors

Tensors come out of the zero point, intersect the plane of the locus and can be combined into families of vectors $X^k{}_0Y^k{}_0Z^k$, $X^k{}_jY^k{}_jZ^k$, $X^h{}_jY^h{}_jZ^h{}_j$, $X^k{}_qY^k{}_qZ^k{}_q$, $X^h{}_qY^h{}_qZ^h{}_q$. They form directed fields by zoning the color body of the *XYZ* space [21] satisfying the expressions for calculating the chromaticity coordinates at the color locus [3]:

$$x = \frac{X}{X+Y+Z}; \quad y = \frac{Y}{X+Y+Z}; \quad z = \frac{Z}{X+Y+Z}. \tag{18}$$

The standardized palette (as an example, the palette shown in Figure 8*a*) is divided into six spatial sectors according to the principle of predominance of *R* (red), *G* (green) and *B* (blue) components (I – *RGB*; II – *RBG*; III – *GBR*; IV – *GRB*; V – *BRG*; VI – *BGR*) and transformed into the coordinates of the *XYZ* space, whose chromaticity coordinates at the color locus represent the intersection points of the color tensors (Figure 8*b*) [21].

Devices and Methods of Measurements
2022, vol. 13, no. 3, pp. 216–227
Y. Saukova, M. Hundzina

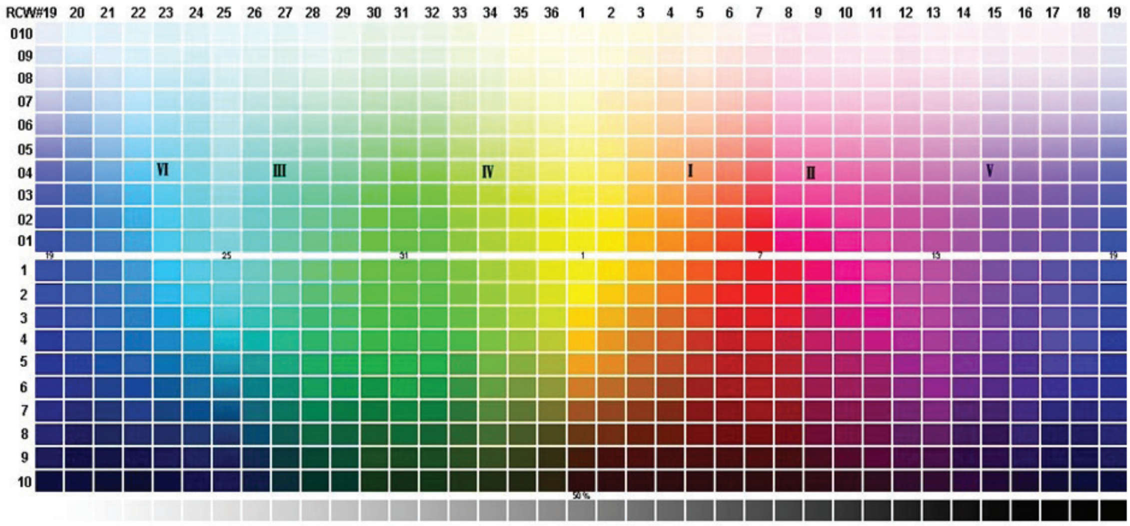

a

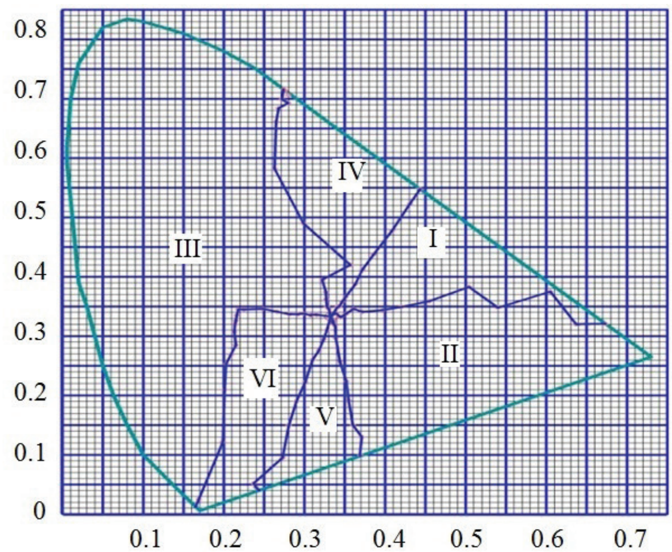

b

Figure 8 – Zoning of the *XYZ* color space: *a* – standardized computer palette; *b* – a color locus divided into sectors

Tensor indexing and singular value decomposition methodology [21] makes it possible to build low-rank approximations of matrices that require less space in computer memory and less computing resources to work with them.

Tensor calculus in discrete-quantized space

Multiple registration of a static object with incrementally increasing exposure time allows to determine the $R_jG_jB_j$ color coordinates for each implementation, combine them into vector families ($R^T{}_jG^T{}_jB^T{}_j$ tensor), transform them into $X_jY_jZ_j$ vector families ($X^T{}_jY^T{}_jZ^T{}_j$ tensor) moving from the zero point to the plane of the color locus, expanding the dynamic range without losing metrological traceability. From the point of view of general relativity, such a displacement can be considered as a parallel transfer of some vector [23] $A^i{}_0$ from the starting point P_0 with coordinates $x^i{}_0 = x^i(\mu_0)$ along the curve $x^j = x^j(\mu)$ to the point P_1 with coordinates $x^i{}_1 = x^i(\mu_1)$, $(\mu_0 \le \mu \le \mu_1)$ which connected to each other. The unique (according to Cauchy's theorem) vector $A^i{}_1 = A^i(\mu_1)$ is the result of parallel transfer and characterizes the value of the field $A^i(x(\mu))$ at the point of μ_1. The vectorgetsincremented [22]:

$$\delta A^i = -\Gamma^i_{kj} \frac{dx^j}{d\mu} \delta x^j, \tag{19}$$

where δx^j is infinitesimal vector to which the transfer is carried out; Γ^i_{kj} is the coefficient of connectivity characterizing the degree of curvature of space.

The dynamics of open quantum systems in the language of tensor networks is described through Hamiltonians and the quantum reservoir model as a set of non-interacting quantum oscillators [22] whose dimension is greater than the dimension of the system. The quantum diagram of the dynamics of the system and the reservoir (upper and lower channels, respectively) [22] is shown in Figure 9.

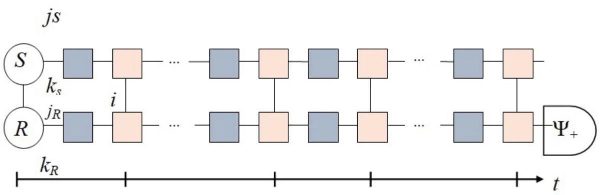

Figure 9 – Diagram representation of color space samplingin the form of a time tensor network

Connections *i* between two channels (system and reservoir) illustrate the correlation between reference points – physically implemented traceability sources j_s (standard samples) and their j_s images at certain points in time. The Hamiltonian of the complete system is generally given by the expression [22]:

$$H = H_0 + H_{\text{int}}, \tag{20}$$

where

$$H_0 = H_s \otimes I + I \otimes H_R; \tag{21}$$

$$H_{\text{int}} = \gamma \sum_{i=1}^{n} A_i \otimes B_i, \tag{22}$$

where H_s and H_R are hilbert spaces of the system and its reservoir, respectively; I is information; H_{int} is mutual information entropy between spaces; γ is characteristic constant of interaction between the reservoir and the system.

The dynamics of the complete system in the form of the Trotter expansion has the next form [22]:

$$|\rho(t)\rangle = \Phi_0(\tau)\Phi_{\text{int}}(\tau)...\Phi_0(\tau)\Phi_{\text{int}}(\tau)\,|\rho(t)\rangle + \mathrm{O}(\gamma\tau), \tag{23}$$

where $\Phi_0(\tau)$ is dynamic mapping responsible for free dynamics over time τ;

$$\Phi_0(\tau) = \exp(-i\tau H_s) \otimes \exp(i\tau H_s{}^T) \otimes \exp(-i\tau H_R) \otimes \exp(i\tau H_R{}^T), \tag{24}$$

$\Phi_{\text{int}}(\tau)$ is a dynamic map that is responsible for the dynamics only involving the interaction Hamiltonian over time τ. Parameter $\mathrm{O}(\gamma\tau)$ specifies the accuracy of the temporal tensor network with the sampling step τ. The time discreteness is given as $N = t/\tau$.

The process of color space quantization is conveniently viewed in terms of the depth of the reservoir's memory. Assuming that the initial state of the reservoir does not depend on the initial states of the system, we write an expression for the brightness levels B [22]:

$$\langle B_i(t+\delta t) B_j(t) \rangle = \frac{\dfrac{t}{\tau-1}...i, \dfrac{\delta t}{\tau-1}....j}{-\gamma\tau}. \tag{25}$$

The vector increment δt is the nominal quantization step. In terms of the memory depth T of the effective reservoir R, the mutual information between two quantum systems will be [22]:

$$I(L;R) = S(M_{L,R} \,\|\, M_L \otimes M_R) \sim \exp(-\frac{(p-q)\tau}{T}), \tag{26}$$

where M is arbitrary density reservoir temporary network matrix with a set of not necessarily orthogonal vectors $\{V_q\}_q$, represented in the form [22]:

$$M = \sum V_q V_q^+. \tag{27}$$

To select a sufficient dimension of the effective reservoir, the criteria of entanglement entropy, Rényi, and von Neumann are used in [22]. Renyi entropy is calculated by the formula $0 < \alpha < 1$ [22]:

$$S(M) = \frac{1}{1-\alpha} \ln TrM^{\alpha}. \tag{28}$$

The relative entropy is zero if and only if. For the von Neumann entropy [22]:

$$d \approx \exp(2n\gamma T(1 - \ln \gamma\tau)). \tag{29}$$

Note that the contributions to the time evolution of the system from its previous states decrease exponentially as the time interval between the current and previous states of the system increases. The characteristic time interval in which the previous states of the system make a significant contribution is equal to the depth of the reservoir memory T, i. e. bits per channel [22].

Conclusion

Since digital colorimetry is based on the transformation of color spaces, their discretization, quantization, encoding and decoding, it is proposed to use the apparatus of tensor calculus to solve the problems of ensuring metrological traceability and reliability.

The presented validation model shows the multivariance of the states of the information-measuring channel through the phenomenon of the covariance hypercube. Only implementations with one unknown make it possible to perform measurements. The transition to orthogonal matrices of high dimensions leads to redundancy of information when identifying the states of the information-measuring system and its elements.

The proposed approach is based on the ranking of intensities in color channels and the division of color spaces into areas of directional fields, which makes it possible to reduce the uncertainty of color measurement. Parallel transfer of vectors with subsequent indexing of color tensors makes it possible to expand the dynamic range of digital image intensity.

A promising area of application of tensor calculus in digital colorimetry is the solution of inverse problems associated with the modeling of information and measurement systems, the creation of virtual objects, and exploratory studies of traceability under high uncertainty.

References

1. Fershil'd M.D. *Modeli cvetovogo vospriyatiya* [Color perception models]. Moscow, Tekhnosfera Publ., 2005, 416 p.

2. Kuznecov U.V. [Color Management Systems: Concept and Opportunity]. *Poligrafiya* [Polygraphy], 2005, no. 4, pp.14–17 (in Russian).

3. Schanda J. Colorimetry: Understanding the CIE system. New York, A John Wiley & SONS Publ., 2007, 467 p.

4. Fan Y., Li J., Guo Y., Xie L., Zhang G. Digital image colorimetry on smartphone for chemical analysis. *Measurement*, 2021, vol. 171, p. 108829.
DOI: 10.1016/j.measurement.2020.108829

5. Bure V.M., Mitrofanova O.A. Analysis of aerial photographs to predict the spatial distribution of ecological data. *Contemporary Engineering Sciences*, 2017, vol. 10, no. 4, pp. 157–163 (in Russian).
DOI: 10.12988/ces.2017.611175

6. Mitrofanov E.P., Petrushin A.F., Mitrofanova O.A. [Using aerial photography data to substantiate precision agricultural practices for the use of agrochemicals]. *Vtoraya vserossijskaya nauchnaya konferenciya s mezhdunarodnym uchastiem* "*Primenenie sredstv distancionnogo zondirovaniya zemli v sel'skom hozyajstve*" [Second all-russian scientific conference with international participation "Application of earth remote sensing in agriculture"]. St. Petersburg, September 26–28, 2018, pp. 212–217 (in Russian).

7. Goden ZH. *Kolorimetriya pri videoobrabotke* [Colorimetry in video processing]. Moscow, Tekhnosfera Publ., 2008, 328 p.

8. *ICCExperts' Dayon HDR ColourImaging*. [Electronic Resource]. Available at: https://www.color.org (accessed: 15.03.2022).

9. *Parameter values for the HDTV standards for production and international programme exchange*. [Electronic Resource]. Available at: https://www.itu.int/rec/R-REC-11 (accessed: 01.02.2022).

10. *Reference electro-optical transfer function for flat panel displays used in HDTV studio production*. [Electronic Resource]. Available at: https://www.itu.int/rec/R-REC-BT.1886 (accessed: 01.02.2022).

11. *Image parameter values for high dynamic range television for use in production and international programme exchange*. [Electronic Resource]. Available at: https://www.itu.int/rec/R-REC-BT.2100 (accessed: 01.02.2022).

12. *High dynamic range television for production and international programme exchange*. [Electronic Resource]. Available at: https://www.itu.int/pub/R-REP-BT.2390 (accessed: 01.03.2022).

13. Lozhkin L.D., Voronoj A.A., Soldatov A.A. Converting CIE color space to strictly equal contrast based on tensor calculus. *Fizika volnovyh processov i radiotekhnicheskie sistemy* [Physics of wave processes and radio engineering systems], 2016, vol. 19, no. 4, pp. 50–59 (in Russian).

14. Makarov D.G. Digital processing of television measuring signals. *Cifrovaya obrabotka signalov* [Digital signal processing], 2007, no. 3, pp. 30–36 (in Russian).

15. Saukova Y. The Validation Model of Information Measuring Channel in Technical Vision Systems. *International Journal of Advanced Engineering and Technology*, 2018, vol. 1, no. 4, pp. 28–33.

16. *Elementy tenzornogo analiza G. Krona* [Elements of tensor analysis G. Krohn]. [Electronic Resource]. Available at: http://устойчивоеразвитие.рф/index.php?id=91 (accessed: 01.02.2022).

17. Luchnikov I., Vintskevich S., Ouerdane H., Filippov S. Simulation complexity of open quantum dynamics: Connection with tensor networks. *Physical Review Letters*, 2019, vol. 122, no. 16, p. 160401.
DOI: 10.1103/PhysRevLett.122.160401

18. Hundzina M.A. An overview of Wolfram Mathematica functions that implement image segmentation. *Mekhanika ta matematichni metodi* [Mechanics and mathematical methods]. Odessa, 2020, pp. 78–89.

19. Van de Weijer J., Robust J., Gevers T., Smeulders A.W.M. Photometric Invariant Features from the Color Tensor. *IEEE Transactions on Image Processing*,

2006, vol. 15, iss. 1, pp. 118–127.
DOI: 10.1109/TIP.2005.860343

20. Lozhkin L.D., Neganov V.A. *Cvet, ego izmerenie, vosproizvedenie i vospriyatie v televidenii. CHast' I* [Color, its measurement, reproduction and perception in television. Part I]. Samara, IUNL PGUTI Publ., 2013, 286 p.

21. Saukova Y., Matyush I. The Metrological Assurance of the Colorimetry in Software and Hardware Environments. *International Journal of Innovative Research in Electronics and Communications (IJIREC)*, 2016, vol. 3, no. 5, pp. 6–19. **DOI:** 10.20431/2349-4050.0305002

22. Alekseev S.O., Pamyatnyh E.A., Ursulov A.V., Tret'yakova D.A., Rannu K.A. *Vvedenie v obshchuyu teoriyu otnositel'nosti, ee sovremennoe razvitie i prilozheniya* [Introduction to General Relativity, Its Modern Development and Applications]. Ekaterinburg: Izd-vo Ural. Un-t, 2015, 380 p.

Неразрушающий контроль качества термообработки стальных образцов, полученных аддитивной технологией, магнитошумовым методом

В.Н. Бусько, А.П. Крень, Г.А. Ланцман

*Институт прикладной физики Национальной академии наук Беларуси,
ул. Академическая, 16, г. Минск 220072, Беларусь*

Поступила 11.07.2022
Принята к печати 27.09.2022

Производство изделий по аддитивным технологиям, как правило, сопровождается несанкционированным появлением и ростом неоднородности свойств, анизотропии, остаточных напряжений, пористости и других дефектов. Поэтому резко возросла актуальность неразрушающего контроля качества изделий, полученных с помощью аддитивных технологий. Цель работы – экспериментально исследовать возможность контроля и оценки качества термической обработки трёхмерных и литых образцов с помощью неразрушающих методов контроля.

Исследовались стальные образцы из низколегированной стали 09Г2С, полученные методом селективного лазерного сплавления с разными видами и режимами последующих термических обработок и литьём. Методами исследования являлись магнитошумовой метод, реализующий магнитный метод эффекта Баркгаузена, и контактно-динамический метод измерения твёрдости материала.

Экспериментально установлено, что оба метода обладают высокой чувствительностью к отожжённым и нормализованным трёхмерным образцам и их отбраковке. Магнитошумовой метод, в отличие от метода твёрдометрии, связанного, преимущественно, с фазово-структурными изменениями, благодаря селективности к другим контролируемым параметрам, дополнительно обладает чувствительностью к литьевым образцам, хотя микроструктуры литых и нормализованных трёхмерных образцов по данным рентгеноструктурного анализа близки между собой.

Магнитошумовой метод может быть использован в качестве одного из физических методов оценки качества и контроля термообработки 3D-образцов на стадии изготовления при отработке их видов, режимов и разбраковке образцов.

Ключевые слова: аддитивные технологии и материалы, селективное лазерное сплавление, термическая обработка, магнитошумовой метод, контактно-динамический метод.

DOI: 10.21122/2220-9506-2022-13-3-228-236

Адрес для переписки:
Бусько В.Н.
*Ин-т прикладной физики Национальной академии наук Беларуси,
ул. Академическая, 16, г. Минск 220072, Беларусь
e-mail: busko@iaph.bas-net.by*

Address for correspondence:
Busko V.N.
*Institute of Applied Physics of the National Academy of Science of Belarus,
Akademicheskaya str., 16, Minsk 220072, Belarus
e-mail: busko@iaph.bas-net.by*

Для цитирования:
В.Н. Бусько, А.П. Крень, Г.А. Ланцман.
Неразрушающий контроль качества термообработки стальных образцов, полученных аддитивной технологией, магнитошумовым методом.
Приборы и методы измерений.
2022. – Т. 13, № 3. – С. 228–236.
DOI: 10.21122/2220-9506-2022-13-3-228-236

For citation:
V.N. Busko, A.P. Kren, G.A. Lanzman.
[Non-Destructive Testing by Magnetic Noise Method of the Quality of Heat Treatment of Steel Samples Obtained by Additive Technology].
Devices and Methods of Measurements.
2022, vol. 13, no. 3, pp. 228–236 (in Russian).
DOI: 10.21122/2220-9506-2022-13-3-228-236

Non-Destructive Testing by Magnetic Noise Method of the Quality of Heat Treatment of Steel Samples Obtained by Additive Technology

V.N. Busko, A.P. Kren, G.A. Lanzman

Institute of Applied Physics of the National Academy of Science of Belarus,
Akademicheskaya str., 16, Minsk 220072, Belarus

Received 11.07.2022
Accepted for publication 27.09.2022

Abstract

The manufacture of products using additive technologies is accompanied by the unpredictable appearance of inhomogeneity of properties, anisotropy, residual stresses, porosity, and other defects. Therefore, there is a great relevance of non-destructive quality control of products obtained by additive technologies. The purpose of the paper is the experimental investigation of the possibility of testing and evaluation of the quality of heat treatment of three-dimensional and cast samples by non-destructive control methods.

The low-alloy steel 09G2S samples, which was obtained by casting and selective laser sintering different modes of subsequent heat treatments were studied. The method of the Barkhausen effect and the instrumented indentation method for measuring the material hardness were applied.

It was experimentally established that both methods are highly sensitive to annealed and normalized three-dimensional samples and their rejection. Compared to the hardness measurement method, which is mainly associated with phase-structural changes, the magnetic noise method due to selectivity to other controlled parameters is additionally sensitive to cast samples (at the same time the microstructures of cast and normalized three-dimensional samples are close to each other according to X-ray data).

The magnetic noise method can be used as one of the physical methods for evaluation the quality and control of the heat treatment of 3D samples at the manufacturing stage when testing their types and modes, as well as sorting samples.

Keywords: additive technologies and materials, selective laser melting, heat treatment, magnetic noise method, contact-dynamic method.

DOI: 10.21122/2220-9506-2022-13-3-228-236

Адрес для переписки:
Бусько В.Н.
Ин-т прикладной физики Национальной академии наук Беларуси,
ул. Академическая, 16, г. Минск 220072, Беларусь
e-mail: busko@iaph.bas-net.by

Address for correspondence:
Busko V.N.
Institute of Applied Physics of the National Academy of Science of Belarus,
Akademicheskaya str., 16, Minsk 220072, Belarus
e-mail: busko@iaph.bas-net.by

Для цитирования:
В.Н. Бусько, А.П. Крень, Г.А. Ланцман.
Неразрушающий контроль качества термообработки стальных образцов, полученных аддитивной технологией, магнитошумовым методом.
Приборы и методы измерений.
2022. – Т. 13, № 3. – С. 228–236.
DOI: 10.21122/2220-9506-2022-13-3-228-236

For citation:
V.N. Busko, A.P. Kren, G.A. Lanzman.
[Non-Destructive Testing by Magnetic Noise Method of the Quality of Heat Treatment of Steel Samples Obtained by Additive Technology].
Devices and Methods of Measurements.
2022, vol. 13, no. 3, pp. 228–236 (in Russian).
DOI: 10.21122/2220-9506-2022-13-3-228-236

Введение

Производство материалов и изделий с помощью аддитивных технологий (АТ) относится к наиболее перспективным производственным процессам, сущность которых состоит в получении готовых изделий/деталей способом последовательного послойного построения путём фиксации отдельных слоёв порошкового материала и их последовательного соединения между собой с помощью сплавления, спекания или другим способом в зависимости от выбора технологии [1]. Формирование изделия путём «наращивания» материала слой за слоем позволяет резко ускорить полный цикл производства, начиная от проектирования до изготовления с высокой точностью и скоростью получения конечного продукта с помощью компьютерной трёхмерной печати и 3D-принтера. Это послужило тому, что в ряде отраслей промышленности (машиностроение, авиа- и ракетостроение, строительство, медицина и др.) резко растёт объём внедряемых 3D–изделий за счёт постепенной замены изготовленных традиционными способами (прокат, литьё, штамповка, ковка, точение, фрезерование и др.). В итоге комплекс перечисленных достоинств техпроцесса с применением АТ приводит к экономии материальных, трудовых и временных ресурсов [1–3].

Специфика получения металлических изделий с использованием АТ такова, что после изготовления они могут иметь более ярко выраженные неоднородность, шероховатость, анизотропию, остаточные напряжения, сложную микроструктуру, текстуру, дефекты (микротрещины, поры, включения, несплошности, несплавления) [4–6], на которые дополнительно влияют виды и режимы последующих термических, механических, термомеханических и других видов обработок, изменяющих структуру и физико-механические свойства (ФМС), которые одновременно являются сдерживающими факторами при внедрении. Вследствие этого в материалах и изделиях, полученных с помощью АТ, в процессе и после изготовления необходимо проводить неразрушающий контроль (НК) и мониторинг качества.

Таким образом, учитывая, что изготовление материалов с применением АТ сопряжено с наличием целого ряда особенностей [4–6], обусловленных отличным от традиционных способов их получения, более остро встаёт вопрос обеспечения качества на основе применения различных физических методов неразрушающего контроля (НК), тем более, что любой цикл аддитивного производства должен включать в себя текущий и выходной контроль качества.

В [5, 7] отмечены две главные задачи, стоящие перед НК качества изделий, полученных по АТ (АТ-изделий): выявление и идентификация дефектов, возникающих при синтезе изделий, т. е., контроль качества изделий в соответствии с требованиями нормативов и выявление дефектов при отработке режимов изготовления. Для этого предложено использовать ультразвуковые, вихретоковые, рентгеновские, капиллярные и магнитные методы, к которым относится магнитошумовой метод, реализующий магнитный эффект Баркгаузена (МЭБ)[1]. В [8] исследованы возможности НК качества АТ-изделий с помощью ультразвукового метода контроля; в результате установлена выявляемость поверхностных трещиноподобных дефектов. В [9, 10] приведены результаты оценки пористости, качества поверхности и внутренней структуры с помощью рентгеновских, акустических, радиографических и других методов, большинство из которых имеют те или иные ограничения и сделан вывод о необходимости привлечения новых или комбинированных методов и технологий НК качества АТ-изделий.

В настоящее время практически отсутствует системный анализ экспериментальных данных по результатам НК качества, видов и режимов термообработки разными физическими методами. В [11] указано, что для снижения упругих напряжений в трёхмерных материалах «режимы и виды термообработки необходимо подбирать индивидуально для каждой марки стали». Но в [7] отмечается, что в целом вопрос НК качества АТ-материалов до конца не отработан.

Цель работы – исследовать возможность оценки качества термической обработки образцов низколегированной стали 09Г2С, полученных литьём и методом селективного лазерного сплавления (СЛС), магнитошумовым методом.

---

[1] ГОСТ 18353-79. Контроль неразрушающий (классификация видов и методов), 26 с..

Образцы, методы и методика исследований

Исследовались две партии образцов: первая – 4 образца длиной 150 мм, шириной 15 и 30 мм (в средней и галтельной части), толщиной 2 мм и 10 мм, полученные методом СЛС, и 2 образца таких же размеров – литьём; вторая партия – 2 образца получены методом СЛС и 1 образец – литьём, размеры – те же, толщина 2 мм. Исходный компонент – порошок малоуглеродистой стали 09Г2С с размером фракций 10–45 мкм. Технические характеристики 3D–принтера, с помощью которого получены образцы иного размера: мощность лазера и диаметр пятна – приведены в работе [11]. После изготовления трёхмерных образцов одна их часть подвергалась рекристаллизационному низкотемпературному отжигу, вторая – нормализации с охлаждением на воздухе. Обе поверхности образцов подвергались механической обработке (шлифовке) вдоль оси абразивным камнем с малой подачей и водяным охлаждением (шероховатость составляла 5–8 мкм).

На рисунке 1*a*, *b* представлен внешний вид образцов первой партии толщиной 2 и 10 мм и второй – толщиной 2 мм, отличающихся тем, что вторая получена разрезанием на электроэрозионном станке образцов толщиной 10 мм на образцы толщиной по 2 мм с последующей поверхностной механической обработкой (все образцы для исследований предоставлены Институтом физики металлов Уральского отделения Российской академии наук, г. Екатеринбург).

В таблице приведены режимы термической обработки и другие характеристики исследуемых образцов.

В качестве метода оценки качества термообработки АТ-образцов после СЛС использовался реализующий МЭБ микромагнитный метод, информативные параметры которого, благодаря тесной связи с «тонкой» структурой ферромагнетика, являются интегральными и обладают высокой чувствительностью к различным контролируемым параметрам, включая микро- и макроструктуру, неоднородность, шероховатость, анизотропию, дефектность, напряжённо-деформированное состояние, поверхностную и объёмную обработку и др. [12–18]. Измерения интенсивности $U_{эф}$ магнитного шума (МШ) выполнялись с помощью прибора ИМШ [18]

В качестве второго сравнительного метода оценки качества термообработки литых и 3D-образцов использовался метод динамического индентирования для оценки твёрдости. Для её измерения использовался цифровой динамический твердомер типа ТПЦ-7 [19, 20]. Динамическое индентирование относится к методам НК благодаря тому, что при измерениях твёрдости поверхность образца практически не повреждается (глубина отпечатка менее 25 мкм).

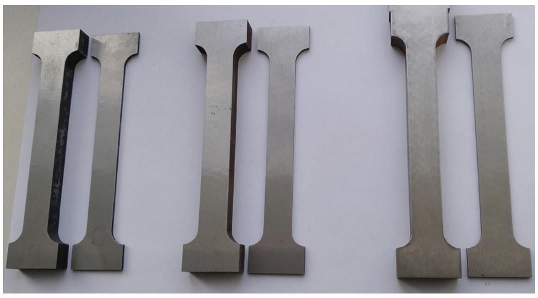

a

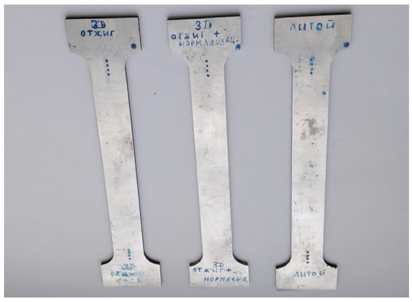

b

Рисунок 1 – Исследуемые образцы стали 09Г2С, полученные методом селективного лазерного сплавления и литья: *a* – 1-я партия; *b* – 2-я партия

Figure 1 – Studied samples of steel 09G2S obtained by selective laser melting and casting: *a* – 1st batch; *b* – 2nd batch

Таблица/Table

Характеристики образцов материалов порошковой стали 09Г2С, полученных методом селективного лазерного сплавления и литьём

Characteristics of samples of powder steel 09G2S obtained by selective laser alloying and casting

№ образца (партии) Sample No. (batch)	Способ изготовл. Production method	Режим термической обработки Thermal treatment mode	Ср. толщ., мм Average thickness, mm	Вес*, г Weight*, g	Уд. пл.**г/см^3 Specific gravity** g/cm^3
1 (1 п.) 1 (1st batch)	3D (СЛС) 3D (SLS)	Отжиг 350 °С, 3 часа (1ч. + 2ч.) Annealing 350 °C, 3 hours (1h + 2h)	2.02	39.584	Не определ. Undefined
2 (-//-)	3D (СЛС) 3D (SLS)	-//-	10.9	216.507	-//-
3 (-//-)	3D (СЛС) 3D (SLS)	Отжиг 350 °С, 3 ч. + нормализация 980 °С, 0,5 ч. + охлаждение на воздухе Annealing 350 °C, 3 h + normalization 980 °C, 0.5 h + cooling in air	2.015	38.905	-//-
4 (-//-)	3D (СЛС) 3D (SLS)	-//-	10.62	206.248	-//-
5 (-//-)	Литьё Casting	Нет / not	2.0	40.287	-//-
6 (-//-)	Литьё Casting	-//-	10.47	251.334	-//-
7 (2 п.) 7 (2nd batch)	3D (СЛС) 3D (SLS)	Отжиг 350 °С, 3 часа (1ч. + 2ч.) Annealing 350 °C, 3 hours (1h + 2h)	2.09	39.683	7.815
8 (-//-)	3D (СЛС) 3D (SLS)	Отжиг 350 °С, 3 ч. + нормализация 980 °С, 0,5 ч. + охлаждение на воздухе / Annealing 350 °C, 3 h + normalization 980 °C, 0.5 h + cooling in air	2.07	40.704	7.800
9 (-//-)	Литьё Casting	Нет / not	2.0	41.461	7.89

* – измерялся на весах Advencurer (Lohaus Corp.), ИПФ НАНБ / measured on a scale Advencurer (Lohaus Corp.), IAPH BAS

** – определялась с помощью гидростатического взвешивания, ИПФ НАНБ / determined by hydrostatic weighing, IAPH BAS

Результаты и обсуждение

На рисунке 2*a* представлены результаты измерения $U_{эф}$ МШ и зависимости от режимов термической обработки АТ–образцов и полученных литьём для 1-й партии (толщина 2 и 10 мм) с использованием преобразователя Баркгаузена (ПБ1), на рисунке 2*b* – с использованием ПБ2 для 2-й партии (2 мм). Преобразователи ПБ1 и ПБ2 между собой отличались типоразмерами, техническими параметрами, условиями перемагничивания образца и измерения МШ. Измерения МШ проводились в центре поверхности обеих сторон образца и усреднялись по 7–10 измерениям $U_{эф}$. Из гистограмм следует, что для обеих партий и толщин между трёхмерными отожжёнными (№ 1, 2, 7), нормализованными (№ 3, 4, 8) и литыми (№ 5, 6, 9) образцами имеется значительная разница, обусловленная наличием взаимосвязи $U_{эф}$ МШ с влияющими на показатели качества и ФМС металла параметрами. Из рисунков 2*a* и 2*b* видно, что чувствительность и селективность $U_{эф}$ к термической обработке можно значительно увеличить за счёт оптимизированной комбинации условий перемагничивания образца преобразователем Баркгаузена и установочных режимов анализа МШ. При использовании ПБ1 разница показаний магнитошумового прибора между отожжённым (№ 7) и нормализованным (№ 8) образцами составила ≈25–30 %, при использовании ПБ2 разница между ними составляет уже 2,3 раза и по уровню МШ они поменялись местами (рисунок 2*b*). Возможно, результат обусловлен использованием принципиально нового типа ПБ2, условиями перемагничивания и анализа МШ, и в связи с этим, изменением глубины перемагничивания и толщины информативного слоя в слоистом АТ-изделии.

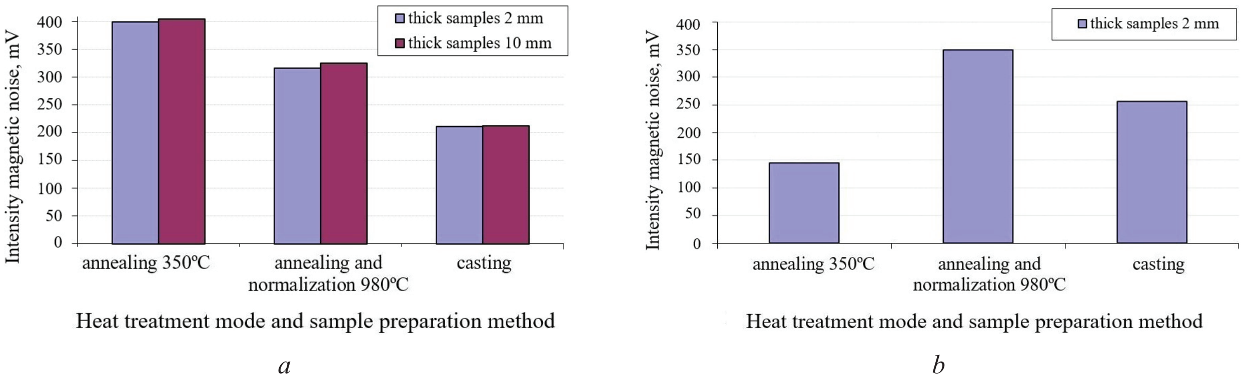

Рисунок 2 – Зависимость интенсивности магнитного шума от режимов термообработки трёхмерных и литых образцов обеих партий: *a* – с использованием ПБ1; *b* – ПБ2

Figure 2 – Dependence of the intensity of magnetic noise on the modes of heat treatment of three-dimensional and cast samples from both batches: *a* – using sensor 1; *b* – sensor 2

Для сравнения полученных с помощью МЭБ результатов контроля качества термообработки на рисунке 3*a* представлены результаты измерения твёрдости по Бринеллю (HB) с помощью ТПЦ-7 образцов из 1-й партии (толщина 2 и 10 мм), на рисунке 3*b* – образцов из 2-й партии толщиной 2 мм. Измерения HB выполнялись на обеих поверхностях в центре образца и усреднялись по данным пяти измерений. Для обеих партий образцов отчётливо видна значительная разница значений HB между отожжёнными и нормализованными образцами, однако разница HB между нормализованными и литыми образцами практически отсутствует. Полученные данные качественно совпали с приведенными в [11] результатами наноиндентирования образцов этой же стали: твёрдость литых образцов примерно в 1,5 раза меньше твёрдости 3D-образцов.

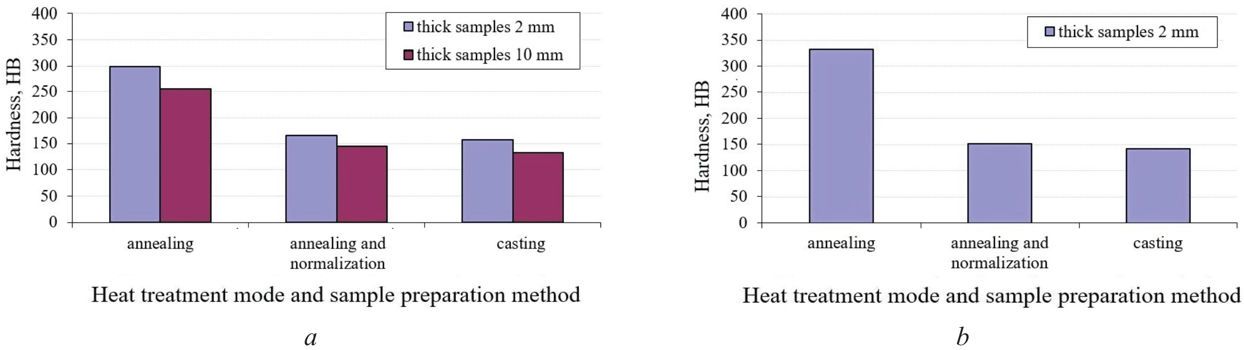

Рисунок 3 – Твёрдость для 1-й (*a*) и 2-й (*b*) партий образцов, полученных с помощью аддитивной технологии (методом селективного лазерного сплавления) и литья, измеренная твердомером ТПЦ-7

Figure 3 – Hardness for the 1st (*a*) and 2nd (*b*) batches of samples obtained using additive technology (selective laser melting) and casting, measured with a hardness tester TPC-7

По данным значений твёрдости разница между отожжённым и нормализованным 3D образцами толщиной 2 мм для обеих партий составляет 130 ед. HB (или 1,8 раза) и 125 ед. HB для толщин 10 м (2,1 раза), что несколько выше, чем при использовании ПБ1 для прибора ИМШ, и примерно такая же с применением ПБ2. Высокая разница показаний твёрдости между отожжёнными и нормализованными образцами вызвана тем, что метод индентирования, в основном, предназначен для определения механических характеристик металла и малочувствителен к микроструктуре. Поэтому между нормализованным (3D) и литым образцами разницы практически нет (рисунок 3*a*, *b*), в то время как по данным МЭБ (рисунок 2*a*, *b*), между литым и 3D-образцами существует значительная разница (более чем в 1,5 раза). Возможно, разница в чувствительности обоих методов к микроструктуре и ФМС в пользу МЭБ вызвана тем, что в АТ-образцах в процессе изготовления могут образовываться зоны локального напряжённо-деформированного состояния, пористость, микротрещины и другие дефекты, которые на $U_{эф}$ оказывают более сильное влияние, чем на твёрдость, а также применением ПБ2 и слоистостью образца. В подтверждение этому из таблицы видно, что удельная плотность литого образца 2-й партии образцов на ≈10 % выше, чем у 3D-образцов, а о влиянии пористости на МШ в порошковой стали ШХ15 было указано в [21]. Кроме пористости на МШ может оказать воздействие изменение размера зерна 3D-образцов, приводящая к росту механической анизотропии, которая оказывает более сильное влияние на $U_{эф}$, чем на твёрдость.

Таким образом, магнитошумовой параметр $U_{эф}$ обладает высокой информативностью к качеству термической постобработки за счёт связи не только с фазово-структурными превращениями, влияющими на микро- и макроструктуру 3D-образцов, но и селективностью к пористости, остаточным напряжениям, анизотропии и размеру зерна в металле, что позволяет использовать МЭБ в качестве одного из физических методов оценки качества и НК термообработки образцов, полученных аддитивным способом.

Заключение

Проведены экспериментальные исследования возможности оценки и неразрушающего контроля качества термической обработки образцов из низколегированной стали 09Г2С, полученных методом селективного лазерного сплавления и, для сравнения, методом литья, с помощью магнитошумового и контактно-динамического методов.

Установлено, что, как и метод твердометрии, магнитошумовой метод обладает высокой чувствительностью к термической обработке трёхмерных отожжённых и нормализованных образцов. Показано, что использование специальных сенсорных устройств с применением нового типа преобразователя Баркгаузена, способов перемагничивания и анализа магнитного шума позволило повысить в 2,5 раза чувствительность информативного магнитошумового параметра при разбраковке трёхмерных образцов. На основе анализа полученных данных, благодаря универсальности и селективности магнитошумового метода, дополнительно выявлена чувствительность к образцам, полученным с помощью литья, и возможность отбраковки от нормализованных синтезированных образцов, которые по данным рентгеноструктурного анализа близки между собой.

Интенсивность магнитного шума как критериальный параметр в комплекте с портативной измерительной аппаратурой и набором преобразователей может быть использована для оценки и экспресс-контроля качества термической и других видов обработок, при отработке режимов лазерного сплавления, оптимизации параметров металлического порошка и лазерного оборудования, с целью получения высоких прочностных и иных физических и механических характеристик аддитивных материалов.

Список использованных источников

1. *Гибсон Я.* Технология аддитивного производства: пер. с англ. / Я. Гибсон, Д. Розен, Б. Стакер // Москва: Техносфера. – 2016. – 656 с.

2. Стратегия развития аддитивных технологий // Аддитивные технологии. – 2021. – № 4. – С. 10–11.

3. *Каблов Е.Н.* Стратегические направления развития материалов и технологий их переработки на период до 2030 года / Е.Н. Каблов // Авиационные материалы и технологии. – 2015. – № 1 (34). – С. 3–33.

4. *Алешин Н.П.* Применение методов неразрушающего контроля для оценки качества деталей

непосредственно в процессе аддитивного производства / Н.П. Алешин, Н.В. Григорьев, Н.А. Щипаков [и др.] // Дефектоскопия. – 2016. – № 9. – С. 64–71.

5. *Алешин Н.П.* Некоторые особенности исследований деталей, изготовленных по аддитивным технологиям, методом рентгеновской компьютерной томографии / Н.П. Алешин, Н.В., О.А. Крупнина [и др.] // Дефектоскопия. – 2018. – № 4. – С. 42–48.

6. *Бусько В.Н.* Особенности циклической усталостной прочности образцов, полученных селективным лазерным спеканием из стали 09Г2С / В.Н. Бусько, В.Л.Венгринович, Д.А. Винтов [и др.] // Неразрушающий контроль и техническая диагностика. – 2020. – № 4. – С. 16–25.

7. *Алешин Н.П.* Применение методов неразрушающего контроля для оценки качества готовых деталей аддитивного производства / Н.П. Алешин, Н.В. Григорьев, Н.А. Щипаков Н.А [и др.] // Дефектоскопия. – 2016. – № 10. – С. 63–71.

8. *Алешин Н.П.* О возможности применения поверхностных и головных ультразвуковых волн при неразрушающем контроле качества изделий аддитивного производства / Н.П. Алешин, Н.В. Григорьев, Н.А. Щипаков Н.А [и др.] // Дефектоскопия. – 2017. – № 12. – С. 16–23.

9. *Алешин Н.П.* Оценка результатов исследования деталей, изготовленных по аддитивным технологиям, альтернативными методами / Н.П. Алешин, Н.В. Григорьев, Н.А. Щипаков [и др.] // Дефектоскопия. – 2016. – № 12. – С. 25–31.

10. *Алешин Н.П.* Экспериментальные исследования возможностей и особенностей ультразвукового контроля деталей, изготовленных по аддитивным технологиям / Н.П. Алешин, Н.В., Н.В. Григорьев, Н.А. Щипаков [и др.] // Дефектоскопия. – 2016. – № 12. – С. 17–24.

11. *Ничипурук А.П.* Структура и магнитные свойства стали 09Г2С, полученной методом селективного лазерного сплавления / А.П. Ничипурук, А.Н. Сташков, Е.А. Щапова [и др.] // Физика твердого тела. – 2021. – Т. 63. – С. 1719–1724.
DOI: 10.21883/FTT.2021.11.51567.25s

12. *Tu Le Manh, Jose Alberto Perez Benitez, Jose Hiram Espina Hernandez, Jose Manuel Hallen Lo pez.* Barkhausen Noise for Nondestructive Testing and Materials Characterization in Low-Carbon Steels. Cambridge, United States, Elsevier Ltd., 2020, 268 p.

13. *Горкунов Э.С.* Эффект Баркгаузена и его использование в структуроскопии ферромагнитных материалов (обзор I/обзор II) / Э.С. Горкунов, Ю.Н. Драгошанский, М. Миховски // Дефектоскопия. – 1999. – № 6. – С. 3–23 // Дефектоскопия. – 1999. – № 7. – С. 3–32.

14. *Блаоу М.М.* Магнитные шумы Баркгаузена для надежного измерения зоны термического влияния в сварной пластине из судостроительной стали / М.М. Блаоу, Б.А. Шау // В мире неразрушающего контроля. – 2014. – № 4. – С. 70–75.

15. *Ашвани Шарма.* Влияние условий шлифования на магнитный отклик инструментальной стали AISI D2 / Шарма Ашвани, Чаудхари Абхиманью, Субхаш Акаш [и др.] // Дефектоскопия. – 2021. – №3. – С. 26–36.
DOI: 10.31857/SO130308221030039

16. *Иванова Й.* Сравнительные измерения напряженного состояния проката углеродистой стали посредством шума Баркгаузена и ультразвука / Й. Иванова, Т. Парталин // Дефектоскопия. – 2012. – № 4. – С. 83–94. **DOI:** 10.1134/S1061830912020040

17. *Филинов В.В.* Применение метода магнитных шумов для контроля технологических напряжений / В.В. Филинов, В.Е. Шатерников, В.А. Рукавишников [и др.] // Контроль. Диагностика. – 2005. – № 3. – С. 17–24.

18. *Бусько В.Н.* Исследование и оценка механической анизотропии сталей и сплавов магнитошумовым методом / В.Н. Бусько, А.А. Осипов // В мире неразрушающего контроля. – 2020. – № 3. – С. 50–56.
DOI: 10.12737/1609-3178-2020-50-56

19. *Rudnitsky V.A., Kren A.P., Lantsman G.A.* Determining Yield Strength of Metals by Microindentation with a Spherical Tip // Russian Journal of Nondestructive Testing, 2019, vol. 55, pp. 162–168.
DOI: 10.1134/S1061830919020098

20. *Kren A., Delendik M., Machikhin A.* Non-destructive evaluation of metal plasticity using a single impact microindentation // International Journal of Impact Engineering, 2022, vol. 162, p. 104141.
DOI: 10.1016/j.ijimpeng.2021.104141

21. *Бусько В.Н.* Оценка пористости порошкового материала подшипниковой стали с помощью метода магнитных шумов / В.Н. Бусько, А.А. Дмитрович // Материалы 37-го межгосударственного семинара “Защитные покрытия, сварка и контроль” / Ред. А.Ф. Ильющенко и др. – Минск: 2006. – С. 66.

References

1. Gibson I., Rosen D., Stucker B. Additive Manufacturing Technologies: 3D Printing, Raid Prototiping, and Direct Digital Manufacturing: Springer, 2015, 498 p.

2. Strategy for the development of additive technologies. *Additivnye tekhnologii* [Additive Technologies], 2021, no. 4, pp. 10–11 (in Russian).

3. Kablov E.N. Strategic directions for the development of materials and technologies for their processing for

the period up to 2030. *Aviacionnye materialy i tekhnologii* [Aviation materials and technologies], 2015, no. 1(34), pp. 3–33 (in Russian).

4. Aleshin N.P., Grigor'ev T., Shchipakov N.A., Prilutskii M.A., Murashov V.V. Using nondestructive testing methods for in-production quality control of additive manufactured parts. *Russian Journal of Nondestructive Testing*, 2016, vol. 52, pp. 532–537.
DOI: 10.1134/S1061830916090023

5. Aleshin N.P., Grigor'ev M.V., Krupnina O.A., Shchipakov N.A. Some features of the study of parts manufactured using additive technologies using X-ray computed tomography. *Russian Journal of Nondestructive Testing*, 2018, vol. 54, no. 4, pp. 271–277.
DOI: 10.1134/S1061830918040022

6. Busko V.N., Vengrinovich V.L., Vintov D.A., Nichipuruk A.P. , Stashkov A.N. Peculiarities of Cyclic Fatigue Strength of Specimens Produced by Selective Laser Sintering from Steel 09G2S. *Nondestructive testing and technical diagnostics*, 2020, no. 4, pp. 16–25 (in Russian).

7. Aleshin N.P., Grigor'ev T., Shchipakov N.A., Prilutskii M.A., Murashov V.V. Applying nondestructive testing to quality control of additive manufactured parts. *Russian Journal of Nondestructive Testing*, 2016, vol. 52, no. 10, pp. 600–609. **DOI:** 10.1134/S1061830916100028

8. Aleshin N.P., Grigor'ev M. V., Shchipakov N.A., Krys'ko N.V., Krasnov I.S., Prilutskii M.A., Smorodinskii Y.G. On the possibility of using surface and head ultrasonic waves for non-destructive quality control of additive manufacturing products. *Russian Journal of Nondestructive Testing*, 2017, vol. 53, no. 12, pp. 830–838.
DOI: 10.1134/S1061830917120026

9. Aleshin N.P., Grigor'ev M.V., Murashov V.V., Krasnov I.S., Krupnina O.A., Smorodinskii Y.G. Assessing the results of ultrasonic testing of additive manufactured parts with alternative methods. *Russian Journal of Nondestructive Testing*, 2016, vol. 52, no. 12, pp. 691–696. **DOI:** 10.1134/S1061830916120032

10. Aleshin N.P., Murashov V., Shchipakov N., Krasnov I., Lozhkova D. Experimental research into possibilities and peculiarities of ultrasonic testing of additive manufactured parts. *Russian Journal of Nondestructive Testing*, 2016, vol. 52, no. 12. pp. 685–690.
DOI: 10.1134/S1061830916120020

11. Nichipuruk A.P., Stashkov A.N., Shchapova E.A., Kazantseva N.V., Makarova M.V. Structure and Magnetic Properties of 09G2S Steel Obtained by the Selective Laser Melting Metod. *Physics of the Solid State*, 2022, vol. 64, pp. 148–153.
DOI: 10.1134/S106378422030076

12. Tu Le Manh, Jose Alberto Perez Benitez, Jose Hiram Espina Hernandez, Jose Manuel Hallen Lo pez. Barkhausen Noise for Nondestructive Testing and Materials Characterization in Low-Carbon Steels. Cambridge, United States, Elsevier Ltd. Publ., 2020, 268 p.

13. Gorkunov E.S., Dragoshansky Yu.N., Mihovski M. Barkhausen effect and its use in structuroscopy of ferromagnetic materials (review I/review II). *Russian Journal of Nondestructive Testing*, 1999, no. 6, pp. 3–23 and // *Russian Journal of Nondestructive Testing*, 1999, no. 7, pp. 3–32 (in Russian).

14. Blaow M.M., Shau B.A. Barkhausen Magnetic Noises for Reliable Measurement of the Heat-Affected Zone in a Welded Shipbuilding Steel Plate. *NDT World*, 2014, no. 4. pp. 70–75.

15. Ashwani Sharma, Abhimanyu Chaudhary, Akash Subhash, Mohd Zahir Khan Yusufzay, Meganshu Vashista. Influence of grinding conditions on the magnetic response of AISI D2 tool steel. *Russian Journal of Nondestructive Testing*, 2021, vol. 57, pp. 212–221.
DOI: 10.31857/SO130308221030039

16. Ivanova Y., Portalin T. Comparative Measurements of the Stressed State of Rolled Carbon Steel Using Barkhausen Noise and Ultrasonic methods. *Russian Journal of Nondestructive Testing*, 2012, no. 4, pp. 83–94.
DOI: 10.1134/S1061830912020040

17. Filinov V.V., Shaternikov V.E., Rukavishnikov V.V., Naroditsky A.M., Pleshakov V.V., Kovalev D.A. Application of the method of magnetic noise to control process stresses. *Kontrol'. Diagnostika* [Control. Diagnostics], 2005, no. 3, pp. 17–24 (in Russian).

18. Busko V.N., Osipov A.A. Research and Evaluation of the Mechanical Anisotropy of Steel an Alloys by the Magnetic Noise Method. *NDT World*, 2020, no. 3. pp. 50–56 (in Russian).
DOI: 10.12737/1609-3178-2020-50-56

19. Rudnitsky V.A., Kren A.P., Lantsman G.A. Determining Yield Strength of Metals by Microindentation with a Spherical Tip. *Russian Journal of Nondestructive Testing*, 2019, vol. 55, no. 2, pp. 162–168.
DOI: 10.1134/S1061830919020098

20. Kren A., Delendik M., Machikhin A. Non-destructive evaluation of metal plasticity using a single impact microindentation. *International Journal of Impact Engineering*, 2022, vol. 162, p. 104141.
DOI: 10.1016/j.ijimpeng.2021.104141

21. Busko V.N., Dmitrovich A.A. Evaluation of the porosity of bearing steel powder material using the magnetic noise method. Materials of the 37th interstate seminar "Protective coatings, welding and control". Editor A. Ilyushchenko, Minsk, 2006, p. 66 (in Russian).

ПРАВИЛА ОФОРМЛЕНИЯ СТАТЕЙ

Статьи, направленные в редакцию журнала, должны удовлетворять требованиям «Инструкции о порядке оформления квалификационной научной работы (диссертации)…», утвержденной Постановлением ВАК РБ от 28.02.2014 г. № 3

1. Материал статьи должен соответствовать профилю журнала и излагаться предельно ясно.

2. Статья представляется на русском или английском языке и публикуется на языке представления.

3. Поступившие в редакцию статьи проходят двойное полуслепое рецензирование. Основные критерии целесообразности опубликования – актуальность тематики, информативность, научная новизна.

4. Статья представляется в распечатанном и в электронном виде в формате текстового редактора Word for Windows, набор – сплошным текстом (без деления на колонки). Объём статьи не должен превышать 14 страниц, включая текст (шрифт Times New Roman, размер 12 п., интервал 1,5), таблицы, графический материал, всю необходимую информацию на английском языке.

5. На первой странице статьи указываются: название статьи, фамилии авторов (фамилия автора, с которым следует вести переписку, отмечается звёздочкой и указывается его адрес электронной почты), названия и почтовые адреса организаций (улица, номер дома, индекс, город, страна), в которых работают авторы, на русском и английском языках. Статья включает: аннотацию (в пределах 200–250 слов); ключевые слова (не более 5); введение, в котором делается краткий обзор сделанного в мире и конкретно формулируется цель работы; основную часть; заключение, в котором в сжатом виде сформулированы основные полученные результаты с указанием их новизны, преимуществ и возможностей применения; список использованных источников. Аннотация, ключевые слова, список использованных источников представляются на русском и английском языках.

6. Аннотация должна быть информативной (содержать «выжимку» из всех разделов статьи – введения с указанием цели работы, методики, основной части и заключения).

7. Графический материал должен быть контрастным и чётким. Необходимо придерживаться единообразия техники исполнения однотипных иллюстраций. Рисунок должен располагаться после абзаца, содержащего ссылку на него. Не допускается размещение рисунков в конце подраздела и статьи. Изобразительный материал вставляется в текст статьи, а также даётся в виде отдельных файлов **(формат tif, jpg, разрешение не менее 300 dpi)**. Текст на рисунках набирается основной гарнитурой; размер кегля соизмерим с размером рисунка (желательно 8 пунктов). Все рисунки нумеруются и сопровождаются подрисуночными подписями. Фрагменты рисунка обозначаются строчными курсивными латинскими буквами – «*a*», «*b*» и т. д. Надписи на рисунках и подписи к рисункам даются на русском и английском языках. Все сокращения и обозначения должны быть расшифрованы в подрисуночной подписи. Рисунки желательно предоставлять в цвете. На рисунках должны быть указаны оси с обозначением приводимых величин и масштабов. На графиках не нужно давать координатную сетку, если это не осциллограмма. Во всех случаях на рисунках должен быть приведён масштаб.

8. У графиков, имеющих числовые значения по осям, рамки должны быть открыты, а засечки направлены внутрь рамки. На рисунках, представляющих собой графики зависимостей, не следует делать размерную сетку, следует дать лишь засечки на осях, причем все засечки должны быть оцифрованы. Если оси на рисунках оцифрованы, то они завершаются на позиции очередной засечки, где засечка не ставится, а вместо числовых значений даются обозначения переменной и единица измерения. Если оси не оцифровываются, то они завершаются стрелками, рядом с которыми даются обозначения переменных без единиц измерения.

9. Полутоновые фотографии приборов или их частей представляются при публикации в тех случаях, когда они несут существенную информацию, которую нельзя выразить иным способом. Фотографии должны быть высококачественными, контрастными, с хорошо различимыми деталями.

10. Иллюстрации (графики, диаграммы, схемы, чертежи), рисованные средствами MS Office, должны быть контрастными и чёткими. Недопустимо нанесение средствами MS Word каких-либо элементов поверх вставленного в файл рукописи рисунка (стрелки, подписи) ввиду большого риска их потери на этапах редактирования и вёрстки. Иллюстрации должны иметь размеры, соответствующие их информативности: 8–8,5 см (на одну колонку), 17–17,5 см (на две колонки) или 23 см (во весь лист). Поэтому желательно изображать отдельные элементы и надписи на рисунке так, чтобы при уменьшении масштаба рисунка до одного из указанных размеров буквы и цифры приобрели высоту 2–2,5 мм, элементы схем 3–5 мм, отдельные точки 1 мм, а линии должны быть при этом разнесены на расстояние не менее 0,5–1 мм.

11. Надписи и обозначения на иллюстрациях следует располагать так, чтобы они не соприкасались ни с какими её частями. На задний план иллюстрации желательно не добавлять серый (цветной) фон или сетки.

12. Таблицы не должны дублировать графики. Каждая таблица имеет заголовок. На все таблицы

и рисунки следует давать ссылки в тексте. Таблицы не должны содержать вертикальные линии, делящие таблицу на столбцы. Название и содержание таблиц представляется на русском и английском языках.

13. Обозначения и сокращения, принятые в статье, расшифровываются непосредственно в тексте.

14. Размерность всех величин, принятых в статье, должна соответствовать Международной системе единиц измерений (СИ).

15. Набор формул должен проводиться в редакторе MathType целиком. Набор формул из составных элементов не допускается, номера формул – по правому краю. Нумеруются лишь формулы, на которые есть ссылки в тексте.

16. Необходимо использовать следующие установки редактора формул. Размеры: полный – 10 пт, подстрочный – 9 пт, под-подстрочный – 7 пт, символ – 14,5 пт, подсимвол – 12,5 пт. Стили: текст, функция, число, кириллица – шрифт «Times New Roman», вектор-матрица – шрифт «Times New Roman», жирный; греческий малый, греческй большой, символ – шрифт «Symbol», прямой; переменная – шрифт «Times New Roman», курсив.

17. Отдельные строчные буквы и специальные символы набираются в тексте гарнитурой Symbol **без использования редактора формул**. При наборе формул и буквенных обозначений необходимо учитывать следующие правила: **русский алфавит не используется**; греческие буквы, математические символы (grad, div, ln, min, max и др.), единицы измерения (Вт, Дж, В, кг и др.), кириллические буквы, сокращения от русских слов ($q_{\text{ср}}$); обозначения химических элементов и соединений (в т. ч. в индексе) набираются **прямо**; латинские буквы – переменные и символы физических величин (в т. ч. в индексе) набираются **курсивом**; векторы – жирным шрифтом (стрелки вверху не ставятся).

18. Начертание обозначений в формулах и в основном тексте должно быть полностью идентично. В расшифровке формул, которая начинается словом «где», символы и их порядок должны соответствовать символам и их порядку следования в формулах.

19. Список использованных источников составляется в порядке упоминания ссылок по тексту, должен содержать полные библиографические данные и приводится в конце статьи. Не рекомендуется давать ссылки на материалы конференций, статьи из электронных журналов без идентификатора **DOI**, учебные пособия, интернет-ресурсы. Ссылки на неопубликованные работы не допускаются. Желательно, чтобы количество ссылок было не менее 10; самоцитирование – не более 20 %.

20. Авторы на отдельной странице предоставляют о себе следующие сведения: фамилия, имя, отчество, ученая степень и звание, место работы и занимаемая должность, адрес электронной связи.

21. Статьи, излагающие результаты исследований, выполненных в учреждениях, должны иметь соответствующее разрешение на опубликование в открытой печати.

22. При необходимости в конце основного текста указываются наименование фонда, оказавшего финансовую поддержку, или уровень и наименование программы, в рамках которой выполнена работа, на русском и английском языках.

23. Авторы несут ответственность за направление в редакцию статей, ранее уже опубликованных или принятых к печати другими изданиями.

24. Статьи, не соответствующие перечисленным требованиям, к рассмотрению не принимаются и возвращаются авторам. Датой поступления считается день получения редакцией первоначального варианта текста.

25. Редакция предоставляет возможность первоочередного опубликования статей лицам, осуществляющим послевузовское обучение (аспирантура, докторантура, соискательство), в год завершения обучения; не взимает плату с авторов за опубликование научных статей; оставляет за собой право производить редакторские правки, не искажающие основное содержание статьи.

AUTHOR GUIDELINES

1. Article materials should correspond to the journal profile and be clearly written.
2. An article should be submitted in Russian or English and will be published in its original language.
3. Articles received by the Editorial Board will be reviewed by 2 specialists. The main criteria of acceptance are theme actuality, information value, and scientific novelty.
4. All materials should be submitted in two hard copies together with electronic file in the Word for Windows format (97/2000/2003). The paper should not exceed 14 pages of the typewritten text (Times New Roman, 12 points, 1.5-space).
5. The article should contain UDC number, Title (printed in capitals), Authors' names (the corresponding author name should be marked with asterisk), full Address of organization(s) in which the author(s) work, Abstract (200–250 words), Keywords (not more than 5 words), Introduction, the Text of the paper with tables, diagrams and figures (if there are any), Conclusion with clearly stated inferences, List of References, List of Symbols and Abbreviations (if it is necessary). Title, Authors' names and affiliation(s), Abstract, Keywords should be presented both in English and Russian languages.
6. The abstract should be informative (contain "squeeze" from all sections of the article – the introduction stating the purpose of the work, methods, main part and conclusion).
7. Figures should be black-and-white, represented in graphical formats tif, attached with Excel or MS Graph and added with captions. All symbols in figures should be descripted.
8. Tables should be placed directly in the article body. Diagrams and tables should not contain the same information. Each table should have the title. All tables, diagrams and figures should be referenced in the text.
9. Symbols and abbreviations which are used in articles should be deciphered directly in the text and also (if necessary) taken out on a separate page.
10. Dimensions of all quantities used in the article should correspond to International System of Units.
11. Formulas should be taped in MathType.
12. List of References is to be placed at the end of the article with full bibliographic information. Order of references should correspond to the order of their occurrence in the text. It is not recommended to refer to conference proceedings, papers from electronic journals without **DOI** number, textbooks, internet resources. References on unpublished works are prohibited. It is recommended to refer to not less than 10 references, self-citations – not more than 20 %.
13. The following information about every co-author should be presented: family name, first name, patronymic (or second) name (if there are any), scientific degree and title, organization and position, full address with the postal code for correspondence, office or mobile phone numbers, fax, e-mail.
14. Articles containing investigation results obtained in organizations should have a corresponding permission for publication.
15. Names of Foundations or Programs financially granted the research may be acknowledged in the end of the text.
16. Authors are responsible for submitting articles previously published or accepted by other publisher.
17. Articles not meeting the requirements of the Editorial Board would not be accepted and may be returned to the authors. The date of receipt is considered to be the day when the Editorial Board receives the author's original paper.
18. Authors conducting postgraduate (graduate studies, doctoral studies) have a priority in publishing their articles out of queue in the year of completion. Authors do not pay for publishing scientific articles. The Editorial Board can shorten and/or change the text if it does not strain the meaning of the article.

Индексы:
74835; 748352